Osaka University Knowledge Archive

Title	Experimental Studies on Electronic States of Iron Pnictide Superconductors RFe(P, As)(O, F) (R = La, Pr, Nd)
Author(s)	竹森, 章
Citation	大阪大学, 2015, 博士論文
Version Type	VoR
URL	https://doi.org/10.18910/52313
rights	
Note	

Dissertation for Doctoral Degree

Experimental Studies on Electronic States

of Iron Pnictide Superconductors

RFe(P, As)(O, F) (R = La, Pr, Nd)

Department of Physics, Graduate School of Science, Osaka University

Akira Takemori

February 2, 2015

Abstract

The iron-based superconductors show unconventional superconductivity with high superconducting transition temperature (T_c). Several experimental studies have suggested that T_c is strongly correlated with the local structural parameters around Fe site such as pnictogen - Fe - pnictogen bond angle and pnictogen height from Fe layer. However, it is not clear yet what electronic parameter is modified by these structural parameters. On the other hand, some theories suggest that the antiferromagnetic (AFM) fluctuation plays an important role for the appearance of superconductivity in the iron-based superconductors, but there is no direct experimental evidence that T_c is correlated with the strength of antiferromagnetic fluctuation. Therefore, in order to clarify the mechanism of superconductivity in this system, it is necessary to find a microscopic parameter that scales with T_c, comparing various physical properties of various iron pnictides with different T_c.

In this work, I focus on $R\mathrm{FeP}_{1-x}\mathrm{As}_x\mathrm{O}_{0.9}\mathrm{F}_{0.1}$, where R are La, Pr, and Nd. First advantage of this system is that P and As are isovalent elements and thus a carrier number is kept constant in principle. The change in physical properties with x is considered to be induced by a structural change due to chemical pressure. The second advantage is that I can cover a wide range of T_c from ~ 3 to ~ 50 K by changing x. This helps us to find a physical quantity that scales with T_c. The third advantage is that the strength of antiferromagnetic fluctuation can be controlled by varying x. $R\mathrm{FeAsO}$ is an antiferromagnetic metal. With F doping, the magnetic order is suppressed and the superconductivity appears above F concentration of ~ 0.08. Therefore, the end material in the present study, $R\mathrm{FeAsO}_{0.9}\mathrm{F}_{0.1}$ shows superconductivity, but has large antiferromagnetic fluctuation. In contrast, the other end material $R\mathrm{FeP(O, F)}$ are superconducting at lower temperature and shows a paramagnetic metallic behavior in the normal state. Therefore, the antiferromagnetic fluctuation is expected to be controllable by changing x in $R\mathrm{FeP}_{1-x}\mathrm{As}_x\mathrm{O}_{0.9}\mathrm{F}_{0.1}$. In the present study, I have investigated the transport properties and

angle resolved photoemission spectroscopy (ARPES) in $R\mathrm{FeP}_{1-x}\mathrm{As}_x\mathrm{O}_{0.9}\mathrm{F}_{0.1}$ with various T_c, lattice constants and presumably antiferromagnetic fluctuation strength to find a relationship among T_c, crystal structure and electronic properties in iron pnictides.

First, I have studied the transport properties of the polycrystalline samples and single crystals, and searched the parameters correlating to T_c. The present results have revealed that there are two distinct regions of x. In the low x region ($x < 0.6$ - 0.8), T_c linearly increases from $\sim$ 3 to $\sim$ 30 K with decreasing the power n in $\rho = \rho_0 + AT^n$ from 2 at $x = 0$ to 1 around $x =$ 0.6 - 0.8. This strongly suggests that some bosonic fluctuation such as antiferromagnetic one is a primary factor to enhance T_c. The universal T_c - n relation holds for all the R systems with $x < 0.6$ - 0.8. In addition to the T-linear resistivity, R_H, ρ_0, and A are strongly enhanced near $x = 0.6$ - 0.8, suggesting some critical change of the electronic state. In the high x region ($x > 0.6$ - 0.8), on the other hand, T_c becomes strongly R-dependent and further increases with x, but shows no clear correlation with n. The compounds with $x > 0.6$ - 0.8 seem to approach another universal T_c - n relation which holds for $R\mathrm{FeAsO}_{1-y}$. The presence of two distinct T_c - n relations could be the evidence that there are two T_c-rising mechanisms and related two different Fermi surface states in $R\mathrm{FeP}_{1-x}\mathrm{As}_x\mathrm{O}_{0.9}\mathrm{F}_{0.1}$.

Next, I have investigated the ARPES using single crystals of $\mathrm{NdFeP}_{1-x}\mathrm{As}_x\mathrm{O}_{0.9}\mathrm{F}_{0.1}$ with $x = 0.4$, 0.8 and 1.0 in order to clarify x-dependent changes of band structures and Fermi surfaces (FSs). The ARPES results indicate the existence of three hole and two electron FSs in $x = 0.4$, and two hole and two electron FSs in $x = 0.8$ and 1.0 samples. The orbital characters of these FSs have been assigned by the measurements of polarization dependence of incident light. The d_{xz} hole FS exists around Γ point at $x = 0.4$. The d_{xz} band sinks down with increasing x, and the top of this band touches E_F around Γ point in the $x = 0.8$ sample. With further increasing x, the hole FS with d_{xz} character disappears at $x = 1.0$. The T_c, n and other transport properties distinctly change around $x = 0.6$ - 0.8. The clear difference of FSs below and above $x = 0.6$ - 0.8 may be related with the change of transport properties, and support the scenario of two T_c-rising mechanisms and two different Fermi surface states in this system.

Contents

Part I

Introduction

Chapter 1

Introduction

1.1 Fundamental facts of iron-based superconductors

1.1.1 Discovery of iron pnictide superconductors

The first iron-based superconductor LaFePO having $T_c = 4$ K was discovered by Kamihara *et al.* in Tokyo Institute of Technology in 2006 [1]. Two years later, LaFeAs(O, F) ($T_c = 26$ K) was also reported by them [2] and studies on iron-based superconductors have been activated in all the world. T_c immediately increased to 55 K by substituting La with Sm whose ionic radius is smaller than that of La [3]. Additionally, new iron-based superconductors having different crystal structures were also discovered, such as $Ae\mathrm{Fe_2As_2}$ (122-type), FeSe (11-type) and so on. Iron-based superconductors have the second highest T_c following cuprates. Both of them are unconventional superconductors and do not follow the BCS theory, which explains the generation mechanism of Cooper pair mediated by electron-phonon coupling. Some common features between iron-based superconductors and cuprates are confirmed, such as (i) they have 2-dimensional layered structure constructed of conduction and insulation layers, (ii) superconductivity emerges by suppression of the AFM order of mother compounds, and so on. On the other hand, there is a difference that the mother compounds of cuprates are Mott-insulators and those of iron-based superconductors are AFM metals.

1.1.2 1111-type iron pnictides

1111-type iron pnictides $R\mathrm{Fe}Pn\mathrm{O}$ (R = rare earth and Pn = P, As) is one of representative iron-based superconductors. They are called 1111 system from the compositional ratio of R :

Fe : Pn : O = 1 : 1 : 1 : 1. The crystal structure of RFePnO is ZrCuSiAs-type (tetragonal, $P4/nmm$) and illustrated in Figure 1.1 RFePnO has the layered structure constructed of FePn
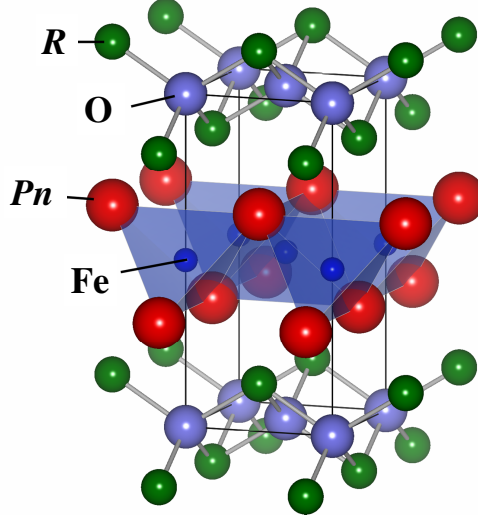
Figure 1.1: Crystal structure of RFePnO.

conduction layers and RO insulation layers. Therefore, physical properties of RFePnO, such as electrical resistivity and the critical magnetic field, show strong 2-dimensionality. SmFeAs(O, F) [3] and (Gd, Th)FeAsO [4] in this system shows superconductivity at $T_c \sim 55$ K, which is the highest in all iron-based superconductors. Almost all experimental studies on this system are performed by using polycrystalline samples because of the difficulty to grow large single crystals. Then clarification of physical properties of 1111 system is not advanced compared with other systems, such as 122 and 11 ones.

The emerging process of superconductivity is different between the cases of RFeAsO and RFePO. In the case of RFeAsO, the structural phase transition from a tetragonal lattice to an orthorhombic one and the magnetic phase transition to a spin density wave (SDW) -type AFM order occurs at T_s and $T_N \sim 150$K. Superconductivity emerges by electron doping to FeAs-layers, which is often accomplished by substituting O with F. The electronic phase diagrams of LaFeAsO$_{1-x}$F$_x$ and CeFeAsO$_{1-x}$F$_x$ are shown in Figure 1.2 [5, 6]. The AFM order is gradually suppressed and the superconducting state is enhanced for O/F substitution in both cases of LaFeAsO$_{1-x}$F$_x$ and CeFeAsO$_{1-x}$F$_x$. The maximum T_c reaches 26 K (R = La) - 55 K (R = Sm) in the case of O/F substitution and the F concentration is about 10 - 15%.

Not only O/F substitution, but also O/H substitution, O deficiency and Fe/Co substitution are electron doping ways. The O/H substitution limit is much higher than the O/F substitu-
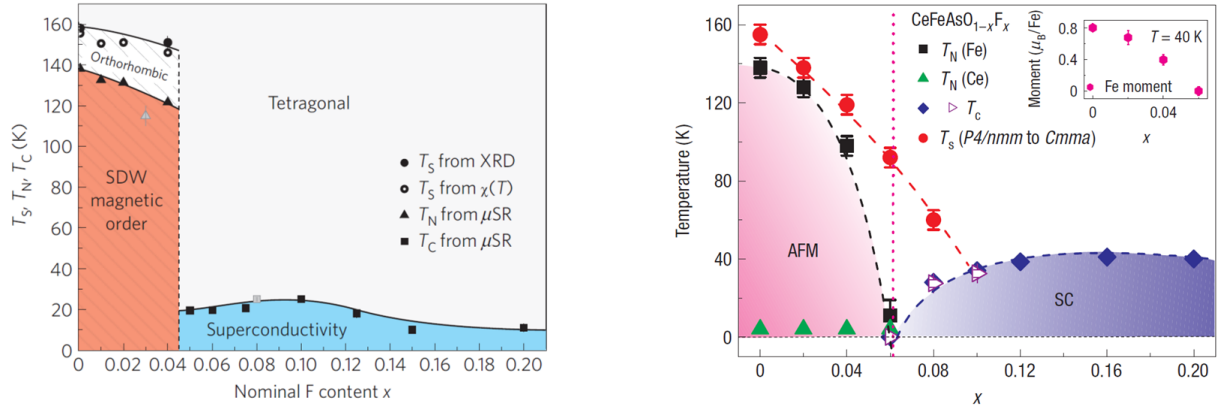
Figure 1.2: Electronic phse diagrams of LaFeAsO$_{1-x}$F$_x$ and CeFeAsO$_{1-x}$F$_x$ [5, 6].

tion one. The electronic phase diagrams of LaFeAsO$_{1-x}$H$_x$ is shown in Figure 1.3 [7]. Two superconducting domes are coupled and a new AFM order emerges at $x \sim 0.6$. The new AFM order seems to be caused by the nesting between electron FSs. O deficiency causes similar effect to O/F substitution [8]. Fe/Co substitution also shows superconductivity, but the T_c is much lower than that of O/F substitution [9]. This may be caused by the substitution in the FeAs conduction layers. On the other hand, RFePO does not have the above structural and magnetic transitions [1]. Superconductivity emerges without carrier doping and T_c is 2 - 5 K. Exceptionally, CeFePO shows heavy fermion-like behavior [10].
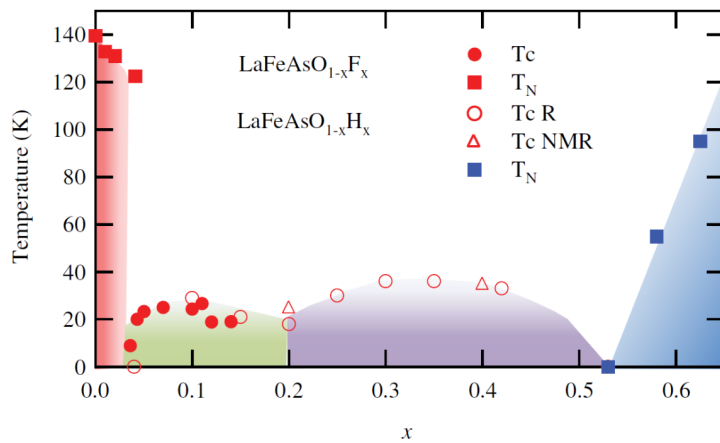
Figure 1.3: Electronic phase diagram of LaFeAsO$_{1-x}$H$_x$ [7].

9

1.1.3   122-type iron pnictides

122-type iron pnictides $Ae\mathrm{Fe_2As_2}$ (Ae = Ca, Sr, Ba of alkaline-earth metals or Eu) are also one of representative iron-based superconductors and called 122 system from the compositional ratio of Ae : Fe : As = 1 : 2 : 2. The crystal structure of $Ae\mathrm{Fe_2As_2}$ is $\mathrm{ThCr_2Si_2}$-type (tetragonal, $I4/mmm$) and illustrated in Figure 1.4. $Ae\mathrm{Fe_2As_2}$ also shows the structural and
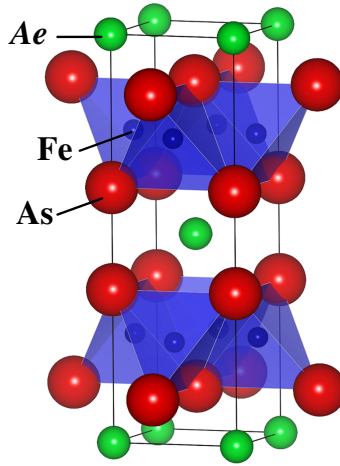
Figure 1.4: Crystal structure of $Ae\mathrm{Fe_2As_2}$.

the AFM transitions at low temperatures. T_s and T_N changes from $\sim$ 200 K (Ae = Sr) to $\sim$ 140 K (Ae = Ba) [11, 12]. Superconductivity emerges by substituting each element, such as Ae $\rightarrow$ Na or K (hole doping), Fe $\rightarrow$ Co or Ni (electron doping) and As $\rightarrow$ P (chemical pressure inducing). Large single crystals are obtained by using a self flux method in this system. Then experimental studies on 122 system is the most advanced in all iron pnictide superconductors.

Hole-doped system

Hole doping is mainly accomplished by substituting Ae with alkali metal A = Na, K, and so on. The electronic phase diagram of $\mathrm{Ba_{1-x}K_xFe_2As_2}$ is shown in Figure 1.5 [13]. Superconductivity emerges in the wide region of x = 0.2 - 1.0. T_c reaches 38 K at x = 0.4, which is the highest in 122 systems exept for a non-bulk superconductor $\mathrm{Ca_{1-x}R_xFe_2As_2}$ [14].
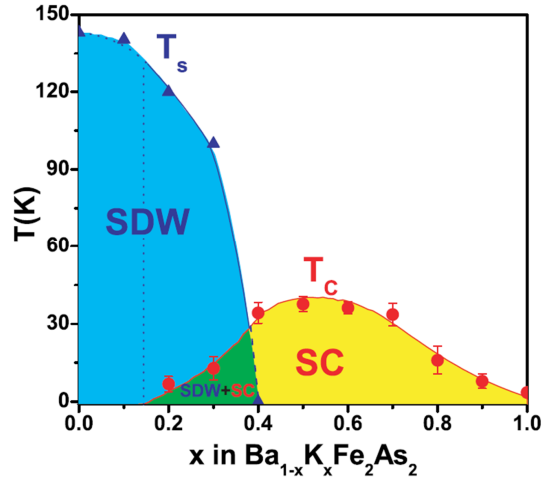
Figure 1.5: Electronic phase diagram of $Ba_{1-x}K_xFe_2As_2$ [13].

Electron-doped system

Electron doping is mainly accomplished by substituting Fe with transition metal $TM = Co$, Ni, and so on. The electronic phase diagram of $Ba(Fe_{1-x}Co_x)_2As_2$ is shown in Figure 1.6 [15]. The T_c of $Ba(Fe_{1-x}Co_x)_2As_2$ is lower than that of $Ba_{1-x}K_xFe_2As_2$ and $BaFe_2(As_{1-x}P_x)_2$. This seems to be caused by the disorder to $3d$ electron of Fe.
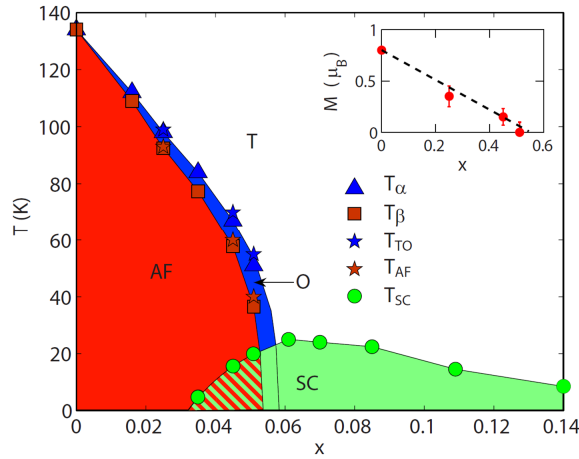
Figure 1.6: Electronic phase diagram of $Ba(Fe_{1-x}Co_x)_2As_2$ [15].

Pressure-induced system

Chemical pressure inducing is accomplished by substituting As with P. The temperature dependence of the electrical resistivity and the electronic phase diagram of $BaFe_2(As_{1-x}P_x)_2$ are presented in Figure 1.7 [16]. The maximum T_c reaches 30 K at $x = 0.33$. Temperature
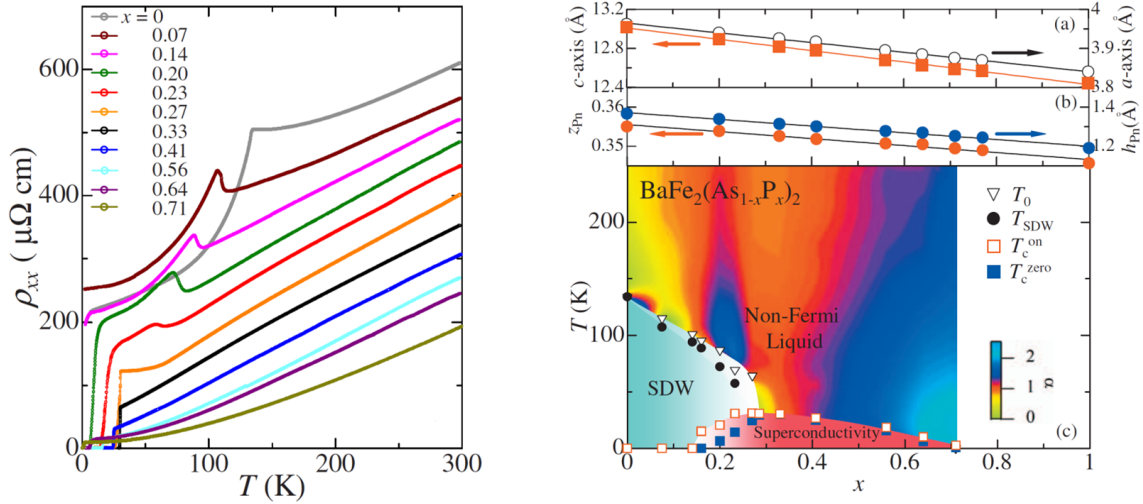
Figure 1.7: Temperature dependence of electrical resistivity (Left) and electronic phase diagram (Right) of $BaFe_2(As_{1-x}P_x)_2$ [16].

dependence of electrical resistivity shows the T-linear behavior and $|R_H|$ is enhanced at $x = 0.33$. These behaviors suggest that $x \sim 0.3$ is the quantum critical point (QCP) which shows non-Fermi liquid-like behaviors. T_c disappears and temperature dependence of electrical resistivity shows $\sim T^2$ behavior at $x \sim 0.7$. Not only chemical pressure but also physical pressure promotes superconductivity. T_c reaches 30 K under 4 GPa in the case of $BaFe_2As_2$ [17].

1.1.4   111-type iron pnictides

111-type iron pnictides are composed of $AFePn$ (A = Li, Na and Pn = P, As). The crystal structure of $AFePn$ is PbClF-type (tetragonal / $P4/nmm$) and illustrated in Figure 1.8 [18]. They have to be taken in inert gas to avoid reaction with air. LiFeAs and LiFeP are stoichiometric superconductors and T_c is 18 K and 5 K, respectively [19, 20]. Temperature dependence of electrical resistivity of both LiFeAs and LiFeP shows $\sim T^2$ behavior [21].
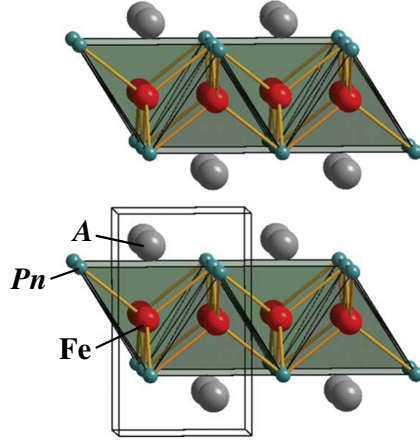
Figure 1.8: Crystal structure of AFePn [18]

1.1.5   42622-type iron pnictides

Representative 42622-type iron pnictides are $Sr_4V_2O_6Fe_2As_2$ ($T_c = 37$ K) [22], $Sr_4Sc_2O_6Fe_2P_2$ ($T_c = 17$ K) [23] and $Ca_4Al_2O_6Fe_2Pn_2$ ($Pn =$ As, P) ($T_c = 28$ K and 17 K) [24], which are stoichiometric superconductors. The crystal structure of $Sr_4Sc_2O_6Fe_2P_2$ (tetragonal, $P4/nmm$) is illustrated in Figure 1.9. $T_c = 17$ K of $Sr_4Sc_2O_6Fe_2P_2$ and $Ca_4Al_2O_6Fe_2P_2$ is the highest in
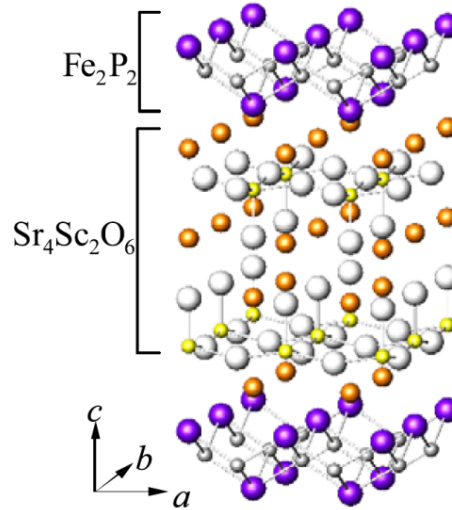
Figure 1.9: Crystal structure of $Sr_4Sc_2O_6Fe_2P_2$ [23].

pure iron phosphide superconductors.

P/As substitution effect is studied in $Ca_4Al_2O_6Fe_2Pn_2$ [25]. The electronic phase diagram of $Ca_4Al_2O_6Fe_2(As_{1-x}P_x)_2$ is shown in Figure 1.10. Interestingly, a new AFM order is discovered
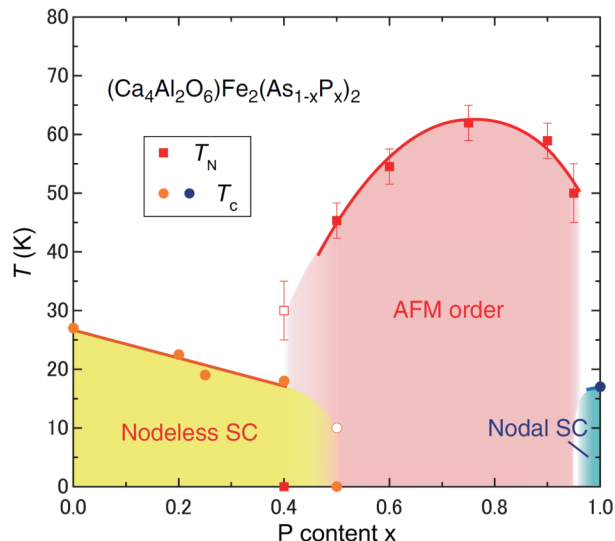
Figure 1.10: Electronic phase diagram of $Ca_4Al_2O_6Fe_2(As_{1-x}P_x)_2$ [25].

at $x = 0.5$ - 0.95 by the NMR measurement. The AFM order may be an essential one between nodal and nodeless superconducting states for many iron pnictide superconductors.

1.2　Theoretical studies on iron pnictide superconductors

1.2.1　Band structure and Fermi surfaces of 1111-type iron pnictides

The electronic states of LaFeAsO and LaFePO are predicted by band calculation [26]. As a result, five $3d$ electron bands per 1 Fe locate in the vicinity of Fermi level (E_F). Calculated band structures of LaFeAsO and LaFePO are shown in Figure 1.11. The unit cell is defined as that for 2 Fe atoms. In both cases of LaFeAsO and LaFePO, two hole bands (around Γ - Z) and two electron bands (around M - A) having d_{xz} and d_{yz} orbital characters cross E_F. Additionally, the 2-dimensional hole band having d_{xy} orbital character also crosses E_F around Γ - Z in LaFeAsO. On the other hand, the 3-dimensional band having d_{z^2} orbital character also crosses E_F around Z in LaFePO. This difference is not caused by the lattice constant a or c but the local crystal structural parameters of Pn around Fe. Calculated 3-dimensional Fermi surfaces (FSs) of LaFeAsO and LaFePO are illustrated in Figure 1.12. The unit cell is defined as that for 2 Fe atoms. 2-dimensional cylindrical FSs are predicted in both of LaFeAsO and LaFePO, which reflect strong 2-dimensionality of 1111 system. Three cylindrical hole FSs around Γ - Z and two cylindrical electron FSs around M - A are observed in LaFeAsO. On the
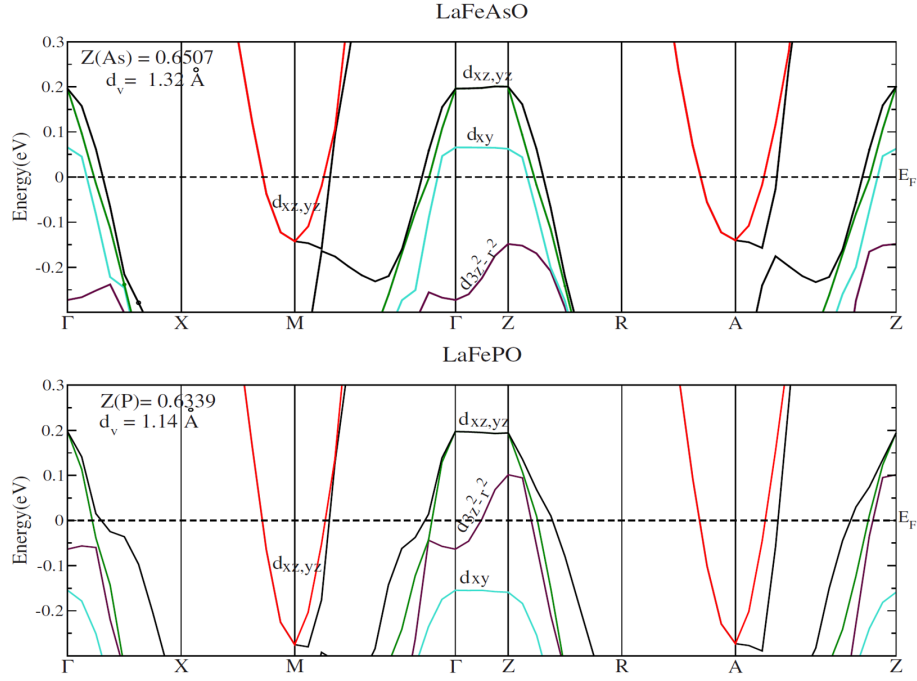
Figure 1.11: Calculated band structures of LaFeAsO (above) and LaFePO (below) [26]. The unit cell is defined as that for 2 Fe atoms.
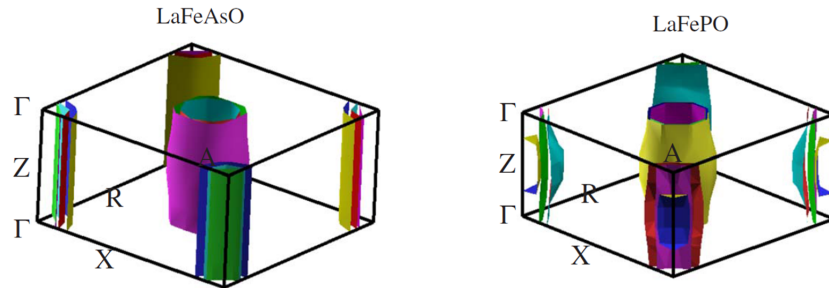
Figure 1.12: Calculated 3-dimensional FSs of LaFeAsO and LaFePO [26]. The unit cell is defined as that for 2 Fe atoms.

15

other hand, two cylindrical hole FSs around Γ - Z, two cylindrical electron FSs around M - A and one closed hole FS around Z are observed in LaFePO. 2-dimensionality of LaFeAsO is stronger than that of LaFePO. This tendency of FSs warping in iron phosphides confirmed in comparison between $BaFe_2As_2$ and $BaFe_2P_2$.

1.2.2   Spin fluctuation theory

The Cooper pair formation mechanism in iron based superconductors is not electron-phonon coupling because of the high T_c. Then the other superconducting mechanism mediated by spin fluctuation is discussed. $s_\pm$ superconducting gap state, whose sign is different between hole and electron FSs, is suggested by Kuroki *et al* [27]. 2-dimensional FSs of 1111 system and superconducting gap state are shown in Figure 1.13. The unit cell is defined as that for 1 Fe atom. In the case of RFeAsO, the FSs are shown in Figure 1.13 (Left). Nesting vectors are
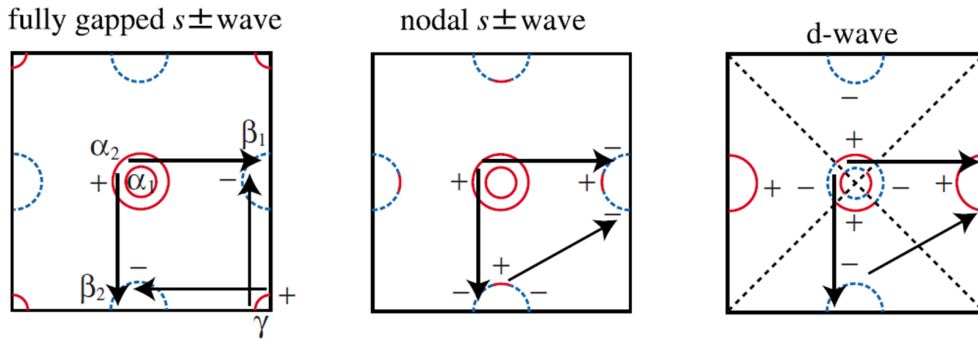
Figure 1.13: 2-dimensional FSs of 1111 system and nesting vectors between FSs [27]. The unit cell is defined as that for 1 Fe atom.

mediated to the direction of $(\pi, 0)$ and $(0, \pi)$. In the case of RFePO, the FSs are shown in Figure 1.13 (Center and Right). Nesting vectors are mediated to the direction of $(\pi, 0)$ and (π, π).

1.3   Experimental studies on iron pnictide superconductors

1.3.1   Correlations between crystal structural parameters and T_c

The mechanism to determine T_c of iron based superconductor is not clear yet. Phenomenologically, the correlation between Pn-Fe-Pn bond angle α and T_c is suggested by Lee *et al* [28]. α dependence of T_c (so-called 'Lee-plot') is presented in Figure 1.14. This plot suggests that
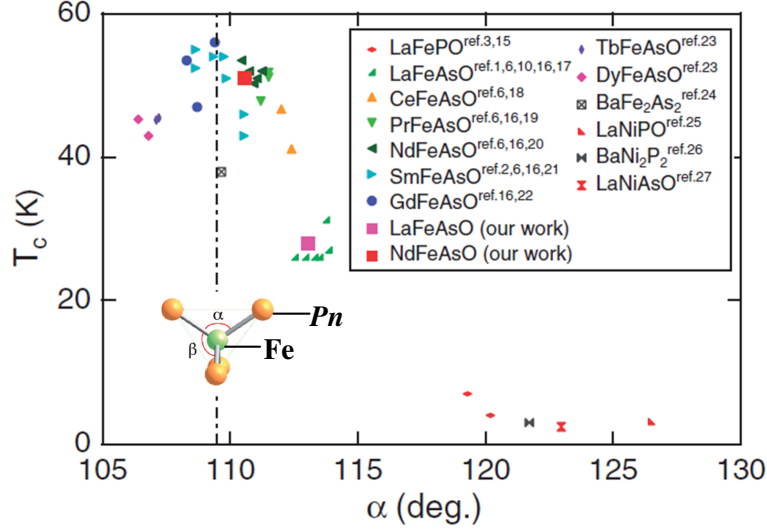
Figure 1.14: Pn-Fe-Pn bond angle α dependence of T_c [28].

T_c reaches the maximum value when α approaches $109.47°$, namely when $FeAs_4$ approaches regular tetrahedra. T_c increases from LaFeAsO to SmFeAsO and decreases from SmFeAsO to DyFeAsO in 1111 system. The bond angle α is regarded as the most important parameter by many researchers because of the clear correlation. However, iron phosphides, such as LiFeP, do not follow this plot. As a result, Lee-plot looks correct only in the special case that targets for comparison are iron arsenides and have the same crystal structure.

The other parameter to determine T_c was suggested by Kuroki et al. They suggest the pnictogen height from Fe-layer h_{Pn} is the key parameter to change FSs, nesting condition and superconducting gap structure. h_{Pn} dependence of T_c is presented in Figure 1.15. In this plot, iron arsenides with large h_{Pn} have higher T_c than iron phosphides with small h_{Pn}. This h_{Pn} plot is appropriate to expain the difference between FeAs and FeP systems in the same system.

1.3.2   Superconducting gap structure of various iron pnictide superconductors

According to the suggestion by Kuroki et al., the local crystal structural parameter of Pn around Fe can be a key parameter to determine T_c and superconducting gap symmetry. The local crystal structural parameter is quite different between the cases of Pn = P and As. Then previous studies on the superconducting gap structure are summarized below in order to compare those of iron arsenide and iron phosphide superconductors. The supercondcting gap symmetry
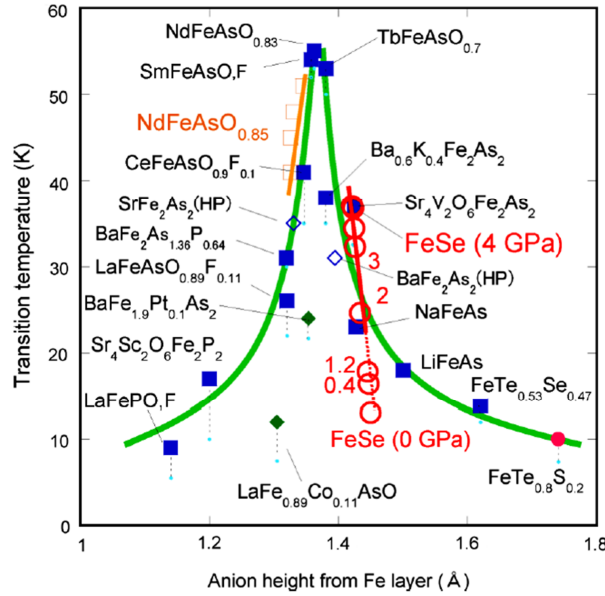
Figure 1.15: h_{Pn} dependence of T_c [29].

and size are often determined by measurements of magnetic penetration depth (MPD), angle-resolved photoemission spectroscopy (ARPES) and point-contact Andreev reflection (PCAR).

Magnetic penetration depth

Temperature dependence of MPD gives the information on superconducting gap symmetry. In the case of nodeless superconductors, the temperature dependence of MPD is described as

$$\frac{\Delta\lambda(T)}{\lambda(0)} \approx \sqrt{\frac{\pi\Delta}{2k_{\mathrm{B}}T}} \exp\left(-\frac{\Delta}{k_{\mathrm{B}}T}\right) \tag{1.1}$$

where Δ is superconducting gap size and $\Delta\lambda(T) = \lambda(T)$ - $\lambda(0)$. $\Delta\lambda(T)$ hardly shows temperature dependence at very low temperatures. On the other hand, in the case of nodal superconductors with line nodes, it is described as

$$\frac{\Delta\lambda(T)}{\lambda(0)} \approx \frac{\ln 2}{\Delta} k_{\mathrm{B}}T. \tag{1.2}$$

Then $\Delta\lambda(T)$ shows T-linear behavior.

Temperature dependence of MPD of 1111-type, 122-type and 111-type iron pnictide superconductors are presented in Figures 1.16, 1.17 and 1.18 (Left) [30, 31, 32, 33]. Temperature dependence of $\Delta\lambda(T)$ of LaFePO, BaFe$_2$(As$_{0.67}$P$_{0.33}$)$_2$ and LiFeP shows T-linear behavior at very low temperatures. Therefore, nodal superconducting gap state arises in these iron phosphide
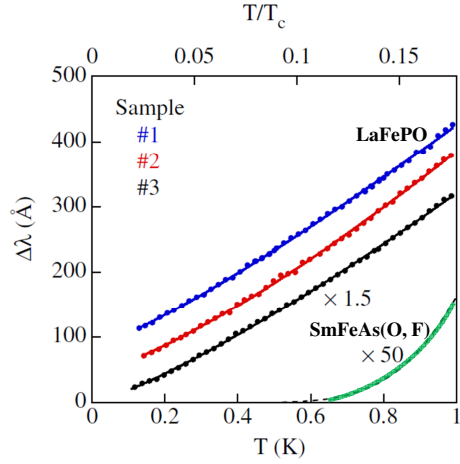
Figure 1.16: Temperature dependence of MPD of 1111-type iron pnictide superconductors [30, 31].
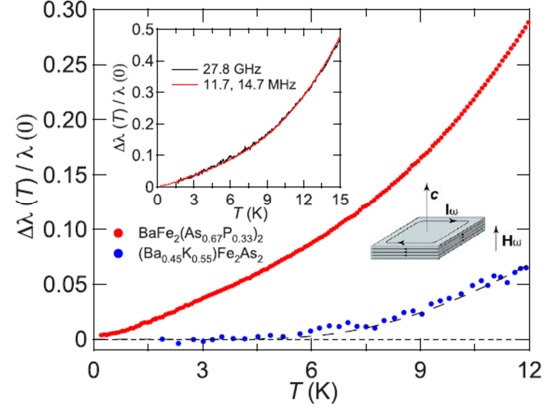
Figure 1.17: Temperature dependence of MPD of 122-type iron pnictide superconductors [32].
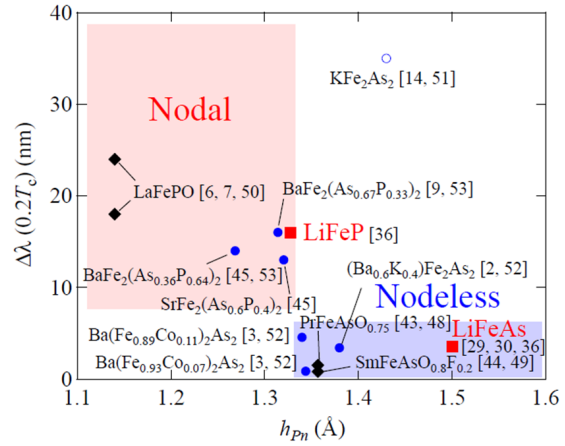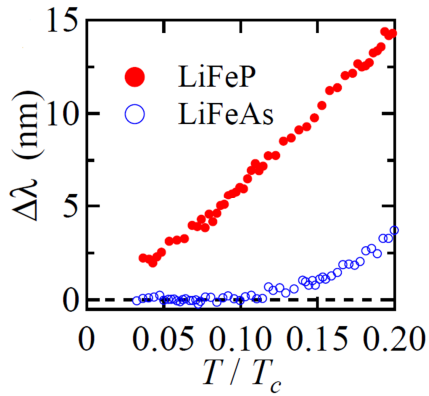
Figure 1.18: Temperature dependence of MPD of 111-type iron pnictide superconductors (Left) and the correlation between h_{Pn} and $\Delta\lambda(T)$ at $T = 0.2T_{\mathrm{c}}$ (Right) [33].

superconductors. On the other hand, $\Delta\lambda(T)$ of SmFeAs(O, F), $Ba_{0.45}K_{0.55}Fe_2As_2$ and LiFeAs hardly shows temperature dependence and it is nearly zero. Then, nodeless superconducting gap state arises in these iron arsenide superconductors.

The correlation between h_{Pn} and $\Delta\lambda(T)$ at $T = 0.2\,T_c$ is presented in Figure 1.18 (Right) [33]. According to the plot, iron arsenide superconductors with large h_{Pn} have small $\Delta\lambda(T)$ and it reflects the nodeless superconducting gap state, except for heavily hole-doped KFe_2As_2. On the other hand, iron phosphide superconductors with low h_{Pn} have large $\Delta\lambda(T)$ and it suggests the nodal superconducting gap state. $h_{Pn} = 1.34$ Åis the boundary of nodal and nodeless states in this plot.

Angle-resolved photoemission spectroscopy

Superconducting gap causes the decrease of the density of state (DOS) on the energy distribution curve (EDC) spectrum in ARPES measurements. Superconducting gap size is estimated by the difference between Fermi level and the edge of EDC spectrum. Superconducting gap symmetry is determined by the measurement of the superconducting gap size of each position on the FS. Superconducting gap of $NdFeAsO_{0.85}F_{0.15}$ and $Ba_{0.6}K_{0.4}Fe_2As_2$ are shown in Figures 1.19 and 1.20 [34, 35]. One nodeless superconducting gap with $\Delta = 15$ meV on the hole FS is
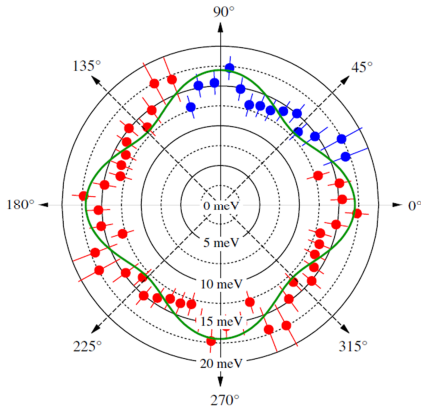
Figure 1.19: Superconducting gap of $NdFeAsO_{0.85}F_{0.15}$ [34].
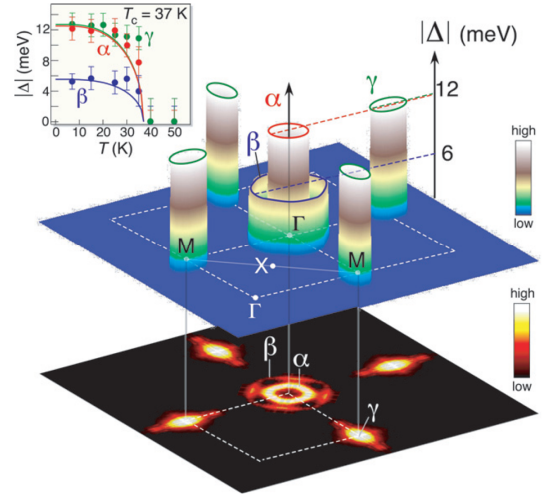
Figure 1.20: Superconducting gap of $Ba_{0.6}K_{0.4}Fe_2As_2$ [35].

observed in $NdFeAsO_{0.85}F_{0.15}$. Two nodeless superconducting gap with $\Delta = 12$ meV on inner hole and electron FSs and one nodeless superconducting gap with $\Delta = 6$ meV on outer hole FS are observed in $Ba_{0.6}K_{0.4}Fe_2As_2$.

On the other hand, superconducting gap structures of pure iron phosphide superconductors, such as RFePO, LiFeAs and $Sr_4Sc_2O_6Fe_2P_2$, are not observed in ARPES measurements because of the low T_c or the difficulty to obtain large single crystals. Instead of pure iron phosphides, superconducting gap structure of $BaFe_2(As, P)_2$ is measured by some groups. According to the ARPES measurement by Feng *et al.*, the superconducting gap on the outer hole FS goes to zero around Z, namely horizontal line nodes are suggested on the outer hole FS around Z [36]. However, the nodal loop structure on electron FSs is suggested by the angle-resolved thermal conductivity measurement [37]. Then the location of the superconducting gap node has not been consented.

Point-contact Andreev reflection

PCAR is also a tool to determine the gap structure. If one incident electron with the energy $E < \Delta$ is shot from a metal to a superconductor with the superconducting gap energy Δ, one Cooper pair is formed in the superconductor and one hole is reflected on the interface between the metal and the superconductor (Andreev reflection). In principle, the electrical conductivity is enhanced twice than the normal conductivity. If $E > \Delta$, Andreev reflection does not occur and the electrical conductivity does not change. These behaviors are analyzed by the Blonder, Tinkham and Klapwijk (BTK) model and the superconducting gap size and symmetry are calculated. Unlike MPD and ARPES measurements, PCAR can be measured by using polycrystalline samples.

In the studies on iron-based superconductors, similar results on the superconducting gap structure to MPD and ARPES measurements are observed in many 1111 and 122 systems. As the original achievement of PCAR spectroscopy, polycrystalline $Sr_4Sc_2O_6Fe_2P_2$ is measured [38]. As a result, a zero-bias conduction peak, which is the evidence of nodal superconducting gap, is observed in the measurement.

Summary

Almost all experiments of MPD, ARPES and PCAR suggest that nodeless superconductivity emerges in iron arsenide superconductors and nodal superconductivity emerge in iron phosphide superconductors. This difference between iron arsenides and iron phosphides seems to be caused by the difference of local crystal structural parameters of Pn around Fe, such as h_{Pn} and α. In addition to that fact, the existence of the AFM order between nodal and node-

less superconducting states is also suggested by Mukuda *et al.* from the NMR measurement of $Ca_4Al_2O_6Fe_2(As_{1-x}P_x)_2$ [25]. The AFM order, the nodal and nodeless superconducting states, which are plotted in the 2-dimensional plane of structural parameters of the nearest-neighbor Fe-Fe distance a_{Fe-Fe} and h_{Pn}, is shown in Figure 1.21.
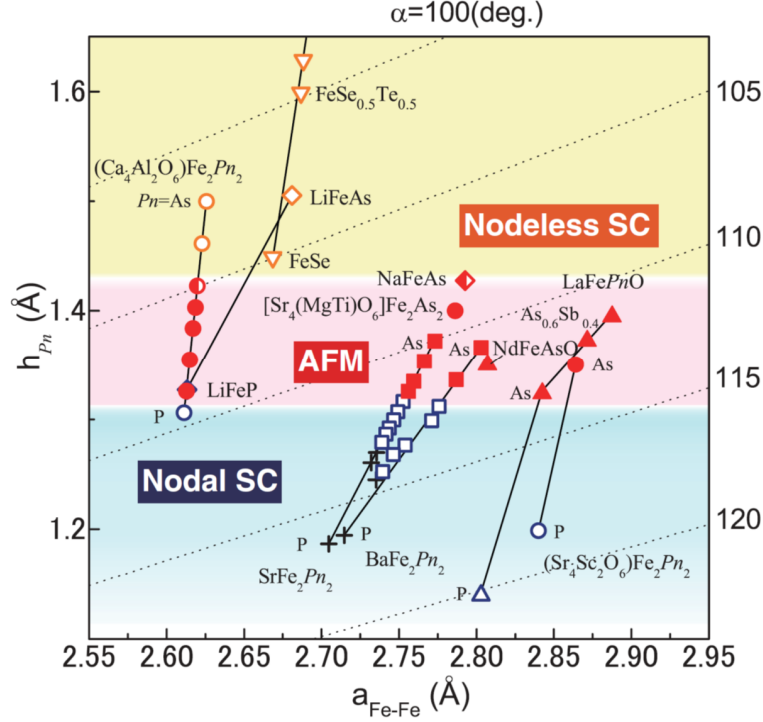
Figure 1.21: The AFM order, the nodal and nodeless superconducting states in iron-based superconductors. They are plotted in the 2-dimensional plane of structural parameters of the nearest-neighbor Fe-Fe distance a_{Fe-Fe} and h_{Pn} [25].

1.3.3   P/As substitution studies on 1111-type iron pnictides

P/As substitution changes the local crystal structural parameters around Fe effectively. There are several reports on P/As substitution effect in 1111-type iron pnictides.

LaFeP$_{1-x}$As$_x$O$_{1}-y$F$_y$

The electronic phase diagram of $LaFeP_{1-x}As_xO_{1-y}F_y$ ($y = 0$, 0.05, 0.1) is presented in Figure 1.22, where the result of $LaFeP_{1-x}As_xO_{0.9}F_{0.1}$ is my data in this thesis. In the case of $y = 0$, two superconducting domes (SC1 and SC2) are observed and SC1 dome seems to occur in the vicinity of QCP. Additionally, a new AFM order (AFM2) between SC1 and SC2 is also detected
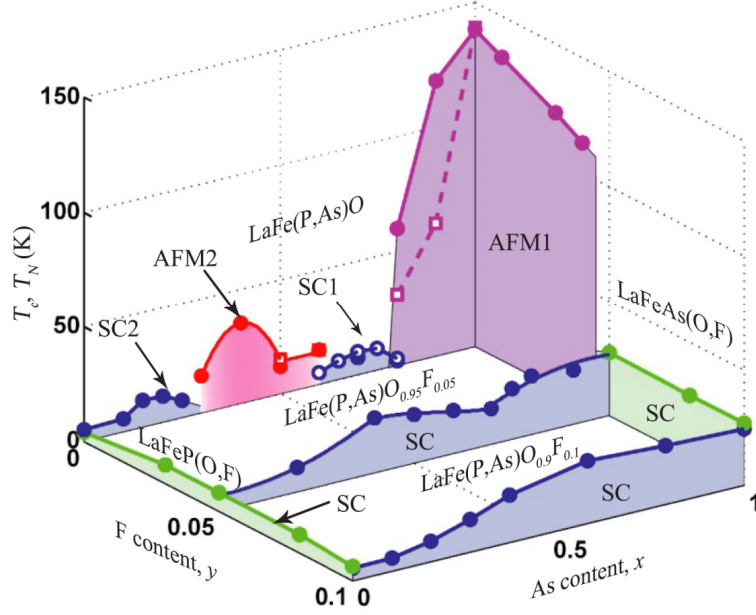
Figure 1.22: Electronic phase diagram of LaFeP$_{1-x}$As$_x$O$_{1-y}$F$_y$ (y = 0, 0.05, 0.1) [39].

by the NMR measurement. The emergence of the new AFM order in P/As substitution system is also observed in Ca$_4$Al$_2$O$_6$Fe$_2$(As$_{1-x}$P$_x$)$_2$. In the case of y = 0.05, superconductivity emerges in all x region. The maximum T_c is observed at x = 0.4 and 1.0, where AFM order exists at y = 0. Therefore, the correlation between superconductivity and AFM fluctuation is suggested. In the case of y = 1.0, T_c increases with x in the region of x = 0 - 0.6 and does not change in the region of x = 0.6 - 1.0 at y = 0.1.

CeFeAs$_{1-x}$P$_x$O and CeFeAs$_{1-x}$P$_x$O$_{0.95}$F$_{0.05}$

Electronic phase diagrams of CeFeAs$_{1-x}$P$_x$O and CeFeAs$_{1-x}$P$_x$O$_{0.95}$F$_{0.05}$ are shown in Figure 1.23 [40, 41]. As for CeFeAs$_{1-x}$P$_x$O, in the case of CeFeAsO, structural and magnetic phase transitions occur at T_s and $T_N \sim$ 140K and AFM order caused by $4f$ electron of Ce emerges at T_N = 4 K. On the other hand, CeFePO is the heavy fermion system. The AFM order caused by $3d$ electron of Fe disappears at x = 0.4 and FM order emerges at x = 0.35 - 0.9. The disappearance of structural and magnetic phase transitions is confirmed by the neutron scattering measurement. Then x = 0.4 is regarded as QCP.

As for CeFeAs$_{1-x}$P$_x$O$_{0.95}$F$_{0.05}$, superconductivity emerges at x = 0 - 0.55 and FM order of Ce emerges at x = 0.45 - 1.0.
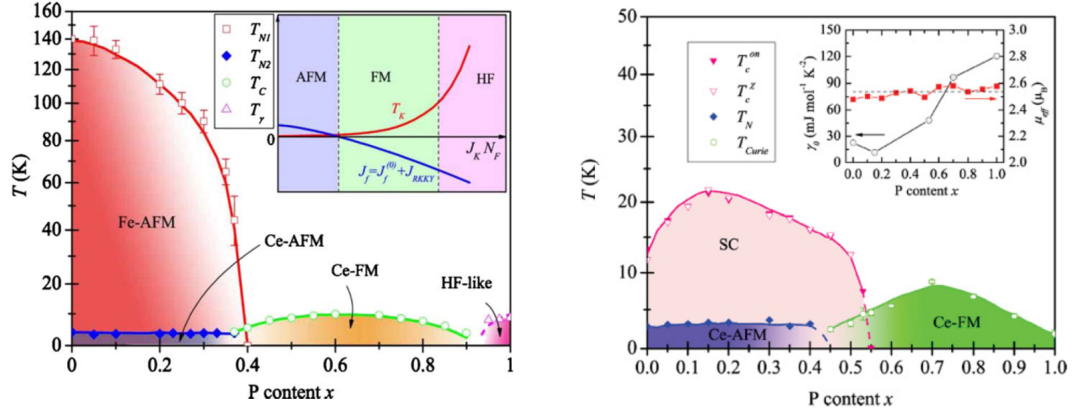
Figure 1.23: Electronic phase diagrams of CeFeAs$_{1-x}$P$_x$O (Left) and CeFeAs$_{1-x}$P$_x$O$_{0.95}$F$_{0.05}$ (Right) [40, 41].

SmFeAs$_{1-x}$P$_x$O

Temperature dependence of electrical resistivity of SmFeAs$_{1-x}$P$_x$O is shown in Figure 1.24 [42]. Superconductivity emerges at $x = 0.565$. This behavior is similar to LaFeP$_{0.3}$As$_{0.7}$O.
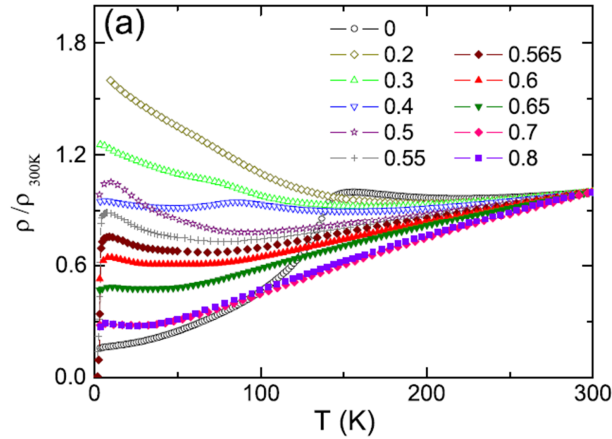
Figure 1.24: Temperature dependence of electrical resistivity of SmFeAs$_{1-x}$P$_x$O [42].

1.3.4   ARPES measurements in 1111 system

LaFePO and LaFeAsO

FS mapping at $k_z = 0$ of LaFePO and LaFeAsO is presented in Figure 1.25 [43, 44]. As for LaFePO, one large hole FS and two small hole FSs are observed around Γ. The two small FSs are nearly degenerated. Two electron FSs are observed around M. The positions and the
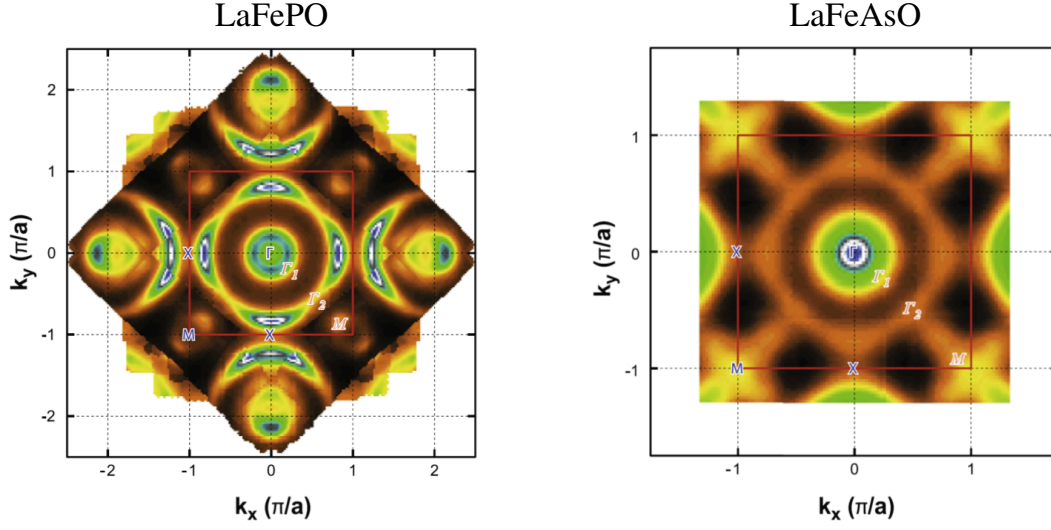
Figure 1.25: FS mapping at $k_z = 0$ of LaFePO (Left) and LaFeAsO (Right) [43, 44]

sizes of the two small hole FSs and the two electron FSs are nearly consistent with theoretical calculation. As for LaFeAsO, one large hole FS, one small hole FS and one pseud-hole FS are observed around Γ. Two electron FSs are observed around M. The largest hole FS is observed in all ARPES measurements of 1111 system, but the enlargement of the hole FS is quite unlikely because of the electrical neutrality.

FSs of LaFePO is also observed by the measurement of the de Haas-van Alphen (dHvA) effect [45]. The FSs of LaFePO determined by the dHvA measurement is shown in Figure 1.26. Two hole FSs and two electron FSs are detected, but one small 3-dimensional hole FS around Z is not observed. The large hole FS in the ARPES measurements is not detected. Therefore, the large hole FS may be caused by the surface effect.

PrFeAsO$_{0.7}$

FS mapping at $k_z = 0$ of PrFeAsO$_{0.7}$ is shown in Figure 1.27 [46]. Three hole FSs around Γ and clover-shaped electron FSs around M are reported. The clover-shaped electron FSs are also reported in heavyly hole-doped KFe$_2$As$_2$. This suggests that the electronic neutrality may be not obtained in the cleaved surface and the reconstruction of electronic state may occur on the sample surface.
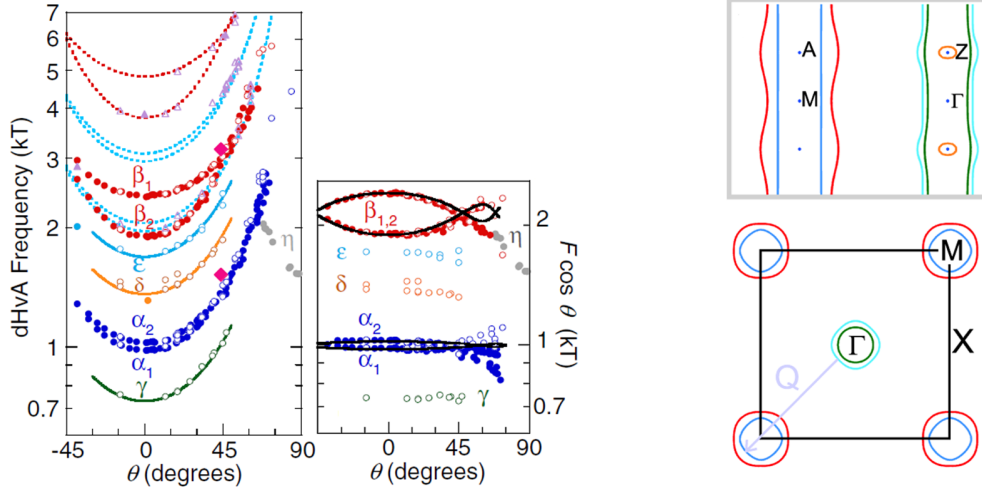
Figure 1.26: FSs of LaFePO observed in the dHvA measurement [45].
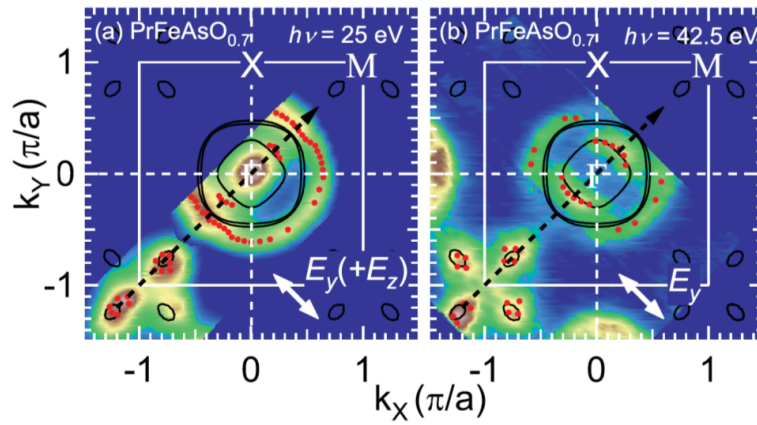
Figure 1.27: FS mapping at $k_z = 0$ of PrFeAsO$_{0.7}$ [46].

NdFeAsO$_{0.85}$F$_{0.15}$

FS mapping at $k_z = 0$ of NdFeAsO$_{0.85}$F$_{0.15}$ is shown in Figure 1.28 [34]. One large hole FS around Γ and one electron FS around M are observed. The nodeless superconducting gap with $\Delta = 15$ meV is reported on the hole FS.
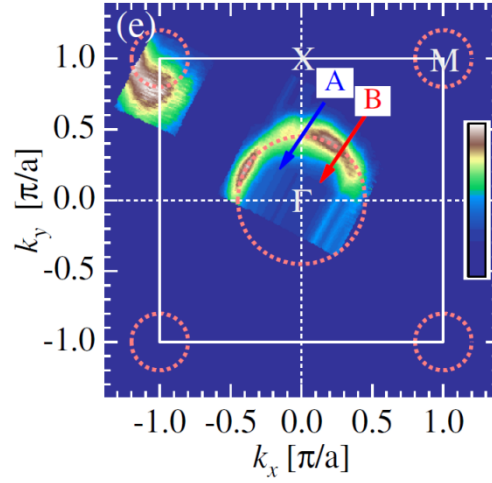
Figure 1.28: FS mapping at $k_z = 0$ of NdFeAsO$_{0.85}$F$_{0.15}$ [34].

SmFeAsO

FS mapping at $k_z = 0$ of SmFeAsO is shown in Figure 1.29 [47]. The large hole FS around Γ is also reported and it is ascribed to the surface effect.
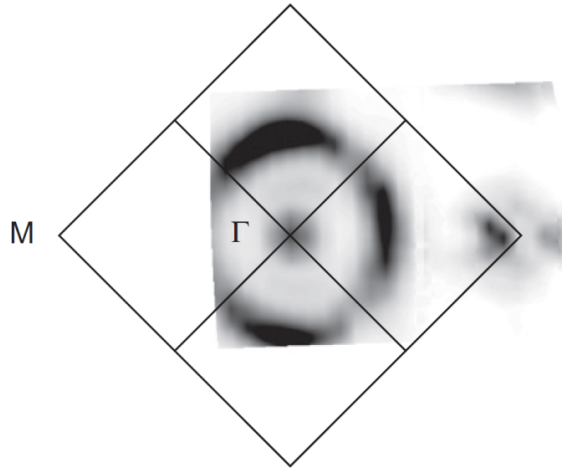
Figure 1.29: FS mapping at $k_z = 0$ of SmFeAsO [47].

Chapter 2

Objective

Recently discovered iron-based superconductors have the second highest T_c following cuprates. They are important substances to clarify the superconducting mechanism with high T_c. In 1111-type iron pnictide superconductors RFePnO, T_c, the structural and magnetic properties are different between R = As and R = P. In the case of RFeAsO, superconductivity emerges together with the suppression of the structural and magnetic transitions by F doping or F deficiency, and the maximum T_c reaches $\sim$ 55 K, which is the highest in iron-based superconductors. On the other hand, no structural and magnetic transitions exist and T_c is $\sim$ 5 K in the case of RFePO. Some empirical rules are proposed to explain the difference of T_c from the view point of the local crystal structural parameters around Fe, such as bond angle α and pnictogen height h_{Pn}. However, it is not clear yet what electronic parameter is modified by these structural parameters. Although, some theories suggest that the antiferromagnetic fluctuation plays an important role for the appearance of superconductivity in the iron-based superconductors, there is no direct experimental evidence that T_c is correlated with the strength of antiferromagnetic fluctuation.

In order to find the key parameter to determine the T_c of iron-based superconductors, I studied P/As substitution effect of 1111-type iron pnictide superconductors by using transport and ARPES techniques. This P/As substituted 1111 system is appropriate to study the above relationship because (i) superconductivity emerges in both of RFeAs(O, F) and RFeP(O, F), (ii) T_c, the local crystal structural parameters around Fe and perhaps strength of antiferromagnetic fluctuation drastically change with the substitution.

In part II, I present the studies on polycrystalline RFeP$_{1-x}$As$_x$O$_{0.9}$F$_{0.1}$ (R = La, Pr, Nd). The purpose is to study the relationship among crystal structural parameters, T_c and transport properties in various R systems having various T_c, and to find the key parameter for supercon-

ductivity. The composition dependence of the crystal structural parameters, T_c and transport properties are discussed and several suggestive results are obtained. As results of the electrical resistivity measurements, two different superconducting x regions are suggested from x dependence of T_c and n, which is defined from $\rho(T) = \rho_0 + AT^n$. In the region of $x < 0.6$ - 0.8, T_c and n correlate and T_c increases by the enhancement of AFM fluctuation. On the other hand, in the region of $x > 0.6$ - 0.8, no clear relationship between T_c and n is observed. Two scaling lines are also observed in the correlation between T_c and n and the different scaling lines may reflect the different FSs and nesting vectors.

In part Ⅲ, I studied on single-crystalline $NdFeP_{1-x}As_x(O, F)$. There are mainly three objectives to launch this study. First, I would like to establish the single crystal growth method of 1111-type iron pnictide superconductors because it is very difficult to obtain large-sized single crystals in 1111 system and successful examples are few in the world. Second, the transport properties including the anisotropy and no grain boundary effect can be measured by using the single-crystalline samples. The results also tell us whether the polycrystalline results in part Ⅱ are intrinsic or not. Third, the band dispersion and the FSs are directly observed by the ARPES measurement. The third is the most important in this P/As substitution study. I would like to clarify the difference of the FS configuration between below and above $x = 0.6$ - 0.8 where T_c and n show distinct x dependences.

Part II

Studies on Polycrystalline RFeP$_{1-x}$As$_x$O$_{0.9}$F$_{0.1}$ (R = La, Pr, Nd)

Chapter 3

Experimental methodology

3.1 Synthesis

All processes of weighting and mixing the raw materials in this study were performed in an Ar-filled glove box. Both concentrations of O_2 and H_2O in the glove box were kept less than 10 ppm.

3.1.1 Synthesis of precursors RAs and RP (R = La, Pr, Nd)

R (= La, Pr, Nd) (3N, KOJUNDO CHEMICAL LABORATORY CO.,LTD (KCL.)), As (6N, FURUKAWA DENSHI CO.,LTD.) and P (5N, KCL.) were used to synthesize the precursors of RAs and RP. First, R chips held in spindle oil were cleaned with hexane in order to remove the oil before the synthesis. This procedure was operated by using an ultrasonic cleaning device in the sequence of 10 min $\times$ 3 times. The mixture of R and hexane was filtered with a filtering paper. The remnant hexane around R was vaporized in vacuum and the cleaned R chips were stored in the globe box. Next, R and As (P) were mixed with the stoichiometric ratio of 1 : 1 and sealed in an evacuated silica tube ($\sim 10^{-6}$ Torr) with the external diameter of 13 mm and the internal diameter of 11 mm. To prevent the explosion of the silica tube during heating, the length of sealed silica tubes should be 16 - 18 cm and the weights of As and P should be less than 1.0 g and 0.4 g, respectively. The R and As (P) in the sealed silica tube were heated and reacted at 900 °C (850 °C) in an electrical furnace. Temperature conditions for synthesis of RAs and RP are illustrated in Figures 3.1 and 3.2, respectively.
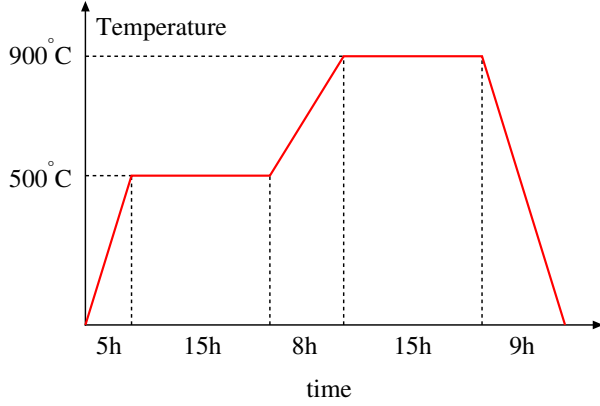
Figure 3.1: The temperature condition for synthesis of RAs.
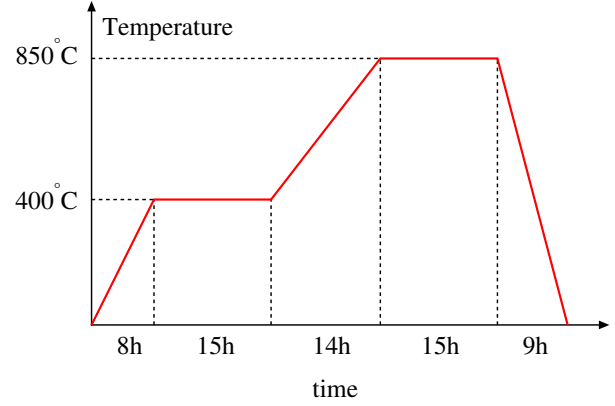
Figure 3.2: The temperature condition for synthesis of RP.

3.1.2   Synthesis of polycrystalline RFeP$_{1-x}$As$_x$O$_{0.9}$F$_{0.1}$ (R = La, Pr, Nd)

RAs, RP, Fe$_2$O$_3$ (4N, KCL.), Fe (5N, KCL.), FeF$_2$ (2N, RARE METALLIC Co.,LTD.) and RF$_3$ (5N, KCL.) were used as starting materials to synthesize polycrystalline RFeP$_{1-x}$As$_x$O$_{0.9}$F$_{0.1}$. Each starting material was weighted with a composition of RFeP$_{1-x}$As$_x$O$_{1-y-\delta}$F$_y$. The O deficiency δ was introduced to the samples in order to make F substitution easy and subtract excess O introduced during the synthesis process. The δ value (~ 0.1) is not noted in the later chapters and sections. Many researchers who studies on P/As substituted iron pnictides often define iron arsenides as main phases and x as P substitution ratio for As site, such as BaFe$_2$(As$_{1-x}$P$_x$)$_2$ and Ca$_4$Al$_2$O$_6$Fe$_2$(As$_{1-x}$P$_x$)$_2$. In my thesis, however, I defined iron phosphides as main phases and x as As substitution ratio for P site (e.g. P$_{1-x}$As$_x$) because my experimental results showed systematic changes with x in the vicinity of iron phosphides.

The chemical reaction formula of RFeP$_{1-x}$As$_x$O$_{1-y}$F$_y$ in the case of using FeF$_2$ is

$$x\,R\text{As} + (1-x)\,R\text{P} + \frac{(1-y-\delta)}{3}\,\text{Fe}_2\text{O}_3 + \frac{(2+y+4\delta)}{6}\,\text{Fe} + \frac{y}{2}\,\text{FeF}_2$$

$$\longrightarrow R\text{FeP}_{1-x}\text{As}_x\text{O}_{1-y-\delta}\text{F}_y$$
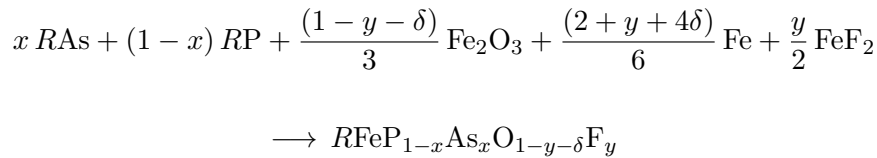
The chemical reaction formula in the case of using RF$_3$ is

$$\frac{x(3-y)}{3}\,R\text{As} + \frac{(1-x)(3-y)}{3}\,R\text{P} + \frac{(1-y-\delta)}{3}\,\text{Fe}_2\text{O}_3 + \frac{(1+2y+2\delta)}{3}\,\text{Fe} + \frac{y}{3}\,R\text{F}_3 + \frac{xy}{3}\,\text{As} + \frac{(1-x)y}{3}\,\text{P}$$
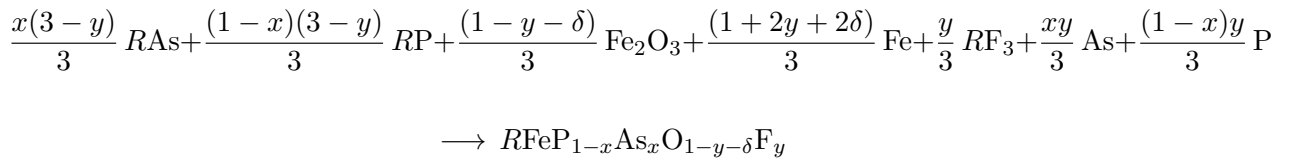
$$\longrightarrow R\text{FeP}_{1-x}\text{As}_x\text{O}_{1-y-\delta}\text{F}_y$$

In this study, FeF_2 was used in the cases of $R = Pr$ and Nd, while RF_3 was used in the case of $R = La$.

Materials of RAs, RP, Fe_2O_3, Fe, FeF_2 or RF_3 were weighted, following the ratio in the above formula and mixed in an agate mortar for 20 minutes. Then the mixture was pressed into a pellet (1.0 - 1.5 g) under the pressure of 20 MPa. The pellet was sealed in an evacuated silica tube and reacted at 1100 °C. The pellet sealed in the evacuated silica tube is shown in Figure 3.3. Temperature conditions for the synthesis of $RFeP_{1-x}As_xO_{0.9}F_{0.1}$ is illustrated in Figure 3.4.
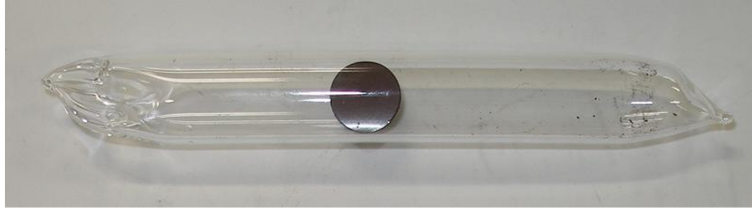
Figure 3.3: The pellet ($\phi = 10$ mm) sealed in the evacuated silica tube.
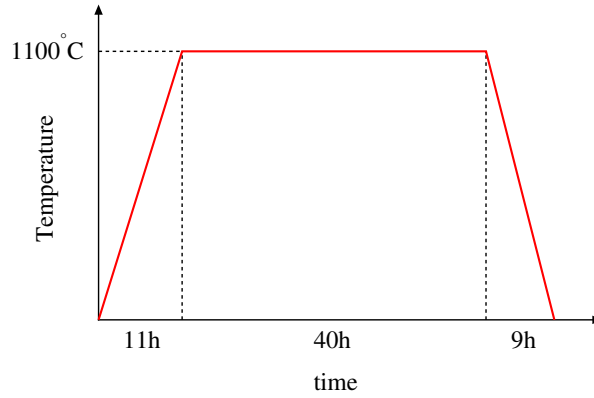
Figure 3.4: The temperature condition for the synthesis of $RFeP_{1-x}As_xO_{0.9}F_{0.1}$.

Polycrystalline samples with the following nominal compositions were synthesized.

- $LaFeP_{1-x}As_xO_{0.9}F_{0.1}$ ($x = 0$, 0.1, 0.2, 0.3, 0.4, 0.6, 0.8, 1.0)

- $PrFeP_{1-x}As_xO_{0.9}F_{0.1}$ ($x = 0$, 0.2, 0.4, 0.6, 0.8, 0.9, 1.0)

- $NdFeP_{1-x}As_xO_{0.9}F_{0.1}$ ($x = 0$, 0.2, 0.4, 0.5, 0.6, 0.7, 0.8, 1.0)

Hereafter, I use the nominal concentrations of F (0.1) and As (x).

3.2   Measurements

3.2.1   Crystal structural analysis

Powder X-ray diffraction in Laboratory

Powder X-ray diffraction is a standard tool to evaluate lattice parameters and impurity concentrations of a polycrystalline sample. It was measured by using MiniFlex and RINT-2000 (Rigaku Co.).

First, a piece of a polycrystalline sample was crushed and powdered with an agate mortar. Then the powder of the sample was stuck on a glass plate and they were set up on the above machines. Bragg peaks were detected by $\theta - 2\theta$ scan in the range of $2\theta = 20$ - 100 °. X-ray source was Cu and $K_{\alpha 1}$ radiation ($\lambda = 1.5406$ Å) without $K_{\alpha 2}$ one was used for analysis. The lattice constants were obtained by the least squares fitting of the X-ray diffraction profile.

Synchrotron X-ray diffraction

Synchrotron X-ray diffraction using X-ray with strong intensity is able to determine accurate crystal structural parameters including atomic positions and atomic occupancies. They are essential information for iron-based superconductors where T_c is sensitive to those parameters. Synchrotron X-ray diffraction was measured at the beam line BL-8A in Photon Factory (PF) in KEK, Tsukuba, Japan.

A piece of a polycrystalline sample was powdered over 1 hour and then inserted into a glass capillary tube with the internal diameter of 200 μm. The powder X-ray diffraction measurements were performed at 300 K by using X-ray with the energy of 15 keV. Crystal structural parameters were determined by Rietveld analysis [48].

3.2.2   Magnetic susceptibility

Magnetic susceptibility measurement is an appropriate tool to detect T_c and superconducting volume fraction because it is dramatically changed by diamagnetism of superconductivity. Temperature dependence of magnetic susceptibility was measured by using MPMS-7 (Quantum Design, Inc.) under the magnetic field of 10 Oe in both conditions of zero field cooling (ZFC) and field cooling (FC). The χ value was defined as the averaged measurement value in three times.

3.2.3   Electrical resistivity

Electrical resistivity measurement is also an appropriate tool to detect T_c through zero-resistivity of superconductivity. The detail of temperature dependent resistivity in the normal state was also studied in this work. It was measured by using conventional four-probe method. A sample was shaped to about $1 \times 1 \times 3\,\mathrm{mm^3}$ cuboid by polishing with a sand paper. Au wires ($\phi = 25\,\mu$m, The Nilaco Co.) were connected on the sample with DOTITE (FUJIKURA KASEI CO.,LTD.) silver paste as electrodes. The configuration of sample and electrodes for electrical resistivity measurement is shown in Figure 3.5. Cooling temperature for the measurement was
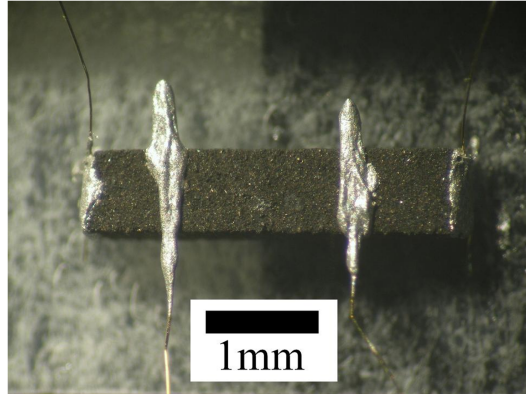
Figure 3.5: The configuration of sample and electrodes for electrical resistivity measurement (inner: voltage probes, outer: current probes).

controlled in He vessel. Electrical resistivity ρ was calculated by the equation

$$\rho = R\,\frac{S}{l} \tag{3.1}$$

where R, S and l are the resistance, the sample cross-section area and the distance between voltage probes, respectively.

3.2.4   Hall effect

Hall effect measurement is a tool to determine a sign of carriers and carrier density. Hall effect was measured by using MPMS to control magnetic field. Sample probe holder was specially designed for four-probe method to detect Hall resistivity. A sample was shaped to about $1.5 \times 1.5 \times 0.25\,\mathrm{mm^3}$. Current and voltage probes were made with the same method of the measurement of electrical resistivity. The configuration of sample and electrodes for Hall effect measurement

is shown in Figure 3.6.
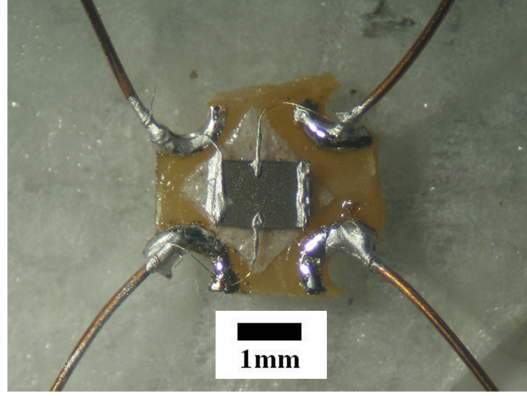
Figure 3.6: The configuration of sample and electrodes for Hall effect measurement (top and bottom: voltage probes, left and right: current probes).

When the magnetic field H is applied, the resistance $R(H)$ contains not only Hall resistance $R_{xy}(H)$ but also a part of the normal resistance $R_{xx}(H)$. Then $R(H)$ is written as

$$R(H) = R_{xx}(H) + R_{xy}(H). \tag{3.2}$$

On the other hand, $R(-H)$ is written as

$$
\begin{aligned}
R(-H) &= R_{xx}(-H) + R_{xy}(-H) \\
&= R_{xx}(H) - R_{xy}(H).
\end{aligned}
\tag{3.3}
$$

From the above two equations, Hall resistance $R_{xy}(H)$ is written as

$$R_{xy}(H) = \frac{R(H) - R(-H)}{2}. \tag{3.4}$$

Hall resistivity ρ_{xy} is calculated by the equation,

$$\rho_{xy}(H) = R_{xy}(H)\,\frac{Wd}{l}. \tag{3.5}$$

where W, d and l are the sample width, the sample thickness and the distance of voltage probes, respectively. When voltage probes are putted on lateral side, $l \approx W$. Then $\rho_{xy}(H)$ is written as

$$\rho_{xy}(H) \approx R_{xy}(H)\,d. \tag{3.6}$$

From above equation, the thickness d should be small to obtain large $R_{xy}(H)$ signal. $\rho_{xy}(H)$ was fitted with the formula

$$\rho_{xy}(H) = c_1 H + c_2 H^3 \tag{3.7}$$

and Hall coefficient R_{H} was determined as the first gradient to the magnetic field, namely

$$c_1 = R_{\mathrm{H}}. \tag{3.8}$$

The typical measurement current was $I = 10$ mA and magnetic field was changed from H = -7 T to 7 T. The accurate R(H) value was defined as the average value for 10 times measurements.

Chapter 4

Experimental results

4.1 Crystal structural analysis

4.1.1 Powder X-ray diffraction

Powder diffraction patterns of $LaFeP_{1-x}As_xO_{0.9}F_{0.1}$, $PrFeP_{1-x}As_xO_{0.9}F_{0.1}$ and $NdFeP_{1-x}As_xO_{0.9}F_{0.1}$ measured by MiniFlex or RINT-2000 are shown in Figures 4.1, 4.2 and 4.3. Positions and in-
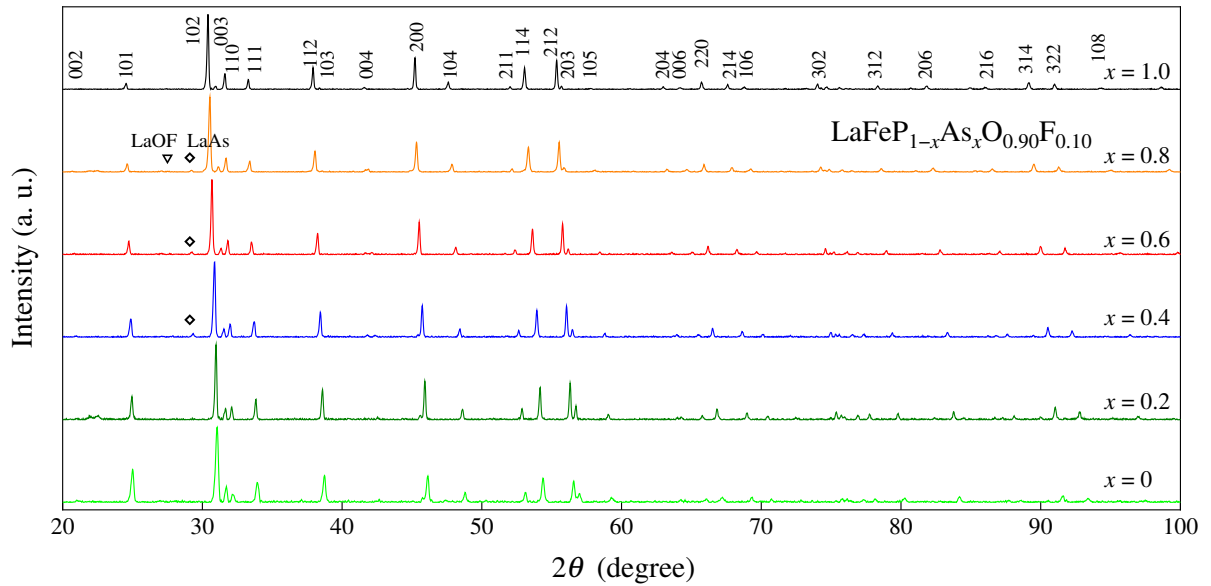
Figure 4.1: Powder X-ray diffraction patterns of $LaFeP_{1-x}As_xO_{0.9}F_{0.1}$.

tensities of Bragg peaks are consistent with the previous reports on 1111 system. As shown in Figures 4.1, 4.2 and 4.3, almost all the diffraction peaks are indexed assuming the tetragonal structure with the $P4/nmm$ symmetry. Bragg peaks systematically shift to lower angle with

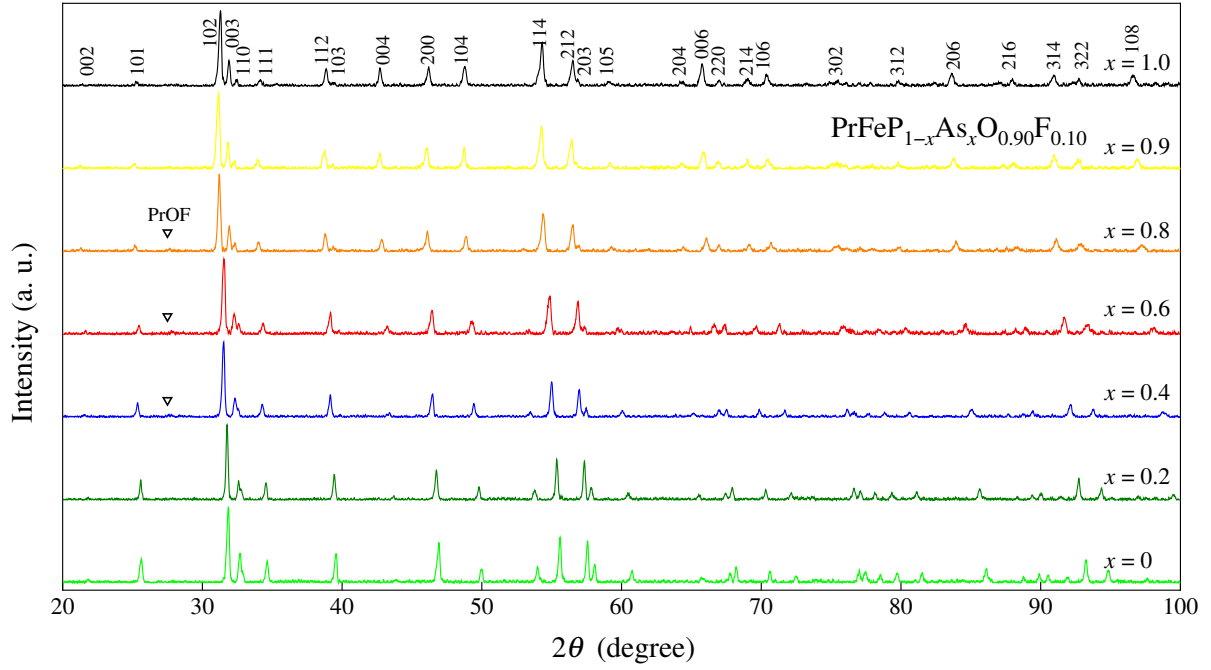Figure 4.2: Powder X-ray diffraction patterns of $PrFeP_{1-x}As_xO_{0.9}F_{0.1}$.
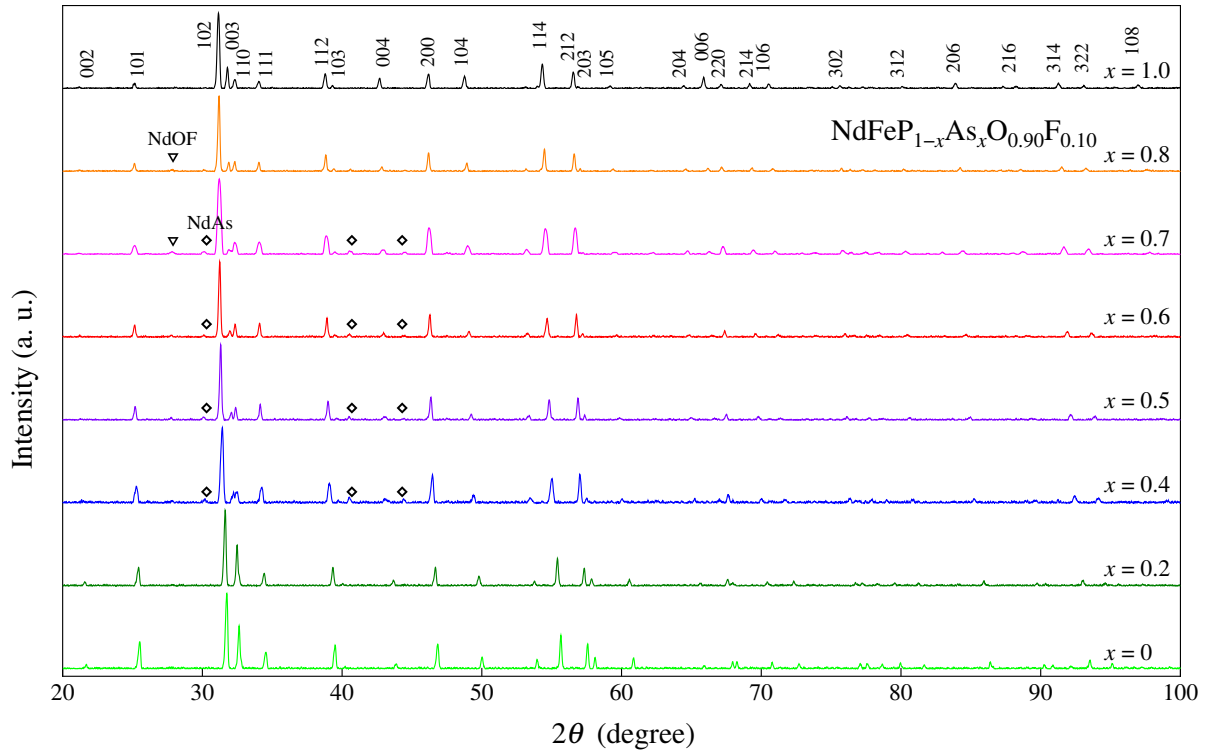
Figure 4.3: Powder X-ray diffraction patterns of $NdFeP_{1-x}As_xO_{0.9}F_{0.1}$.

increasing x. This suggests that lattice constants a and c increase with x and P/As substitution in 1111 system is succeeded. A little impurities of RAs and ROF are detected, but they do not seriously affect magnetic and transport properties.

4.1.2   Synchrotron X-ray diffraction

Powder diffraction patterns measured at BL-8A in PF are analyzed by Rietveld method [48]. They are well fitted with the symmetry of $P4/nmm$ in the tetragonal lattice. The x dependences of lattice constants (a and c), pnictogen height from Fe-layer (h_{Pn}) and Pn-Fe-Pn bond angle (α) of RFeP$_{1-x}$As$_x$O$_{0.9}$F$_{0.1}$ (R = La, Pr, Nd) are plotted in Figure 4.4. Lattice parameters of x
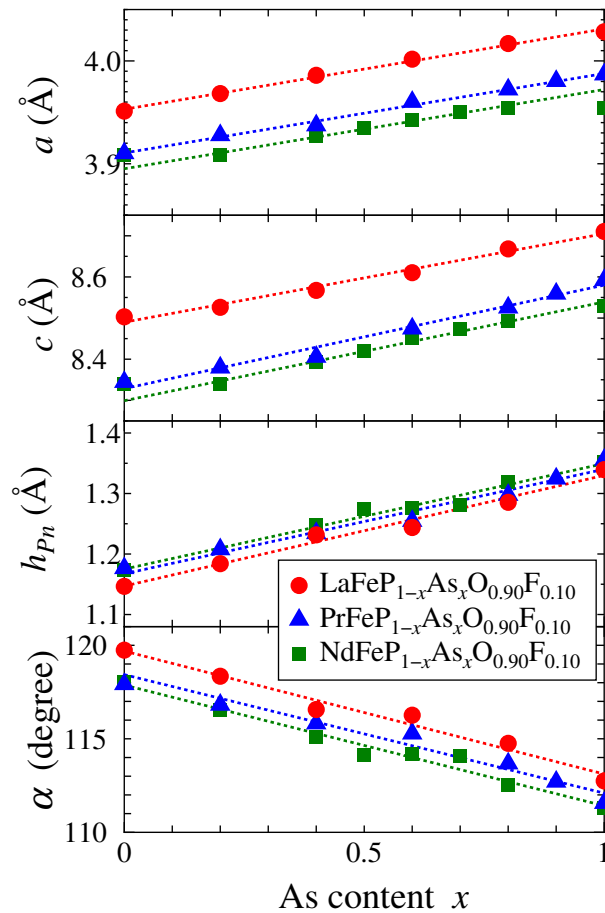
Figure 4.4: x dependence of a, c, h_{Pn} and α of RFeP$_{1-x}$As$_x$O$_{0.9}$F$_{0.1}$ (R = La, Pr, Nd).

= 0 and 1.0 are consistent with the previous studies [49] - [53]. a and c linearly increase with x, following Vegard's law. It proves that P/As substitution in RFeP$_{1-x}$As$_x$O$_{0.9}$F$_{0.1}$ is successfully prepared. h_{Pn} and α, which are the key parameters for iron-based superconductors, are also

linearly changed with x. The 10 % F substitution causes the disappearance of structural and magnetic transitions in 1111 system. Therefore, above crystal structural parameters do not change at low temperatures.

4.2   Magnetic susceptibility

Temperature dependences of magnetic susceptibility of $LaFeP_{1-x}As_xO_{0.9}F_{0.1}$, $PrFeP_{1-x}As_xO_{0.9}F_{0.1}$ and $NdFeP_{1-x}As_xO_{0.9}F_{0.1}$ are presented in Figures 4.5, 4.6 and 4.7. Sharp superconducting transition and bulk superconductivity are observed in most of the samples.

Figure 4.5: Temperature dependence of magnetic susceptibility of $LaFeP_{1-x}As_xO_{0.9}F_{0.1}$.

T_c of $x = 0$ and $x = 1.0$ are consistent with the previous studies [1, 2, 5, 54, 55]. The superconducting volume fraction is sufficiently large in most samples. T_c and the absolute value of χ are most enhanced at $x = 0.6$ in the case of $R = $ La. On the other hand, T_c gradually increases with x in Pr and Nd systems.

Figure 4.6: Temperature dependence of magnetic susceptibility of $\text{PrFeP}_{1-x}\text{As}_x\text{O}_{0.9}\text{F}_{0.1}$.

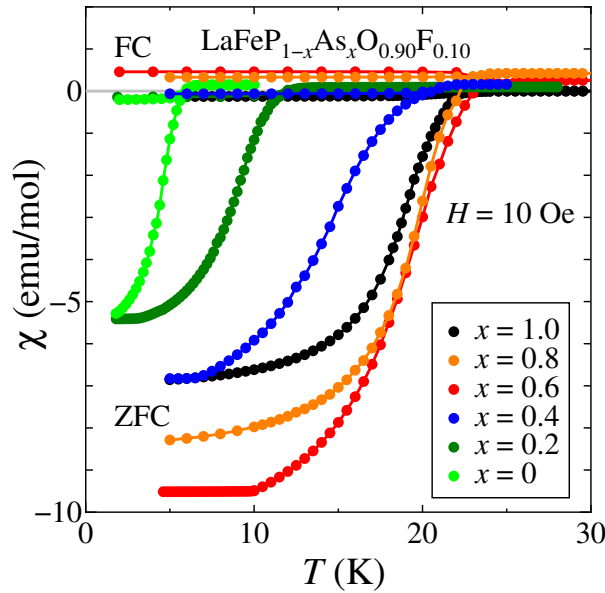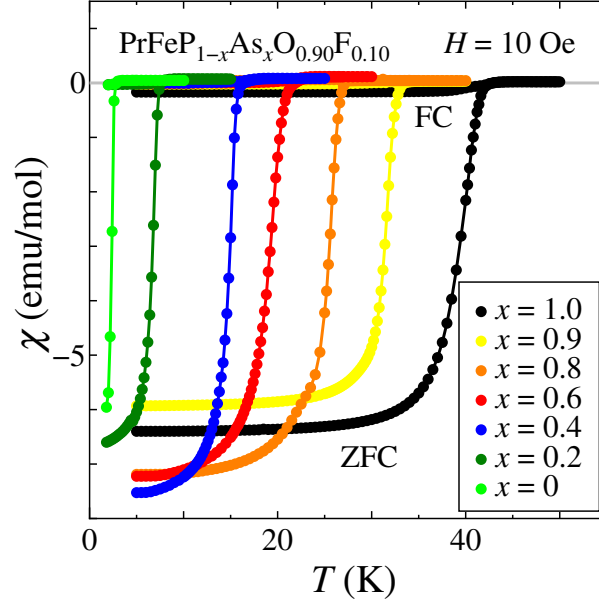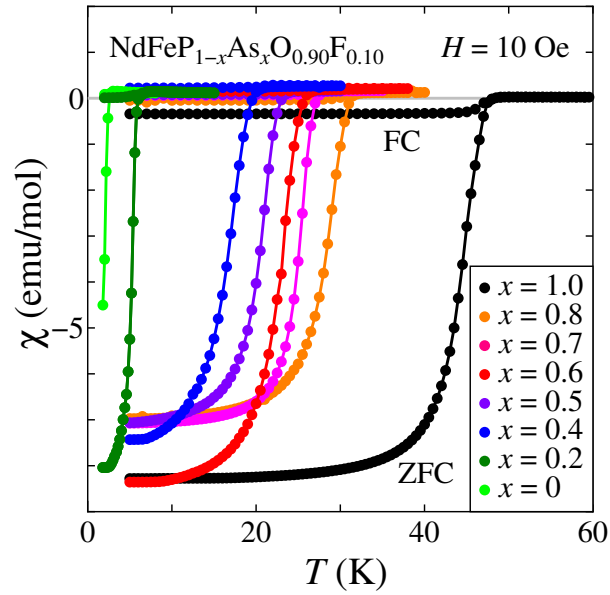

Figure 4.7: Temperature dependence of magnetic susceptibility of $\text{NdFeP}_{1-x}\text{As}_x\text{O}_{0.9}\text{F}_{0.1}$.

4.3   Electrical resistivity

Temperature dependences of electrical resistivity of $LaFeP_{1-x}As_xO_{0.9}F_{0.1}$, $PrFeP_{1-x}As_xO_{0.9}F_{0.1}$ and $NdFeP_{1-x}As_xO_{0.9}F_{0.1}$ are presented in Figures 4.8, 4.11 and 4.14. Absolute values of ρ of my polycrystalline samples are about ten times larger than that of single crystals in the previous works [56]. This is caused by a grain boundary effect. However, the temperature dependence profiles of ρ is not so different between polycrystalline and single-crystalline samples. Therefore, it is meaningful to discuss transport properties of polycrystalline samples. The anisotropic factor Γ of a metal is described as

$$\Gamma = \frac{H_{c2}^{ab}}{H_{c2}^{c}} = \left(\frac{m_c^*}{m_{ab}^*}\right)^{\frac{1}{2}} = \left(\frac{\rho_c}{\rho_{ab}}\right)^{\frac{1}{2}} \tag{4.1}$$

where H_{c2}^{ab} (H_{c2}^{c}), m_{ab}^* (m_c^*), ρ_{ab} (ρ_c) are in-plane (out-of-plane) upper critical magnetic field, effective mass and electrical resistivity, respectively. ρ_c/ρ_{ab} is ~ 25 when Γ is ~ 5 as reported previously [56]. Therefore, it is expected that electrical current mainly flows in the in-plane direction and electrical resistivity of polycrystalline samples mainly reflects in-plane one in 1111 system.

In spite of different R, some common behaviors are observed as follows.

(ⅰ) No indication of structural and magnetic transitions is observed in all samples.

(ⅱ) At $x = 0$, ρ shows a conventional Fermi liquid behavior $\rho \sim T^2$ and the absolute value of ρ is the smallest.

(ⅲ) At $x \sim 0.6$, ρ shows T-linear behavior and the absolute value of ρ is the largest.

In order to analyze and discuss the above behaviors, I fit the resistivity $\rho(T)$ with the formula

$$\rho(T) = \rho_0 + AT^n \tag{4.2}$$

in the temperature range between T_c and 100 K, where ρ_0, A and n are the residual resistivity, the slope and the power law exponent of T, respectively. The present fitting range is defined to subtract the scattering effect by phonon at high temperatures and focus on the essential behaviors of strongly correlated electron system at low temperatures. I note that $\rho(T)$ is exponent at $T < 100$ K because $\log(\rho - \rho_0)$ is always linear to $\log T$ at $T < 100$ K. Double logarithmic plots of electrical resistivity of $LaFeP_{1-x}As_xO_{0.9}F_{0.1}$, $PrFeP_{1-x}As_xO_{0.9}F_{0.1}$ and

NdFeP$_{1-x}$As$_x$O$_{0.9}$F$_{0.1}$ are presented in Figures 4.9, 4.12 and 4.15. Fitting curves of electrical resistivity of LaFeP$_{1-x}$As$_x$O$_{0.9}$F$_{0.1}$, PrFeP$_{1-x}$As$_x$O$_{0.9}$F$_{0.1}$ and NdFeP$_{1-x}$As$_x$O$_{0.9}$F$_{0.1}$ are presented in Figures 4.10, 4.13 and 4.16. Details of fitting parameters are discussed in Chapter 5.
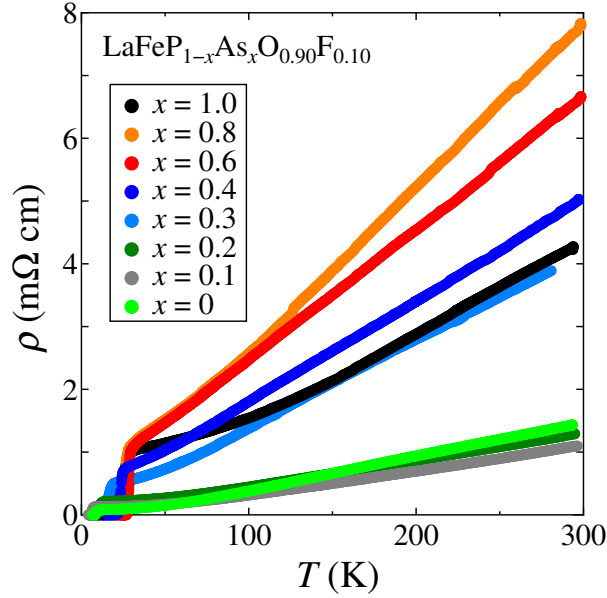
Figure 4.8: Temperature dependence of electrical resistivity of LaFeP$_{1-x}$As$_x$O$_{0.9}$F$_{0.1}$.
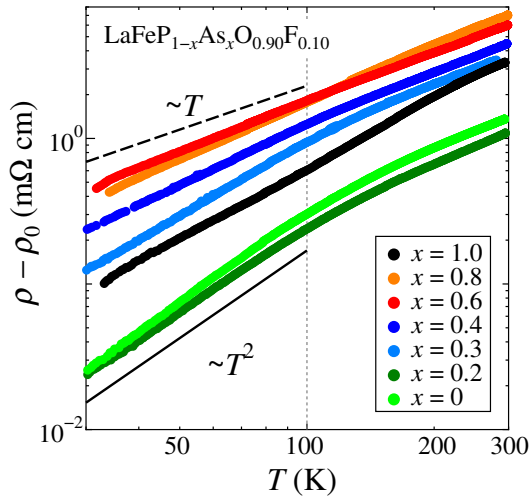
Figure 4.9: Double logarithmic plot of electrical resistivity of LaFeP$_{1-x}$As$_x$O$_{0.9}$F$_{0.1}$.
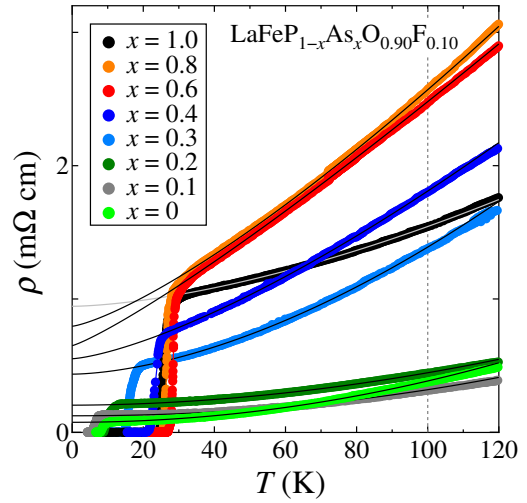
Figure 4.10: Experimental results (dots) and fitting curves (solid line) of electrical resistivity of LaFeP$_{1-x}$As$_x$O$_{0.9}$F$_{0.1}$.
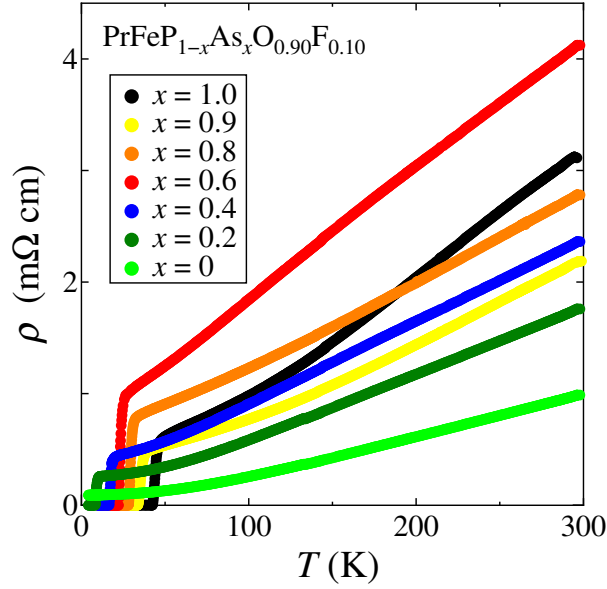
Figure 4.11: Temperature dependence of electrical resistivity of $PrFeP_{1-x}As_xO_{0.9}F_{0.1}$.
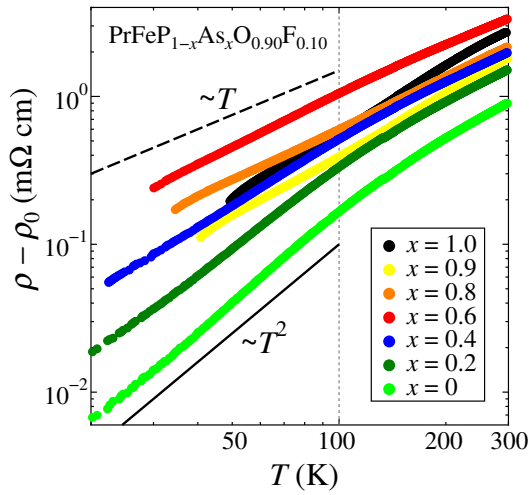
Figure 4.12: Double logarithmic plot of electrical resistivity of $PrFeP_{1-x}As_xO_{0.9}F_{0.1}$.
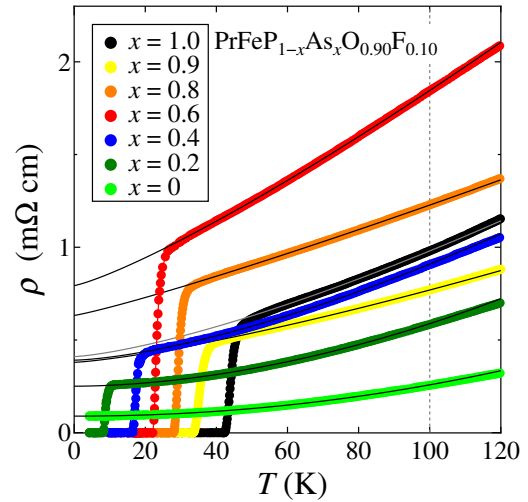
Figure 4.13: Experimental results (dots) and fitting curves (solid line) of electrical resistivity of $PrFeP_{1-x}As_xO_{0.9}F_{0.1}$.
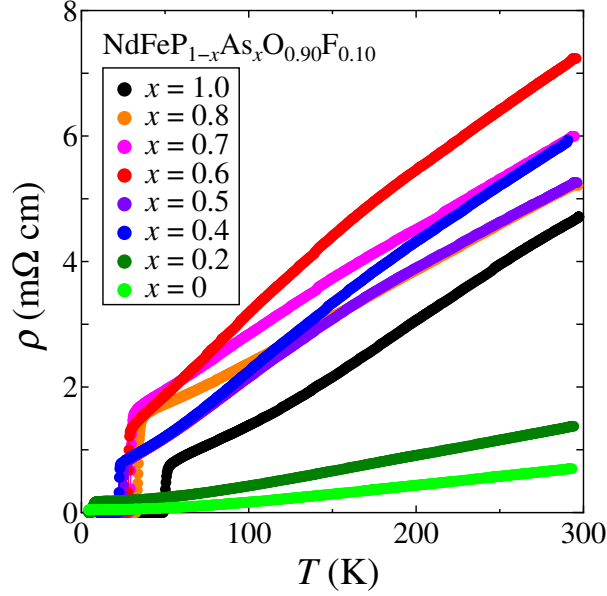
Figure 4.14: Temperature dependence of electrical resistivity of $NdFeP_{1-x}As_xO_{0.9}F_{0.1}$.
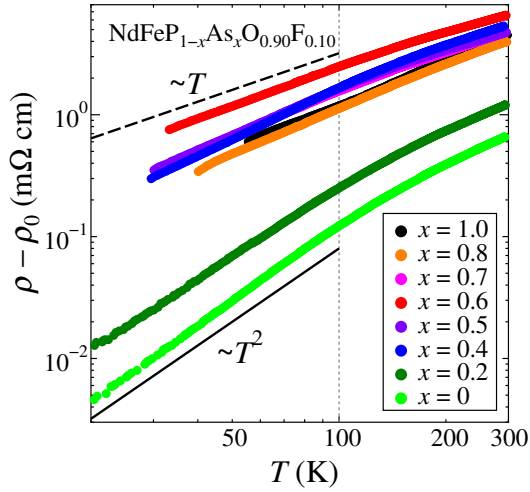
Figure 4.15: Double logarithmic plot of electrical resistivity of $NdFeP_{1-x}As_xO_{0.9}F_{0.1}$.
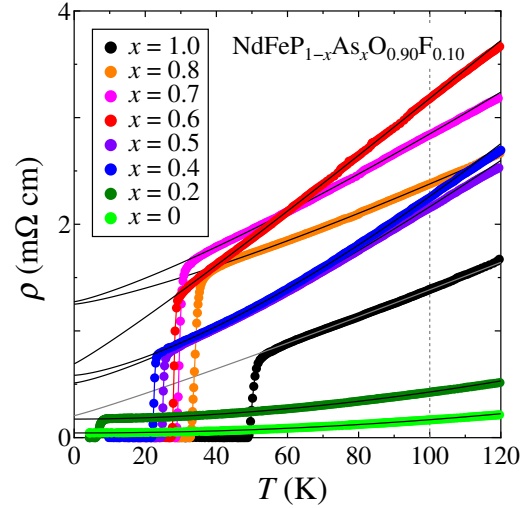
Figure 4.16: Experimental results (dots) and fitting curves (solid line) of electrical resistivity of $NdFeP_{1-x}As_xO_{0.9}F_{0.1}$.

4.4   Hall effect

4.4.1   Hall resistivity

LaFeP$_{1-x}$As$_x$O$_{0.9}$F$_{0.1}$

Magnetic field dependences of Hall resistivity ρ_{xy} in LaFeP$_{1-x}$As$_x$O$_{0.9}$F$_{0.1}$ with various x are shown in Figures 4.17 - 4.22. In multi-carrier system having hole and electron as carriers, $\rho_{xy}(H)$ shows magnetic field dependence and it is described as

$$\rho_{xy}(H) = \frac{1}{|e|} \frac{n_h\mu_h^2 - n_e\mu_e^2 + (\mu_h\mu_e)^2(n_h - n_e)H^2}{(n_h\mu_h + n_e\mu_e)^2 + (\mu_h\mu_e)^2(n_h - n_e)^2H^2} H \qquad (4.3)$$

where n_h (n_e) and μ_h (μ_e) are hole (electron) carrier density and mobility [57]. This system is regarded as a nearly compensated metal because the F concentration is only 10 %. When $n_h \approx n_e$ is assumed, $(n_h\mu_h + n_e\mu_e)^2 >> (\mu_h\mu_e)^2(n_h - n_e)^2H^2$ holds. Then $\rho_{xy}(H)$ is fitted with the formula $\rho_{xy}(H) = c_1H + c_2H^3$ and c_1 is defined as R_{H}. Dots and lines in Figs 4.17 - 4.37 indicate the experimental results and the fitting curves of $\rho_{xy}(H) = c_1H + c_2H^3$, respectively. When superconductivity is broken by high magnetic fields, ρ_{xy} cannot be fitted with the above formula. So below T_{c}, ρ_{xy} is fitted with $\rho_{xy}(H) = c_1H$ only in the low magnetic field in order to describe the superconducting state in $H \to 0$.

Figure 4.17: Magnetic field dependence of Hall resistivity ρ_{xy} of LaFePO$_{0.9}$F$_{0.1}$.
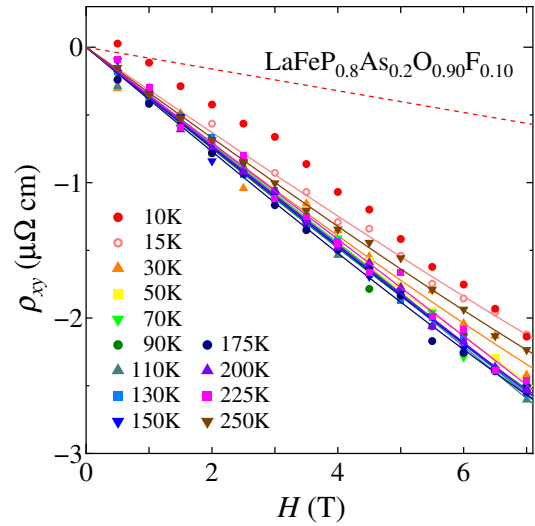
Figure 4.18: Magnetic field dependence of Hall resistivity ρ_{xy} of LaFeP$_{0.8}$As$_{0.2}$O$_{0.9}$F$_{0.1}$.

Figure 4.19: Magnetic field dependence of Hall resistivity ρ_{xy} of LaFeP$_{0.6}$As$_{0.4}$O$_{0.9}$F$_{0.1}$.

Figure 4.20: Magnetic field dependence of Hall resistivity ρ_{xy} of LaFeP$_{0.4}$As$_{0.6}$O$_{0.9}$F$_{0.1}$.

Figure 4.21: Magnetic field dependence of Hall resistivity ρ_{xy} of LaFeP$_{0.2}$As$_{0.8}$O$_{0.9}$F$_{0.1}$.
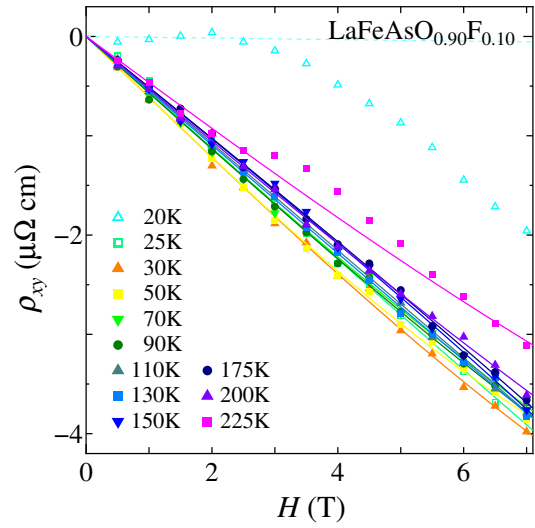
Figure 4.22: Magnetic field dependence of Hall resistivity ρ_{xy} of LaFeAsO$_{0.9}$F$_{0.1}$.

PrFeP$_{1-x}$As$_x$O$_{0.9}$F$_{0.1}$

Magnetic field dependences of Hall resistivity ρ_{xy} in PrFeP$_{1-x}$As$_x$O$_{0.9}$F$_{0.1}$ with various x are shown in Figures 4.23 - 4.29.
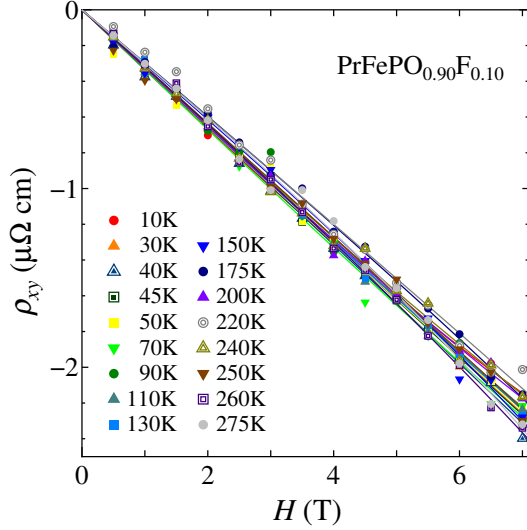
Figure 4.23: Magnetic field dependence of Hall resistivity ρ_{xy} of PrFePO$_{0.9}$F$_{0.1}$.
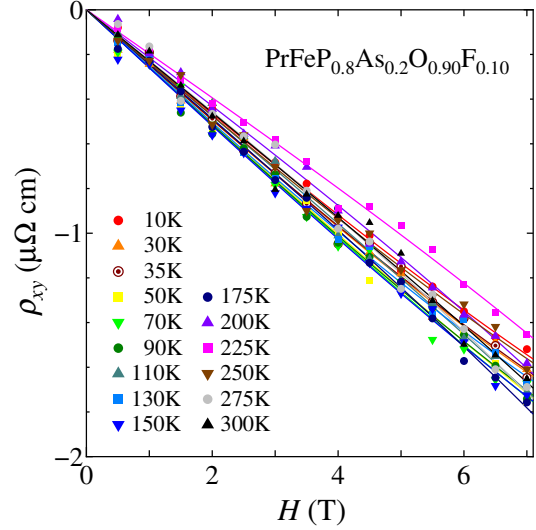
Figure 4.24: Magnetic field dependence of Hall resistivity ρ_{xy} of PrFeP$_{0.8}$As$_{0.2}$O$_{0.9}$F$_{0.1}$.
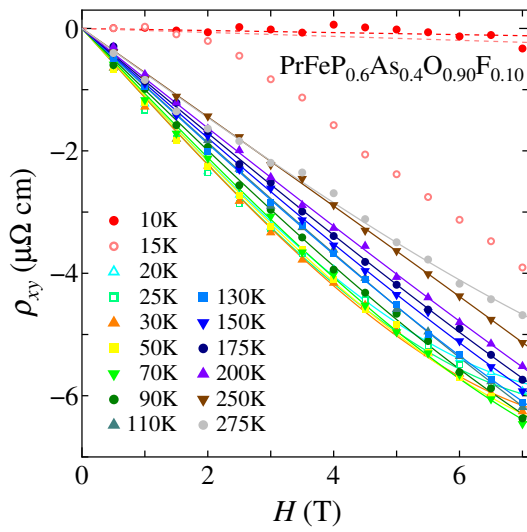
Figure 4.25: Magnetic field dependence of Hall resistivity ρ_{xy} of PrFeP$_{0.6}$As$_{0.4}$O$_{0.9}$F$_{0.1}$.
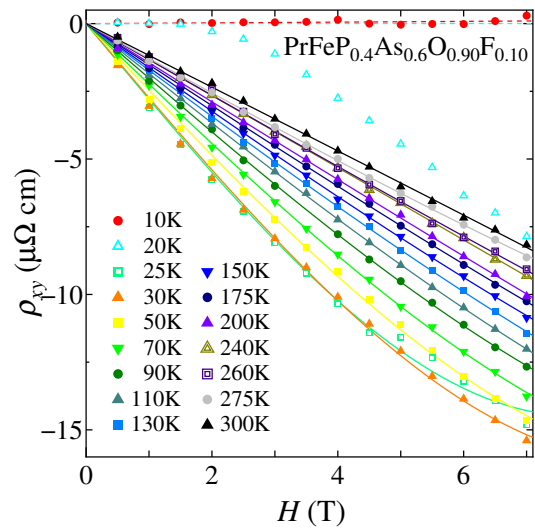
Figure 4.26: Magnetic field dependence of Hall resistivity ρ_{xy} of PrFeP$_{0.4}$As$_{0.6}$O$_{0.9}$F$_{0.1}$.
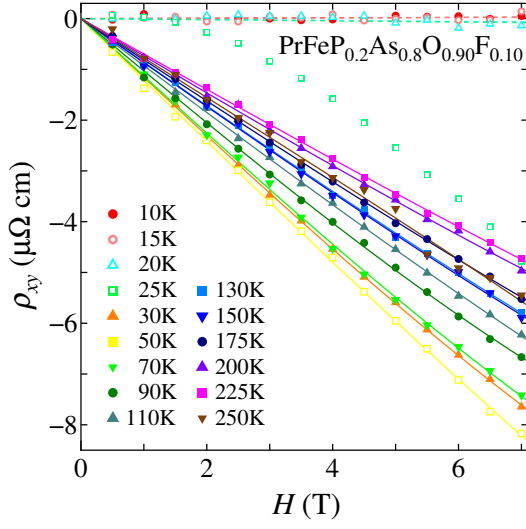
Figure 4.27: Magnetic field dependence of Hall resistivity ρ_{xy} of $PrFeP_{0.2}As_{0.8}O_{0.9}F_{0.1}$.
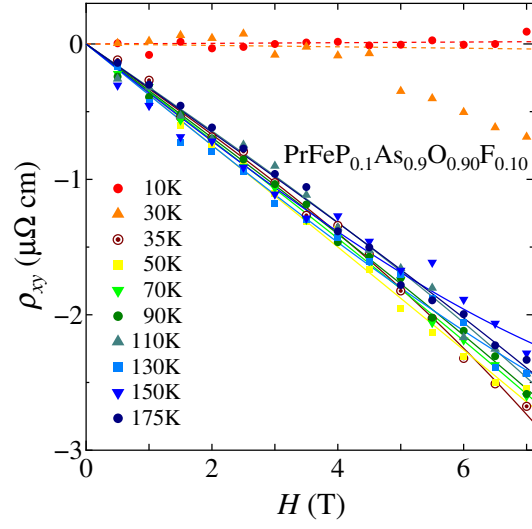
Figure 4.28: Magnetic field dependence of Hall resistivity ρ_{xy} of $PrFeP_{0.1}As_{0.9}O_{0.9}F_{0.1}$.
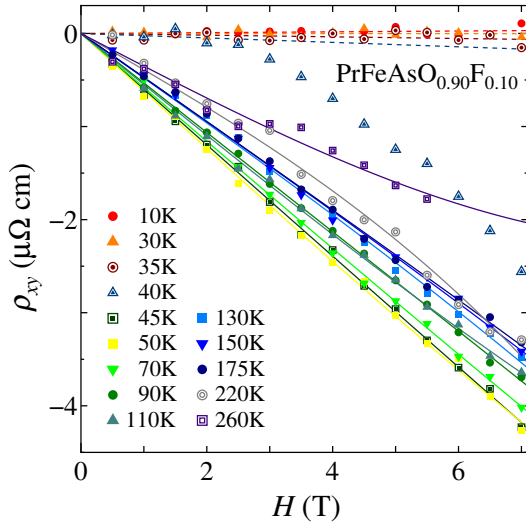
Figure 4.29: Magnetic field dependence of Hall resistivity ρ_{xy} of $PrFeAsO_{0.9}F_{0.1}$.

NdFeP$_{1-x}$As$_x$O$_{0.9}$F$_{0.1}$

Magnetic field dependences of Hall resistivity ρ_{xy} in NdFeP$_{1-x}$As$_x$O$_{0.9}$F$_{0.1}$ with various x are shown in Figures 4.30 - 4.37.
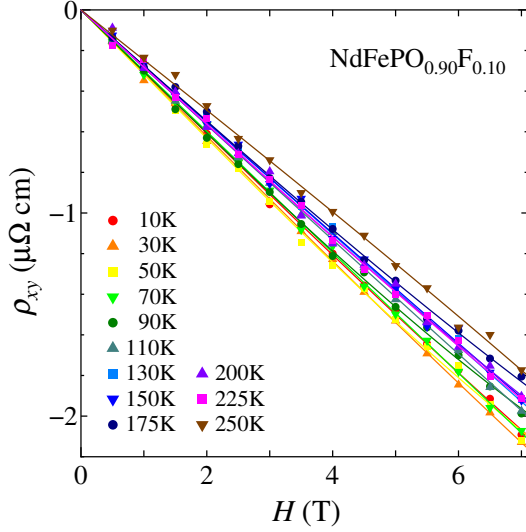
Figure 4.30: Magnetic field dependence of Hall resistivity ρ_{xy} of NdFePO$_{0.9}$F$_{0.1}$.
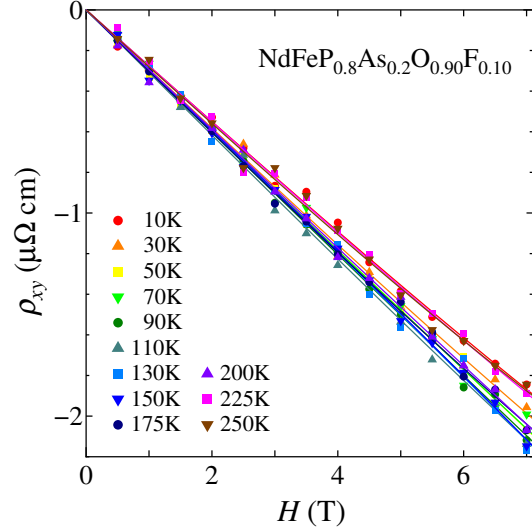
Figure 4.31: Magnetic field dependence of Hall resistivity ρ_{xy} of NdFeP$_{0.8}$As$_{0.2}$O$_{0.9}$F$_{0.1}$.
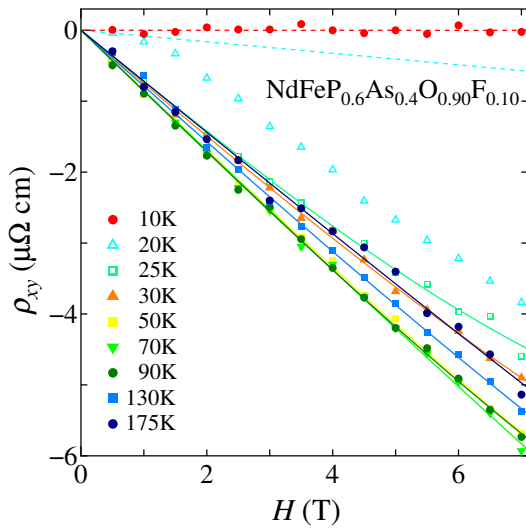
Figure 4.32: Magnetic field dependence of Hall resistivity ρ_{xy} of NdFeP$_{0.6}$As$_{0.4}$O$_{0.9}$F$_{0.1}$.
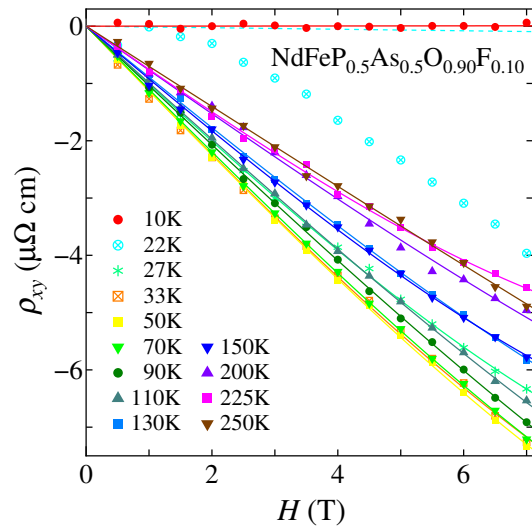
Figure 4.33: Magnetic field dependence of Hall resistivity ρ_{xy} of NdFeP$_{0.5}$As$_{0.5}$O$_{0.9}$F$_{0.1}$.
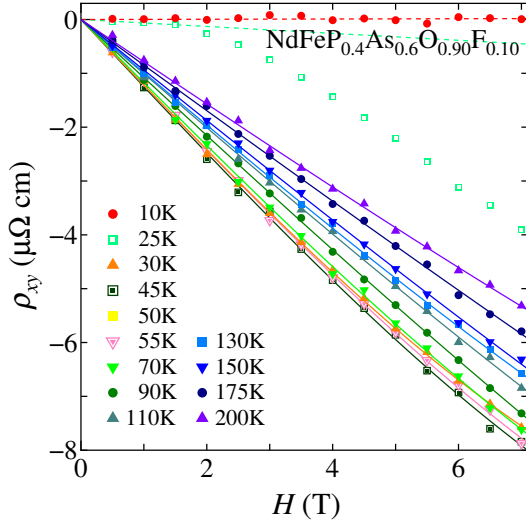
Figure 4.34: Magnetic field dependence of Hall resistivity ρ_{xy} of NdFeP$_{0.4}$As$_{0.6}$O$_{0.9}$F$_{0.1}$.
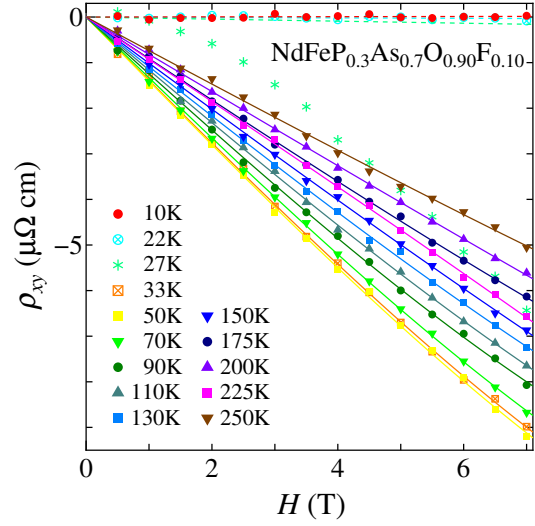
Figure 4.35: Magnetic field dependence of Hall resistivity ρ_{xy} of NdFeP$_{0.3}$As$_{0.7}$O$_{0.9}$F$_{0.1}$.
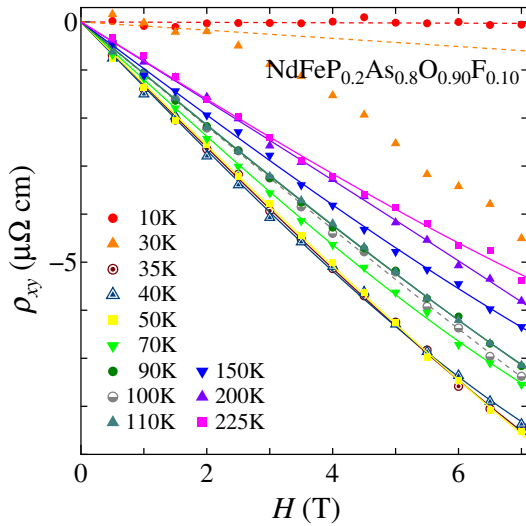
Figure 4.36: Magnetic field dependence of Hall resistivity ρ_{xy} of NdFeP$_{0.2}$As$_{0.8}$O$_{0.9}$F$_{0.1}$.
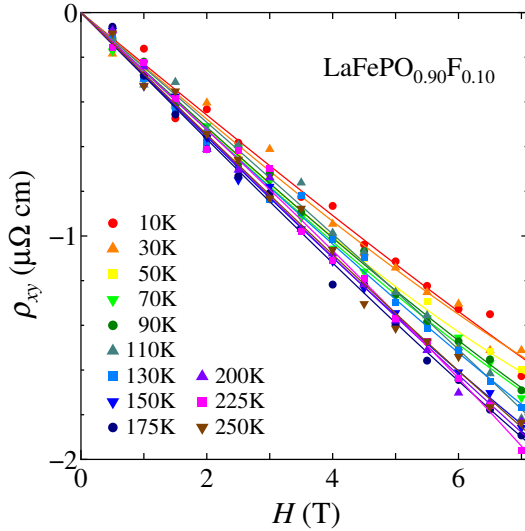

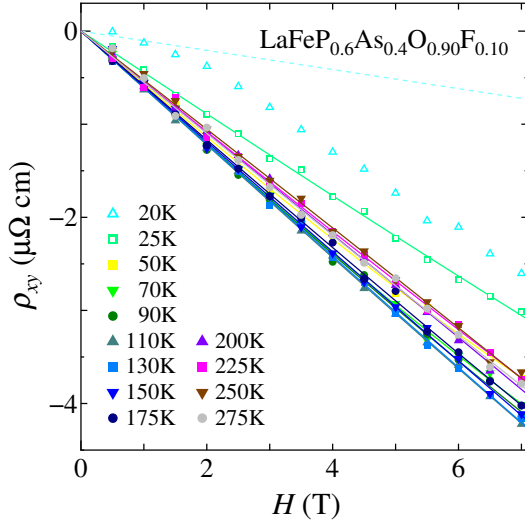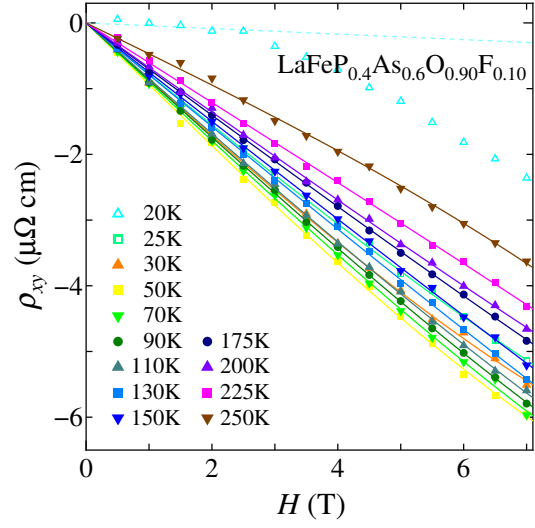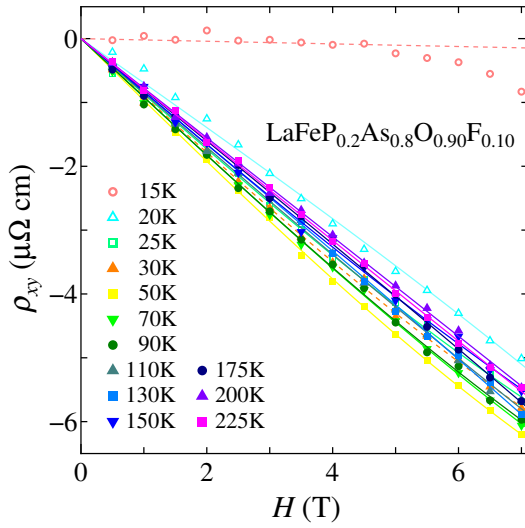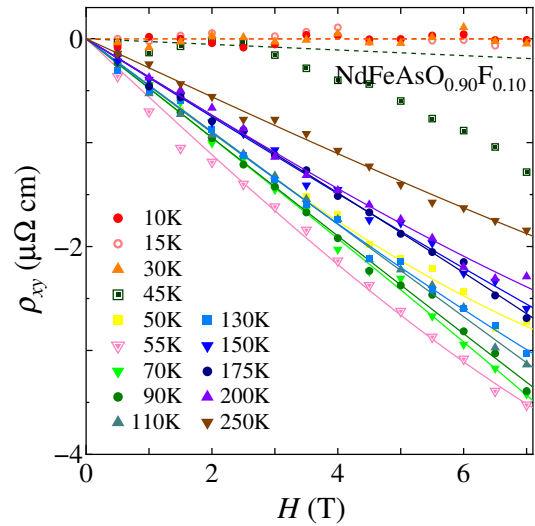Figure 4.37: Magnetic field dependence of Hall resistivity ρ_{xy} of NdFeAsO$_{0.9}$F$_{0.1}$.

4.4.2   Hall coefficient

Temperature dependences of Hall coefficient R_H of $LaFeP_{1-x}As_xO_{0.9}F_{0.1}$, $PrFeP_{1-x}As_xO_{0.9}F_{0.1}$ and $NdFeP_{1-x}As_xO_{0.9}F_{0.1}$ are presented in Figures 4.38, 4.39 and 4.40.   The value of R_H in
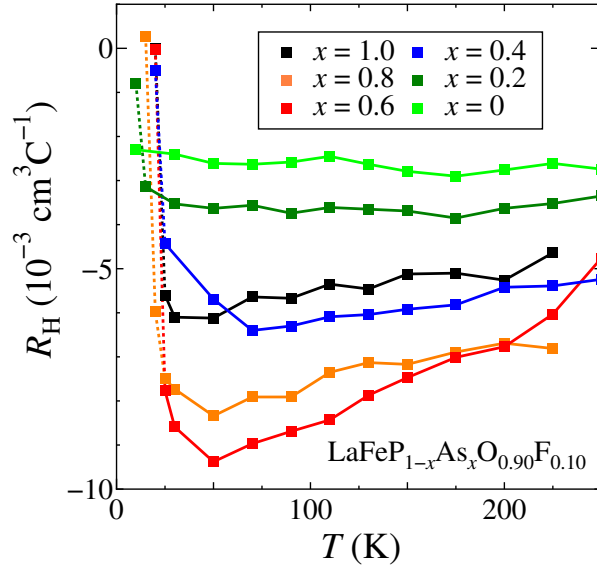
Figure 4.38: Temperature dependence of Hall coefficient of $LaFeP_{1-x}As_xO_{0.9}F_{0.1}$.

the normal state is negative for all compositions, and the dominant carriers are electrons in this system . At $x = 0$, the absolute value of R_H ($|R_H|$) is small ($\sim$ -3 $\times$ 10^{-3} cm^3/C) and almost temperature-independent for all R systems. On the other hand, $|R_H|$ is large and strongly temperature dependent at $x \sim 0.6$. At $x = 1.0$, $|R_H|$ is smaller and shows weaker temperature dependence than that of $x \sim 0.6$. The results suggest the change of the electronic structure around $x \sim 0.6$. The details are discussed in the next chapter.
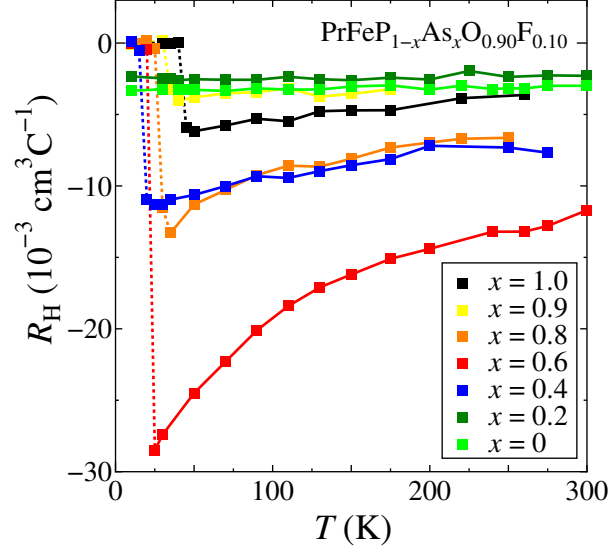
Figure 4.39: Temperature dependence of Hall coefficient of $PrFeP_{1-x}As_xO_{0.9}F_{0.1}$.
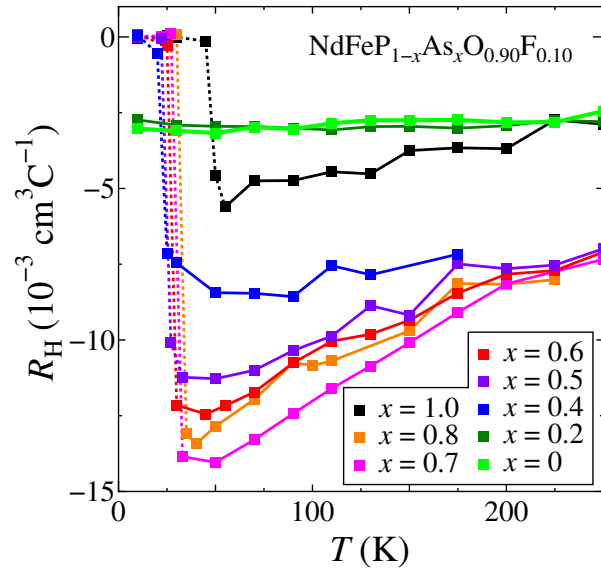
Figure 4.40: Temperature dependence of Hall coefficient of $NdFeP_{1-x}As_xO_{0.9}F_{0.1}$.

Chapter 5

Discussion

5.1 Crystal structural parameters and T_c

5.1.1 Bond angle α dependence of T_c

Pn-Fe-Pn bond angle α dependence of T_c in $R\mathrm{FeP}_{1-x}\mathrm{As}_x\mathrm{O}_{0.9}\mathrm{F}_{0.1}$ (R = La, Pr, Nd) is plotted in Figure 5.1. The reported results of $R\mathrm{FeAsO}_{1-y}$ are also plotted together. My results of α and
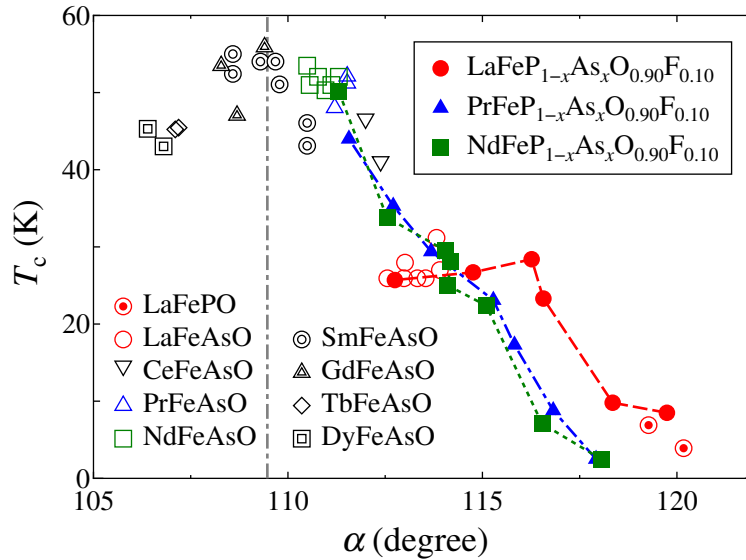
Figure 5.1: Pn-Fe-Pn bond angle α dependence of T_c in $R\mathrm{FeP}_{1-x}\mathrm{As}_x\mathrm{O}_{0.9}\mathrm{F}_{0.1}$ (R = La, Pr, Nd) (solid symbols). The reported results of $R\mathrm{FePO}$ and $R\mathrm{FeAsO}_{1-y}$ are also plotted (open symbols) [28].

T_c at $x = 0$ and 1.0 are consistent with those in the previous studies. T_c gradually increases to 44 K and 50 K with decreasing α in Pr and Nd systems. On the other hand, T_c increases from

$\alpha = 120$ ° to 116 ° and keeps 26 - 28 K from 116 ° to 113 ° in La system. Additionally, T_c of La system is much higher than that of Pr and Nd systems at the same α, where $\alpha = 115$ - 120 °. Therefore, variations of T_c cannot be ascribed to only those of α.

5.1.2   Pnictogen height h_{Pn} dependence of T_c

Pnictogen height from Fe-layer h_{Pn} versus T_c in $R\text{FeP}_{1-x}\text{As}_x\text{O}_{0.9}\text{F}_{0.1}$ (R = La, Pr, Nd) is plotted in Figure 5.2. The reported results of other iron pnictide superconductors are also plotted together. h_{Pn} and T_c at $x = 0$ and 1.0 are consistent with the previous studies. T_c
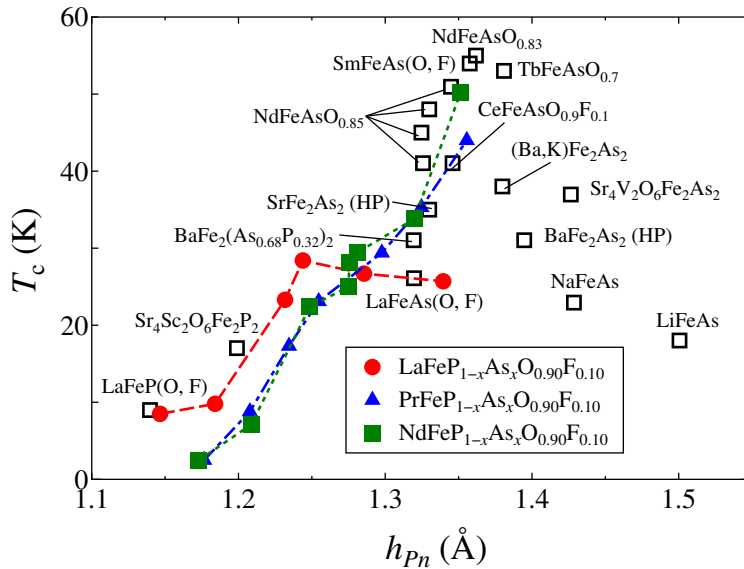
Figure 5.2: Pnictogen height from Fe-layer h_{Pn} dependence of T_c in $R\text{FeP}_{1-x}\text{As}_x\text{O}_{0.9}\text{F}_{0.1}$ (R = La, Pr, Nd) (solid symbols). The reported results of other iron pnictide superconductors are also plotted (black open squares) [29].

gradually increases with h_{Pn} in Pr and Nd systems. On the other hand, T_c increases from h_{Pn} = 1.15 Å to 1.24 Å and does not change much from 1.24 Å to 1.35 Å in La system. As a result, variations of T_c cannot be ascribed to only those of h_{Pn}.

5.2   Transport properties

5.2.1 x dependences of T_c and n

Temperature dependence of electrical resistivity is fitted with the formula $\rho(T) = \rho_0 + AT^n$. x dependences of T_c and n of $R\text{FeP}_{1-x}\text{As}_x\text{O}_{0.9}\text{F}_{0.1}$ (R = La, Pr, Nd) are presented in Figure

5.3. In almost all samples, the superconducting transitions are sharp enough to determine T_c from the middle temperature of the resistive transition. In $PrFePO_{0.9}F_{0.1}$ and $NdFePO_{0.9}F_{0.1}$, $T_c < 4.2$ K is defined as an onset temperature in magnetic susceptibility.
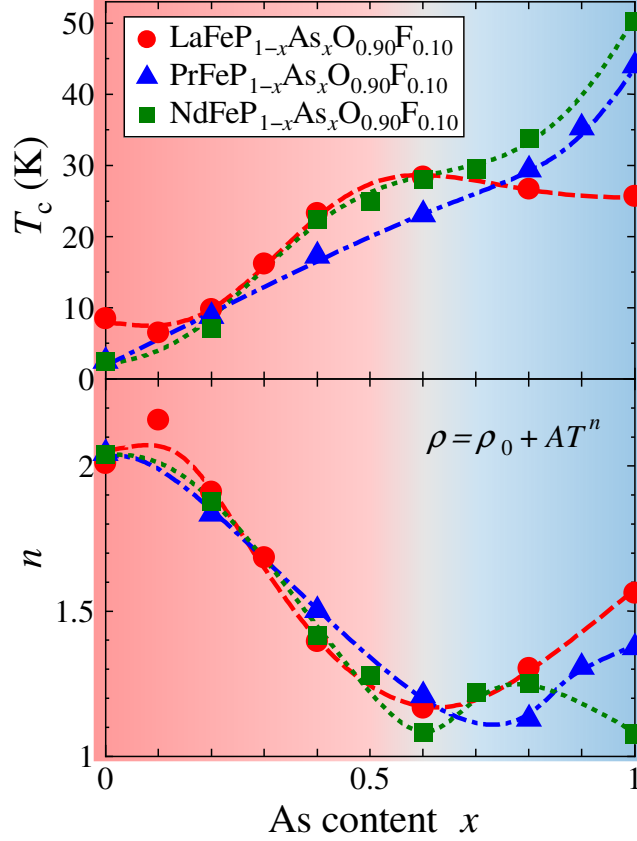
Figure 5.3: x dependences of T_c and n in $RFeP_{1-x}As_xO_{0.9}F_{0.1}$ (R = La, Pr, Nd). Two different composition regions of $x < 0.6$ - 0.8 (red) and $x > 0.6$ - 0.8 (blue) are also illustrated.

T_c and n change non-linearly with x while crystal structural parameters change linearly with x, as shown in Figure 4.4. This suggests the existences of other hidden parameters beyond the crystal structural parameters. When x dependences of T_c and n are simultaneously focused on, two different composition regions of $x < 0.6$ - 0.8 (red area in Figure 5.3) and $x > 0.6$ - 0.8 (blue area) are extracted.

In the region of $x < 0.6$ - 0.8, both of T_c and n show nearly the same behaviors in all R systems. They are affected by neither α nor h_{Pn} that are significantly different between La and the other systems. T_c increases from ~ 3 K to ~ 30 K with x in the region of $x < 0.6$ - 0.8. n is ~ 2 at $x = 0$, namely $\rho \sim T^2$. This behavior can be explained as a conventional Fermi liquid behavior. n decreases from ~ 2 to ~ 1 with increasing x and then ρ shows T-linear behavior

at low temperatures around $x = 0.6$. In 2-dimensional AFM compounds, ρ decreases linearly with T in the vicinity of QCP [58]. As for QCP, it is confirmed with T-linear resistivity at x = 0.3 in P/As substituted $BaFe_2(As_1-xP_x)_2$. As for AFM fluctuation, NMR measurements using my polycrystalline samples of $LaFeP_{1-x}As_xO_{0.9}F_{0.1}$ (x = 0, 0.2, 0.6) are performed by Mukuda *et al.* [59]. Their results of $1/T_1T$ are shown in Figure 5.4. The peak of $1/T_1T$ at
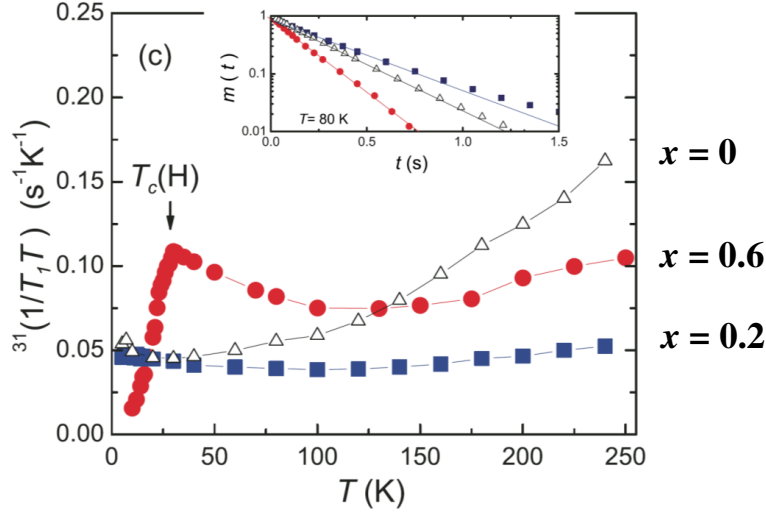
Figure 5.4: Temperature dependence of $1/T_1T$ [59]

$x = 0.6$ suggests the enhancement of the AFM fluctuation. As a result, the T-linear behavior of electrical resistivity in the present systems indicates the enhancement of AFM fluctuation around x = 0.6 - 0.8. These experimental facts that T_c and AFM fluctuation increase and AFM fluctuation is enhanced with x mean that AFM fluctuation enhanced T_c to about 30 K in this composition region. This conclusion is consistent with many theoretical and experimental studies on iron-based superconductors.

In the region of $x > 0.6$ - 0.8, T_c is affected not only by x but also R. x dependence of T_c shows different behaviors among different R systems. In the case of R = La, T_c does not change significantly with x. In the case of R = Pr and Nd, T_c increase with x. No clear correlation between T_c and n is observed except for $x = 1.0$. At $x = 1.0$, T_c increases and n decreases with the decreasing ionic radius of R (La $\rightarrow$ Pr $\rightarrow$ Nd). The similar behaviors of T_c and n were observed in $RFeAsO_{1-y}$ system, and the details is discussed later.

5.2.2 x dependences of ρ_0 and A

x dependence of ρ_0 and A in $R\mathrm{FeP}_{1-x}\mathrm{As}_x\mathrm{O}_{0.9}\mathrm{F}_{0.1}$ (R = La, Pr, Nd) is presented in Figure 5.5. It is impossible to obtain accurate absolute values of ρ_0 and A because the sintered density of
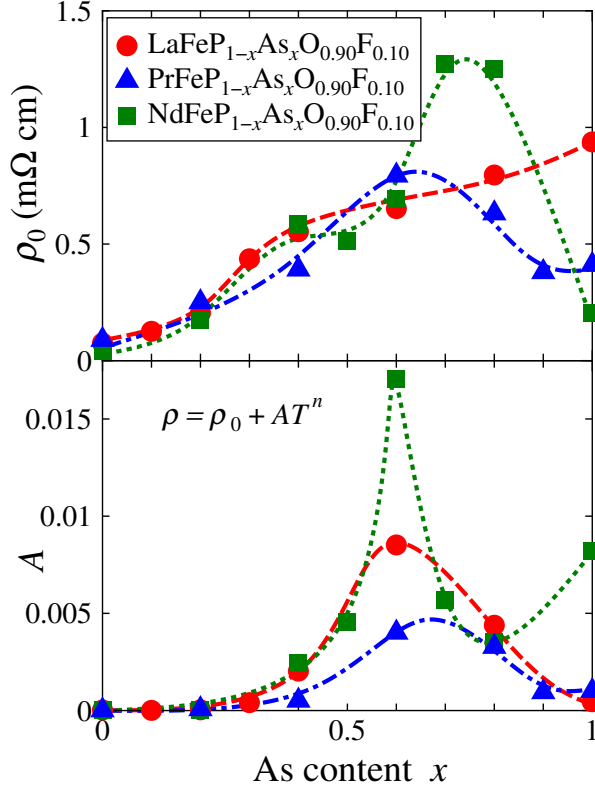
Figure 5.5: x dependence of ρ_0 and A in $R\mathrm{FeP}_{1-x}\mathrm{As}_x\mathrm{O}_{0.9}\mathrm{F}_{0.1}$ (R = La, Pr, Nd).

polycrystalline samples is not constant. However, rough tendencies that ρ_0 and A are enhanced at $x \sim 0.6$ - 0.8 are observed in all R systems.

5.2.3 x dependence of R_H at $T = 50$ K

To clarify the x dependence of Hall coefficient at low temperatures, x dependences of R_H at $T = 50$ K and n in $R\mathrm{FeP}_{1-x}\mathrm{As}_x\mathrm{O}_{0.9}\mathrm{F}_{0.1}$ (R = La, Pr, Nd) are presented in Figure 5.6. Both of P and As have the valence of -3 in the present systems. Therefore, P/As substitution should not change the carrier density of $R\mathrm{FeP}_{1-x}\mathrm{As}_x\mathrm{O}_{0.9}\mathrm{F}_{0.1}$. However, $|R_\mathrm{H}|$ is enhanced and shows strong temperature dependence at $x \sim 0.6$ - 0.8, where n approaches 1. They seems to be ascribed to (i) band crossing on E_F and/or (ii) inherent behaviors of strongly correlated electron system.
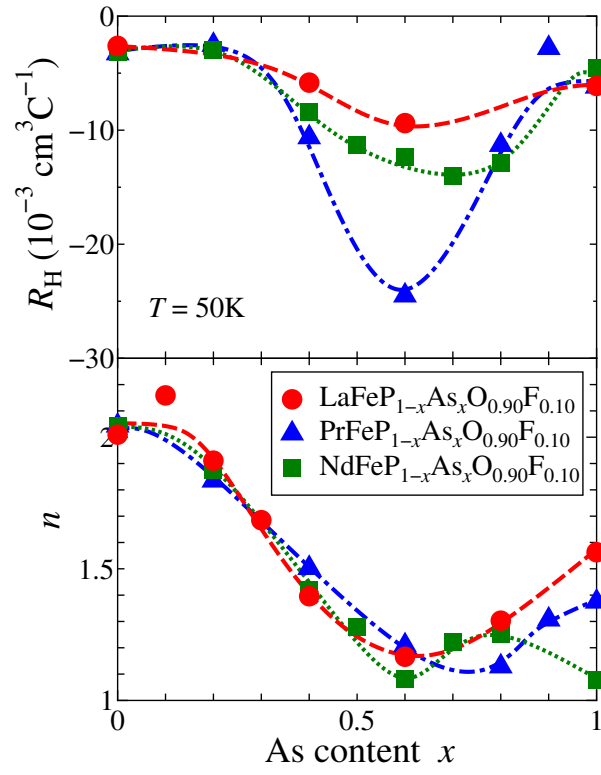
Figure 5.6: x dependence of R_H at $T = 50$ K and n in $R\text{FeP}_{1-x}\text{As}_x\text{O}_{0.9}\text{F}_{0.1}$ ($R =$ La, Pr, Nd).

As for the case (i), R_{H} of normal single-band metal is described as

$$
R_{\mathrm{H}} = \begin{cases} \frac{1}{n_h e} & \text{(hole)} \\[2ex] -\frac{1}{n_e e} & \text{(eletron)} \end{cases} \tag{5.1}
$$

On the other hand, iron pnictides have both hole and electron carriers (multiband). Then R_{H} of a multiband metal is described as

$$
R_{\mathrm{H}} = \frac{1}{e} \frac{n_h \mu_h^2 - n_e \mu_e^2}{(n_h \mu_h + n_e \mu_e)^2} \tag{5.2}
$$

where n_h (n_e) and μ_h (μ_e) are hole (electron) carrier density and mobility, respectively. Theoretical calculations of band dispersions and FSs of NdFeAsO and LaFePO are shown in Figure 5.7. The theoretical study has demonstrated that the 3-dimensional hole FS with d_{Z^2} orbital
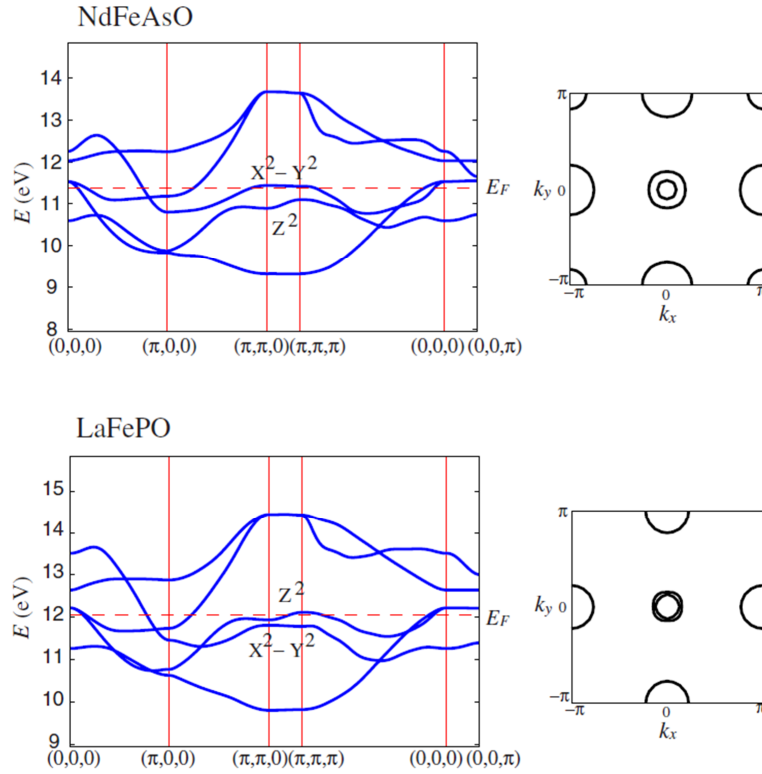
Figure 5.7: Theoretical calculation of band dispersions and FSs of NdFeAsO and LaFePO [27]

character exists around (π, π, π) in LaFePO, while the 2-dimensional hole FS with $d_{X^2-Y^2}$ orbital character exists around $(\pi, \pi, 0)$ in NdFeAsO. Both of the bands of d_{Z^2} and $d_{X^2-Y^2}$ may sink below E_{F} at $x \sim 0.6$ - 0.8. In that case, a decrease of n_h and the enhancement of $|R_{\mathrm{H}}|$ are

expected.

As for the case (ii), similar behaviors are also observed in $CeTMIn_5$ (TM = Co, Rh, Ir) in heavy fermion system [60]. Not only the enhancement of R_H but also T-linear resistivity and breaking the Kohler's law are suggested as characteristic behaviors of strongly correlated electron system.

If the scenario (ii) is adopted and the AFM fluctuation affects superconductivity in the region of $x > 0.6$ - 0.8, $|R_H|$ should show a different behavior for each R system having different T_c. Nevertheless, $|R_H|$ monotonically decreases with increasing x and reaches nearly the same value ($\sim$ -5 $\times$ 10^{-3} cm^{3}C^{-1}) at $x = 1.0$ in all R systems. Therefore, the scenario (i) is more likely than the scenario (ii).

5.2.4   Correlation between T_c and n

Correlation between T_c and n in RFeP$_{1-x}$As$_x$O$_{0.9}$F$_{0.1}$ (R = La, Pr, Nd)

In the region of $x < 0.6$ - 0.8, T_c increases from ~ 3 K to ~ 3 and n decreases from ~ 2 to ~ 1 with increasing x. In this region, the enhancement of AFM fluctuation causes the increase of T_c. For further understanding, n is plotted against T_c in Figure 5.8. In the region of $x <$
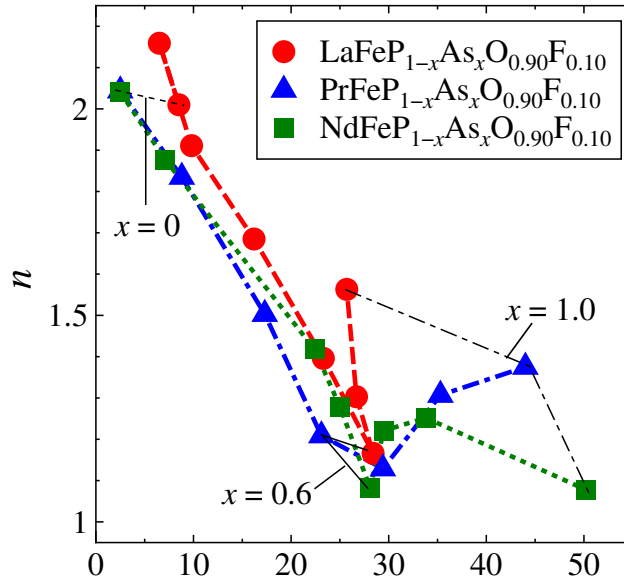
Figure 5.8: Correlation between T_c and n in RFeP$_{1-x}$As$_x$O$_{0.9}$F$_{0.1}$ (R = La, Pr, Nd).

0.6 - 0.8, T_c and n are on the same scaling line in spite of different R systems with different

lattice parameters. This scaling line demonstrates the correlation between the AFM fluctuation and T_c. T_c and n change with x on this line, therefore, As content x is an important parameter in this region. In the region of $x > 0.6$ - 0.8, however, the different behaviors of T_c and n are observed for different R systems.

Correlation between T_c and n in various iron pnictide superconductors

The other correlation between T_c and n is also reported by Ishida *et al.* [61]. They discuss the relationship between T_c and n in 1111-type RFeAsO$_{1-y}$ (R = La, Ce, Pr, Nd), 122-type Ba$_{1-x}$K$_x$Fe$_2$As$_2$, Ba(Fe$_{1-x}$Co$_x$)$_2$As$_2$ and BaFe$_2$(As$_{1-x}$P$_x$)$_2$. As shown in Figure 5.9, the new scaling line is found, where n decreases from ~ 2 to ~ 1 and T_c increases from ~ 20 K to ~ 50 K. T_c and n of BaFe$_2$(As$_{1-x}$P$_x$)$_2$ ($x = 0.3$ - 0.7), 111-type LiFeAs and LiFeP by Kasahara *et al.* are also plotted with them in Figure 5.9. My and Ishida's scaling lines are indicated by red and blue bands, respectively.
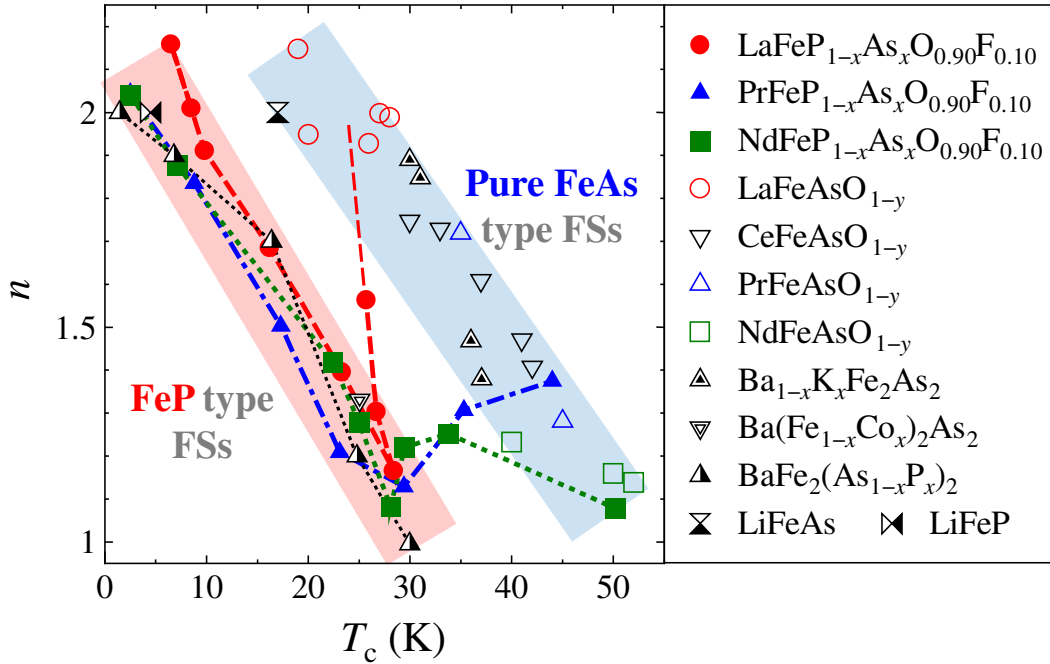
Figure 5.9: Correlation between T_c in RFeP$_{1-x}$As$_x$O$_{0.9}$F$_{0.1}$ (R = La, Pr, Nd) and various iron pnictide superconductors [16, 21, 56, 61].

My scaling line changes from $T_c \sim 0$ K / $n \sim 2$ to $T_c \sim 30$ K / $n \sim 1$. This scaling line contains not only the data for RFeP$_{1-x}$As$_x$O$_{0.9}$F$_{0.1}$ ($x = 0$ - 0.6) but also those for BaFe$_2$P$_2$ and LiFeP. As for RFeP$_{1-x}$As$_x$O$_{0.9}$F$_{0.1}$, the hole FS with $d_{X^2-Y^2}$ orbital character is expected to appear only

in the vicinity of $x = 1.0$ by band calculation. The hole FS generates different nesting vectors in spin fluctuation theory. Therefore, the correlation between T_c and n of $R\mathrm{FeP}_{1-x}\mathrm{As}_x\mathrm{O}_{0.9}\mathrm{F}_{0.1}$ (x < 0.6 - 0.8) may mean the enhancement of AFM fluctuation in the nesting situation without the $d_{X^2-Y^2}$ hole FS. 3-dimensionality of FSs, such as warping or decreasing of the contribution of the d_{xy} orbital character compared with iron arsenides, is also suggested in $\mathrm{BaFe}_2(\mathrm{As}_{1-x}\mathrm{P}_x)_2$ and LiFeP. As a result, my scaling line suggests the enhancement of AFM fluctuation in FeP-type FSs.

Ishida's scaling line in Figure 5.9 changes from $T_c \sim 20$ K / $n \sim 2$ to $T_c \sim 50$ K / $n \sim 1$. This scaling line is constructed of compounds having pure FeAs-type FSs, such as $R\mathrm{FeAsO}_{1-y}$ (R = La, Ce, Pr, Nd), $\mathrm{Ba}_{1-x}\mathrm{K}_x\mathrm{Fe}_2\mathrm{As}_2$ and LiFeAs. The present results of $\mathrm{PrFeAsO}_{0.9}\mathrm{F}_{0.1}$ and $\mathrm{NdFeAsO}_{0.9}\mathrm{F}_{0.1}$ are located on this second scaling line.

My scaling line indicates the enhancement of T_c with decreasing n in FeP-type FSs, while Ishida's line indicates a similar T_c behavior in pure FeAs-type FSs. The difference of T_c between the two scaling lines is ~ 20 K. This differrence of T_c may be caused by (i) the difference of FSs and nesting vectors or (ii) the difference between spin fluctuation and other new fluctuation.

Correlation among T_c, n and superconducting gap structure

Crystal structural parameters in iron-based superconductors affect not only T_c but also superconducting gap structure. Nodeless superconducting gap was reported in $R\mathrm{FeAsO}_{0.9}\mathrm{F}_{0.1}$, ($R$ = La, Pr, Nd), $R\mathrm{FeAsO}_{1-y}$ (R = La, Ce, Pr, Nd), $\mathrm{Ba}_{1-x}\mathrm{K}_x\mathrm{Fe}_2\mathrm{As}_2$, LiFeAs. On the other hand, nodal superconductivity was reported in $R\mathrm{FePO}_{0.9}\mathrm{F}_{0.1}$, ($R$ = La, Pr, Nd), $\mathrm{BaFe}_2(\mathrm{As}_{1-x}\mathrm{P}_x)_2$ and LiFeP. Correlation between T_c and n together with superconducting gap structure (Nodeless / Nodal) for various iron pnictide superconductors is presented in Figure 5.10.

The present results for x < 0.6 - 0.8 of $R\mathrm{FeP}_{1-x}\mathrm{As}_x\mathrm{O}_{0.9}\mathrm{F}_{0.1}$ are on the same scaling line with the results of LiFeP and $\mathrm{BaFe}_2(\mathrm{As}_{1-x}\mathrm{P}_x)_2$ having a nodal gap. $R\mathrm{FePO}_{0.9}\mathrm{F}_{0.1}$ is suggested to have a nodal gap on the electron FS with $s\pm$ wave symmetry or that on the hole FS with d wave symmetry. My experimental results of $x = 1.0$ of $R\mathrm{FeP}_{1-x}\mathrm{As}_x\mathrm{O}_{0.9}\mathrm{F}_{0.1}$ are on the same scaling line with $R\mathrm{FeAsO}_{1-y}$ (R = La, Ce, Pr, Nd) having a nodeless gap. $R\mathrm{FeAsO}_{0.9}\mathrm{F}_{0.1}$ is suggested to have a nodeless gap in $s\pm$ wave symmetry.
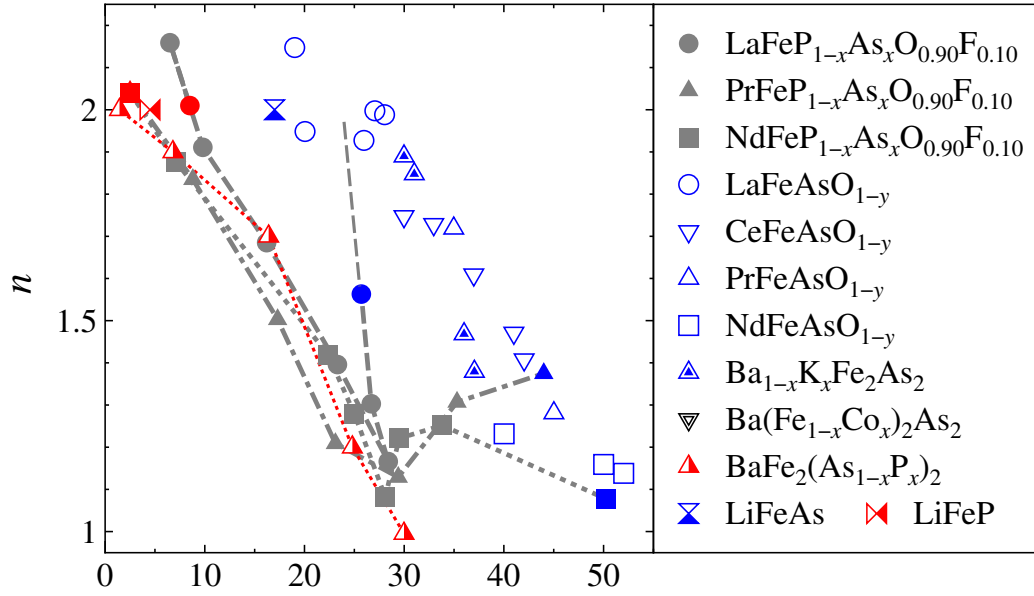
Figure 5.10: Correlation between T_c and n together with superconducting gap structure (Nodeless / Nodal) for various iron pnictide superconductors [16, 21, 56, 61].

Part III

Studies on Single-crystalline NdFeP$_{1-x}$As$_x$(O, F)
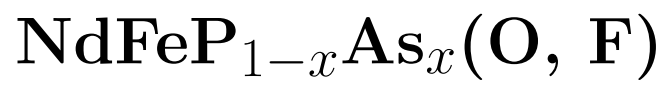
Chapter 6

Experimental methodology

6.1 Single crystal growth of NdFeP$_{1-x}$As$_x$(O, F) by high pressure synthesis

6.1.1 Previous studies of single crystal growth

There are a few reports on single crystal growth of 1111-type iron pnictide. Only two groups constantly succeed in the synthesis of $\sim$ 1 mm sized superconductive single crystals. Both of them use a high pressure technique.

Single crystals of O-deficient PrFeAsO$_{1-y}$ have been obtained by Ishikado *et al.* in National Institute of Advanced Industrial Science and Technology (AIST), Japan [56]. A flat-belt type press machine was used to apply pressure and single crystals were grown by a self flux method using PrAs, Fe$_2$O$_3$, Fe and As. Their synthesis conditions such as applied pressure, heating temperature and heating time are 2 GPa, 1300 - 1400 °C and 2 hours, respectively. A short heating time of 2 hours and the water-cooling press efficiently realized a large temperature gradient in the sample space like Bridgman-method. Reported sample size and T_c were 0.5 - 0.8 mm and 44 K, respectively. Single-crystalline PrFeAsO$_{1-y}$ synthesized by them were provided to various measurements, such as ARPES, magnetic penetration depth measurements and so on.

Single crystals of RFeAs(O, F) (R = Pr, Nd) have been obtained by Zhigadlo *et al.* in Eidgenössische Technische Hochschule Zürich (ETHZ) [62]. A cubic anvil type press machine is used to apply pressure. They adoped the NaAs/KAs flux method and their synthesis condition were slightly different from that in AIST group. In their synthesis, the temperature gradient in

the sample space is smaller than that in AIST group. Applied pressrue and heating temperature in their crystal growth are 3 GPa and 1350 - 1450 °C. The holding time at the maximum temperature and slow-cooling time are 2 - 5 hours and 35 -90 hours. The reported sample size and T_c were 0.4 - 1 mm, 30 K for PrFeAs(O, F) and 39 K for NdFeAs(O, F), respectively.

In the present work, single crystal growth was performed by using a high pressure technique and the self flux method. Our press machine is cubic anvil type and our assembling parts without pyrophyllite are similar to those in AIST group. I grew the single crystals of $NdFeP_{1-x}As_x(O, F)$ in order to clarify the detail of transport properties and the FSs by ARPES measurements.

6.1.2   Procedure of high pressure synthesis of $NdFeP_{1-x}As_x(O, F)$

Precursors NdAs and NdP were synthesized by following the processes described in Capter 3. A composition of $NdFe(P_{1-x}As_x)_{1+\alpha}O_{1-y-\delta}F_y$ was determined as a target of weighting calculation, where x, y, δ and α were As substitution ratio for P site, F substitution ratio for O site, O deficiency ratio for O site and additional (P, As) ratio, respectively. The additional (P, As) was introduced to drop the melting point. The δ and α values are not noted in later chapters and sections. The raw materials are mixed with the below ratio,

$$x\,NdAs + (1-x)\,NdP + \frac{1-y-\delta}{3}\,Fe_2O_3 + \frac{2+y+4\delta}{6}\,Fe + \frac{y}{2}\,FeF_2 + \alpha x\,As + \alpha(1-x)\,P$$

$$\longrightarrow NdFe(P_{1-x}As_x)_{1+\alpha}O_{1-y-\delta}F_y$$
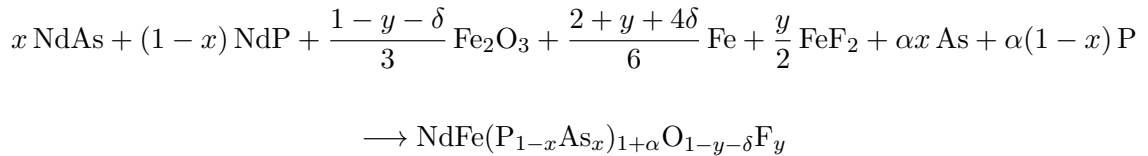
The compositional ratio was often Nd : Fe : (P, As) : O : F = 1 : 1: 1.3 : 0.6 : 0.3 (namely y = 0.3, δ = 0.1 and α = 0.3). The starting materials of NdAs, NdP, Fe_2O_3, Fe, FeF_2, As and P were weighted with the above ratio and mixed in an agate mortar for 20 minutes. The mixture was pressed into a pellet ($\sim$ 2.5 g) under the pressure of 20 MPa.

High pressure synthesis was performed by using cubic anvil type press machine. Assembling parts for high pressure synthesis are shown in Figure 6.1 and Table 6.1.   Pyrophyllites of 1 and 2 in Figure 6.1 have the chemical formula of $Al_2Si_4O_{10}(OH)_2$ and play an important role as pressure media. The pyrophyllite is insulated and moderately soft to deform under pressure. Therefore, it is often used in high pressure synthesis. Stainless steel (SUS) of 3 and molybdenum of 4 in Figure 6.1 are electrodes to connect between the anvil and carbon. Carbons of 5 and 6 in Figure 6.1 are heaters to generate Joule heat by electrical conduction. Boron nitrides (BN) of 7 and 8 in Figure 6.1 construct a sample room and avoid the reaction between the sample
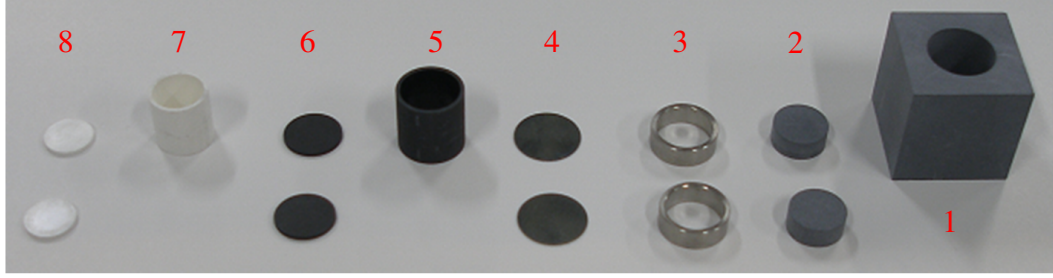
Figure 6.1: Assembling parts for high pressure synthesis.

Table 6.1: The list of assembling parts for high pressure synthesis.

Number	Material	size	No. of pcs.
1	Pyrophyllite	$21 \times 21 \times 21$ mm^3	1
2	Pyrophyllite	$\o10 \times 4$ mm^2	2
3	SUS	$\o12 \times \o10 \times 4$mm^3	2
4	Molybdenum	$\o12 \times 0.3$ mm^2	2
5	Carbon	$\o12 \times \o10.5 \times 12.2$ mm^3	1
6	Carbon	$\o10.5 \times 0.8$ mm^2	2
7	BN	$\o10.5 \times \o9 \times 10.6$ mm^3	1
8	BN	$\o9 \times 0.8$ mm^2	2

and the carbon. Pyrophyllite and BN were dehydrated at 600 °C for 24 hours. The schematic procedure of assembling parts for high pressure synthesis is illustrated in Figure 6.2.

First, six insulated sheets made of polytetrafluoroethylene (Teflon) were attached to the anvils in order to insulate among anvils and to conduct electrical current through carbon and only two anvils. All the parts were assembled and set into cubic anvils. The high pressure synthesis machine and the assembled parts on the anvils are shown in Figure 6.3. The weight applied to the press was often 260 t and it corresponds to the pressure of 3.8 GPa in the sample room. The calibrated relationship between the pressure and the weight is shown in Table 6.2.

Table 6.2: The calibrated relationship between the pressure and the weight.

Pressure (GPa)	Weight (t)
2	70
3	175
4	280
5	390
6	500
7	605
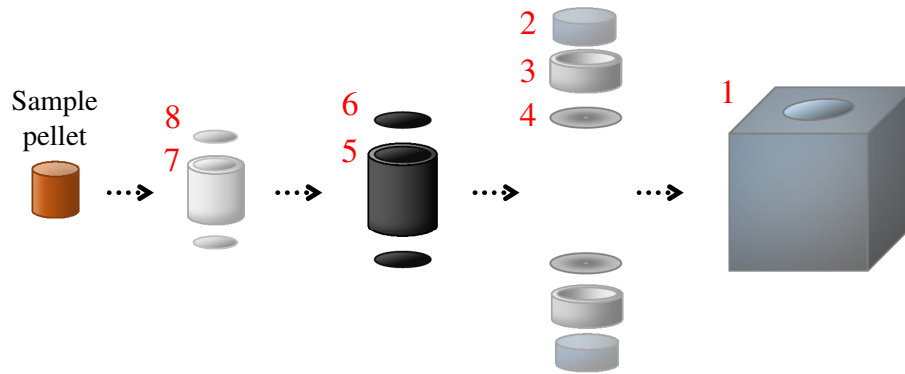
Figure 6.2: Procedure of assembling parts for high pressure synthesis.

Figure 6.3: The high pressure synthesis machine (Left) and the assembled parts on the anvils (Right).

The electronic power of ~ 2000 W applied to the carbon heater, and the sample was heated up to $\sim 1400\,^\circ\text{C}$. One example of the power condition to grow single-crystalline $\text{NdFeP}_{1-x}\text{As}_x(\text{O, F})$ is illustrated in Figure 6.4. Single crystals are expected to grow in the in-plane direction in the
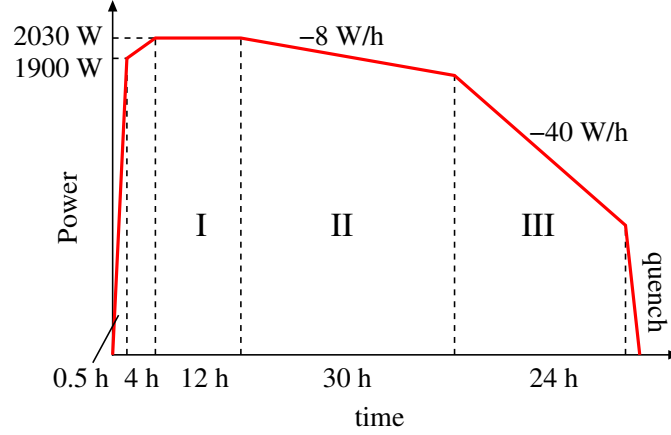
Figure 6.4: One example of the power condition to grow single-crystalline $\text{NdFeP}_{1-x}\text{As}_x(\text{O, F})$.

region I and to grow in the out-of-plane direction in the region II in Figure 6.4. F is introduced into the single crystals in the region III. All anvils were air-cooled during the synthesis in order to avoid breaking anvils and to generate a large temperature gradient in a sample space. In fact, the probability to obtain single crystals in the case of anvil air-cooling was ten times larger than that without air-cooling. Therefore, temperature gradient in the sample space is plays an important factor in the present crystal growth process.

6.2   Measurements

6.2.1   Composition analysis

Composition analysis was performed by using electron probe microanalyzer (EPMA) in The Institute of Scientific and Industrial Research (ISIR), Osaka University and energy dispersive X-ray spectrometry (EDX) in Ashida Lab, Osaka University. 3 - 6 samples were measured by EDX and the composition was defined as the average value.

6.2.2   Magnetic susceptibility and transport measurements

Magnetic susceptibility, electrical resistivity, Hall effect and magnetoresistance were measured in order to discuss physical properties. The measurement procedures for single crystals

were almost the same as the case of polycrystalline samples. Magnetic susceptibility was measured in the magnetic field of 10 Oe parallel to the c-axis. In-plane electrical resistivity and magnetoresistance were measured by using the current perpendicular to the c-axis. Hall coefficient was measured in the magnetic field parallel to c-axis.

6.2.3   ARPES measurement

ARPES is a powerful technique, which can directly observe the dispersion of valence bands and Fermi surfaces. I performed APRES measurements to clarify the x-dependent change of the electronic structure and FSs in $NdFeP_{1-x}As_x(O, F)$ single crystals. Below, I describe the sample preparation, condition of measurement and analysis of ARPES measurement.

Sample preparation

Processes of the sample preparation for ARPES measurement are the following. First, all samples for ARPES measurements were confirmed to have a uniform T_c and show a sharp superconducting transition by magnetic susceptibility measurement. All of them were also confirmed to be a single-domain crystal by taking Laue photograph. Next, parts of the sample holder for the ARPES measurement, which are the base and the sample mount, were prepared. The base and the sample mount were made of Cu and BeCu, respectively. The edge of the sample mount was chipped off with a sand paper to cut off the reflected light from the surface of the sample mount. The top of the sample mount was also scratched to make adhesion between it and Ag paste easy. The sample was attached to the top of the sample mount with Ag paste. They were heated at 120 °C for 30 minutes to harden Ag paste (I confirmed that this heating procedure did not change the temperature dependence of magnetic susceptibility and T_c of the sample). The base and the sample mount were assembled into the sample holder. Interspaces between them was filled with an indium wire (ϕ 1 mm $\times \sim$ 5 mm). The indium wire was used in order to make thermal contact good and to cool the sample down to low temperature. The sample mount was stabilized to the base like the configuration, as illustrated in the left panel of Figure 6.5. In this configuration, the hole and electron FSs can be observed by changing only the tilt angle in the ARPES measurement. The sample alignment was confirmed by taking Laue photograph again (See the right panel of Figure 6.5). At last, an alumina pole (ϕ 1 mm $\times$ 4 mm) for cleaving was stuck to the sample surface with Torr Seal (Pascal Co.) (See the left panel of Figure 6.6). They were heated at 120 °C for 30 minutes to harden Torr Seal.
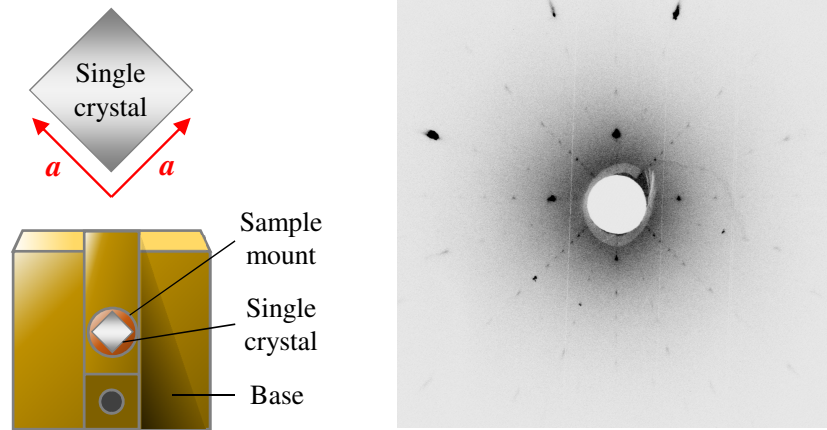
Figure 6.5: The sample location (Left) and the Laue photograph (Right).
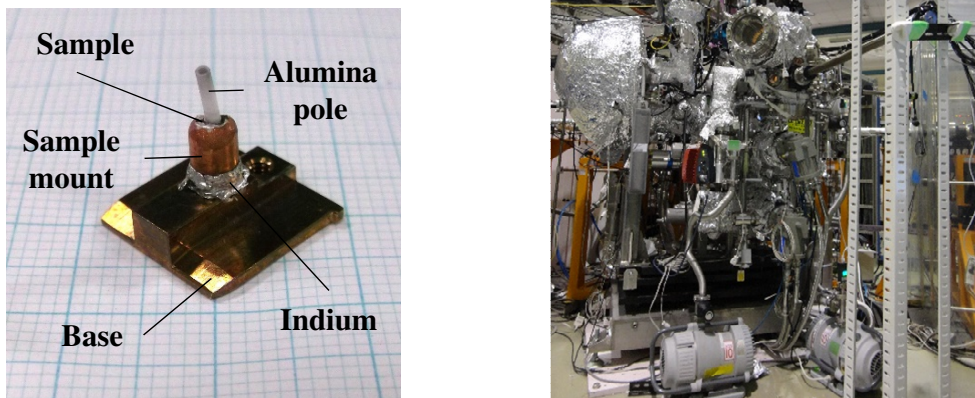
Figure 6.6: The sample holder (Left) and the instrument of the ARPES measurement at BL-7U in UVSOL (Right).

Further processes of the sample preparation performed at BL-7U in UVSOR (the right panel of Figure 6.6) are the following. The sample holder was coated by aero-duck (The Nilaco Co.) to cut off the reflected light. The sample holder was inserted into the cryostat in the vaccum space using a transfer rod. The sample was cooled below 20 K and cleaved to get a clean surface.

Measurements and analysis

In general, the ARPES experiments are performed to detect the energy and momentum distribution of electron in occupied states. The electron is excited by absorption of photons from monochromatized light source. The photoemission processes can be understood by the three step model.

(i) The photon is absorbed and the electron in bulk sample is excited.

(ii) The excited electron moves to the surface through the sample without scattering.

(iii) The electron overcomes the potential of work function Φ and escapes into the vacuum with a kinetic energy E_{kin}.

In the photoemission process, the momentum of electron perpendicular to sample surface is partially lost because of the work function, when the excited electron escapes into the vacuum. On the other hand, its momentum parallel to surface is conversed due to the transition symmetry. Figure 6.7 illustrates a schematic process of photoemission spectroscopy. When the electron in the sample absorbs a photon with sufficiently high energy $h\nu$, it is emitted as a photoelectron. According to the energy conservation and momentum one, the kinetic energy and the momentum are written as follows.

$$E_{\mathrm{kin}} = h\nu - \Phi - |E_{\mathrm{B}}|. \tag{6.1}$$

$$p_{//} = \hbar k_{//} = \sqrt{2mE_{\mathrm{kin}}}\sin\theta. \tag{6.2}$$

Here, E_{B}, p, θ, and m are binding energy, momentum of electron in vacuum, pole angle, and electron mass, respectively. The work function is the energy difference between Fermi level E_{F} and vacuum energy E_{vac}, i.e. $\Phi = E_{\mathrm{vac}} - E_{\mathrm{F}}$. In actual experiment, the kinetic energy measured from E_{F} rather than E_{vac} is observed. Then, it is convenient to write

$$E_{\mathrm{kin}} = h\nu - |E_{\mathrm{B}}|. \tag{6.3}$$

By measurement of kinetic energy of the electron together with the position of detector, the binding energy and the momentum of electron on the 2-dimensional Fe plane can be determined.
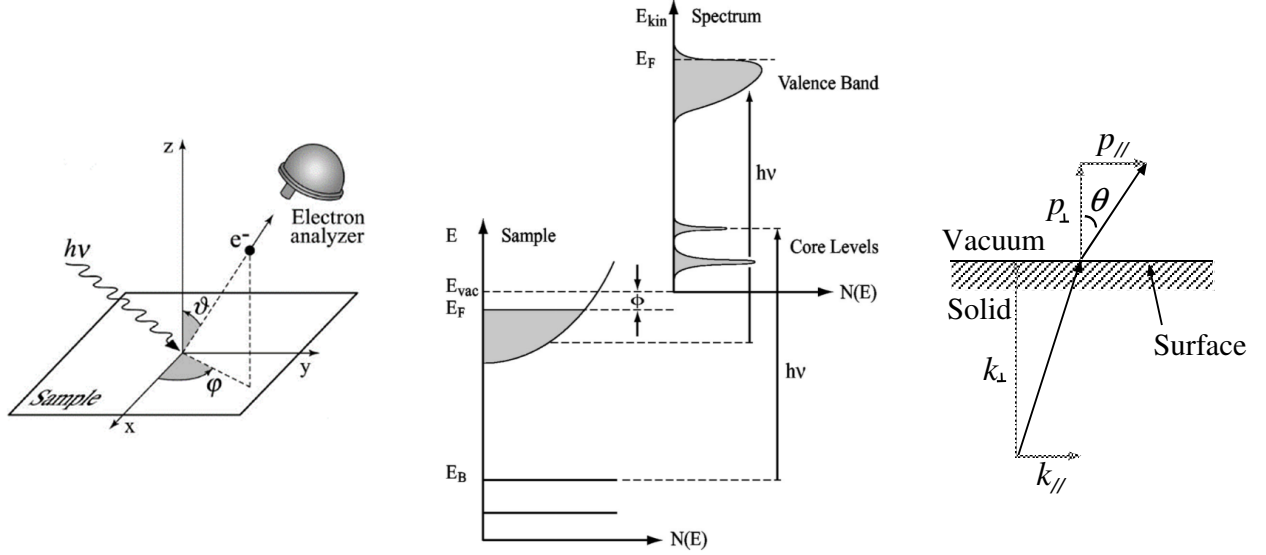
Figure 6.7: Geometry on ARPES measurement (Left) and the photoemission of electrons (Center) and the geometry of a photoelectron on the sample surface (Right) [63].

Figure 6.8 shows the schematic procedure of band mapping by ARPES. By detecting all the electrons with different kinetic energy but with same momentum, we can get the energy distribution curve (EDC). In contrast, the momentum distribution curve (MDC) can be gotten by collecting the electrons with same energy but different momentum. EDC includes the information of density of state. I measured the EDC along several directions on Brillouin zone, and determined the band dispersion. On the other hand, I performed the MDC measurement under the condition of constant energy around E_{F} along many cuts on Brillouin zone, and got the FS mapping.

The iron-based superconductors are multi-band systems, and have several hole- and electron-FSs with different d-orbital characters of Fe. These FSs are expected to have different nesting conditions and different contribution to superconductivity. Therefore, it is important to clarify the orbital characters of each FS (or band) in the present system. When the symmetry of $3d$ orbitals in real space is considered, the photoemission signal of certain orbitals depends on the polarization of incident light generally. In the present ARPES measurement, I used two linear polarization geometries, P and S polarizations. Figure 6.9 shows the experimental setup for polarization dependent ARPES. In P polarization (or S polarization) configuration, the electric
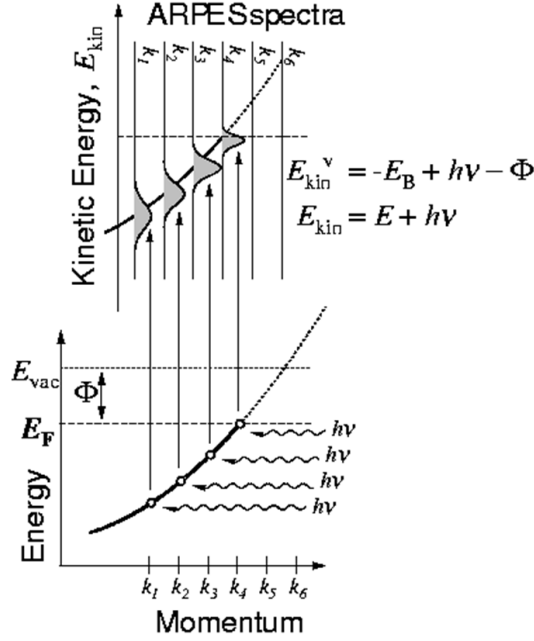
Figure 6.8: The relationship between the ARPES spectra and the band dispersion.

field direction of the incident light is parallel (or perpendicular) to the mirror plane defined by the analyzer slit and sample surface. By measuring the polarization dependence of ARPES along Γ-M with high symmetry, we could determine the orbital character of bands. The bands with d_{xz}, d_{z^2} and $d_{x^2-y^2}$ characters can be observed in the P polarization configuration, while those with d_{yz} and d_{xy} can be detected in the S polarization configuration.
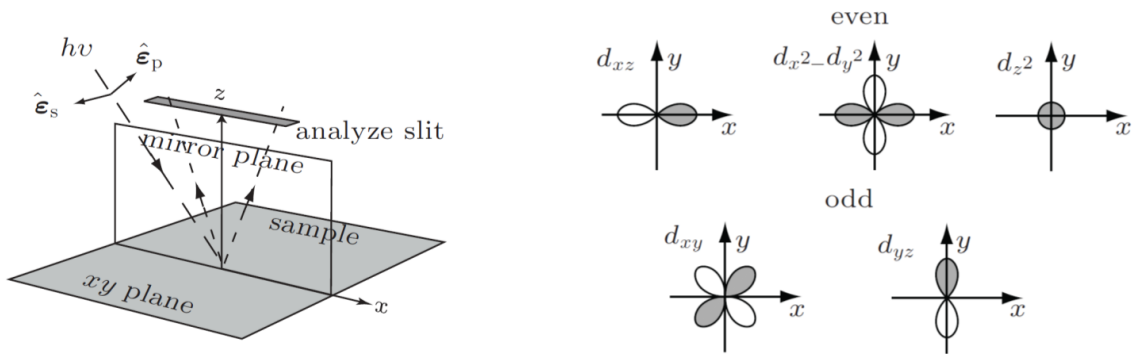
Figure 6.9: The polarized directions of P and S (Left) and the orbital characters of $3d$ electrons (Right) [64].

The ARPES measurement was performed at the SAMURAI end-station of the undulator beamline BL-7U in UVSOR-Ⅲ in the Institute for Molecular Science. Measurement samples were single-crystalline $NdFeP_{1-x}As_x(O, F)$ ($x = 0.4$, 0.8 and 1.0). The measurement temperature is

about 12 K. The light source energy ($h\nu$) is 12 eV - 40 eV. The energy resolution was about 15 meV. The angular resolution was about 0.17°. E_{F} was calibrated using an evaporated Au film.

Chapter 7

Experimental results

7.1 Single crystals of $\mathrm{NdFeP}_{1-x}\mathrm{As}_x(\mathrm{O, F})$ grown by high pressure synthesis

The single crystals of $\mathrm{NdFeP}_{1-x}\mathrm{As}_x(\mathrm{O, F})$ were grown within the sintered pellet. The pellet separated into two pieces and an extracted single crystal of $\mathrm{NdFeP}_{0.4}\mathrm{As}_{0.6}(\mathrm{O, F})$ are shown in Figure 7.1.
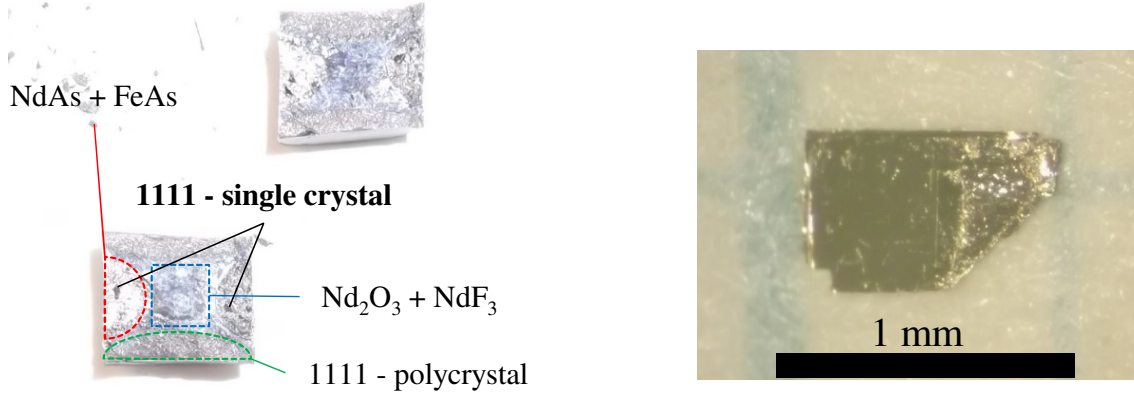
Figure 7.1: A sintered pellet separated into two pieces along the perpendicular direction (Left) and a single crystal of $\mathrm{NdFeP}_{0.4}\mathrm{As}_{0.6}(\mathrm{O, F})$ (Right).

The sintered pellet is mainly separated into three regions of (i) NdAs and FeAs, (ii)$\mathrm{Nd}_2\mathrm{O}_3$ and NdF_3 and (iii) 1111-type polycrystals. The compositions of each region are measured by using EDX. Single crystals were discovered in the region of (i). A typical single crystal size was about $1 \times 1 \times 0.03$ mm^3.

The F concentration estimated by EPMA was ~ 0.05 in a whole x region. In the As end material ($x = 1.0$), no structural transition was observed in the temperature dependence of electrical resistivity and T_{c} is lower than that of an optimal doped sample. According to above facts in the $x = 1.0$ sample, the F concentration is also expected to be 5 - 10 %, which is close to that of EPMA values.

The nominal F content y was 0.3 in most cases. However, the y value cannot be determined by EDX, because the energy of the X-ray absorption peak for Fe is close to that for F. Then only As content x was determined by EDX measurements. The result of the EDX measurements is shown in Figure 7.2 and Table 7.1.
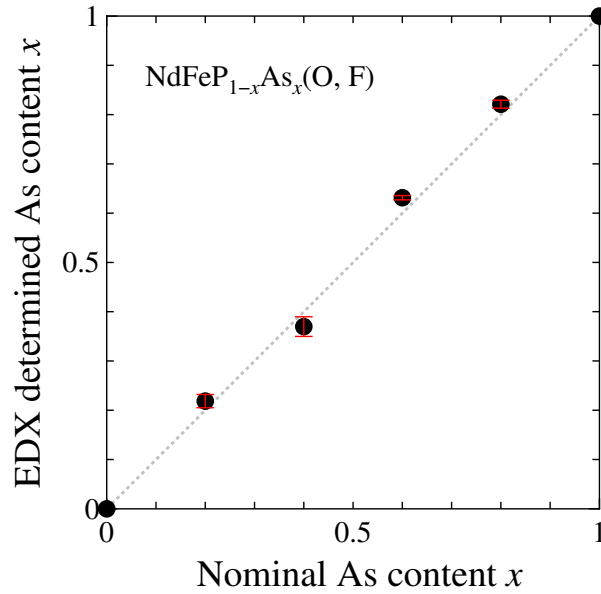
Figure 7.2: The actual As content x determined by the EDX measurement.

Table 7.1: The actual As content x determined by the EDX measurement.

Nominal	EDX
0	0
0.2	0.219(13)
0.4	0.370(20)
0.6	0.631(4)
0.8	0.821(8)
1.0	1

Hereafter, I use the nominal As content as x, because x determined by the EDX measure-

ments is nearly same to the nominal one.

7.2   Magnetic susceptibility

Temperature dependence of magnetic susceptibility of single-crystalline $NdFeP_{1-x}As_x(O, F)$ is presented in Figure 7.3. T_c of grown single crystals in the same batch are almost same. Bulk superconductivity emerged at $x = 0.4$ - 1.0. The T_c of $NdFeAs(O, F)$ was 43.5 K, which is higher than that of the crystals grown by the ETHZ group.
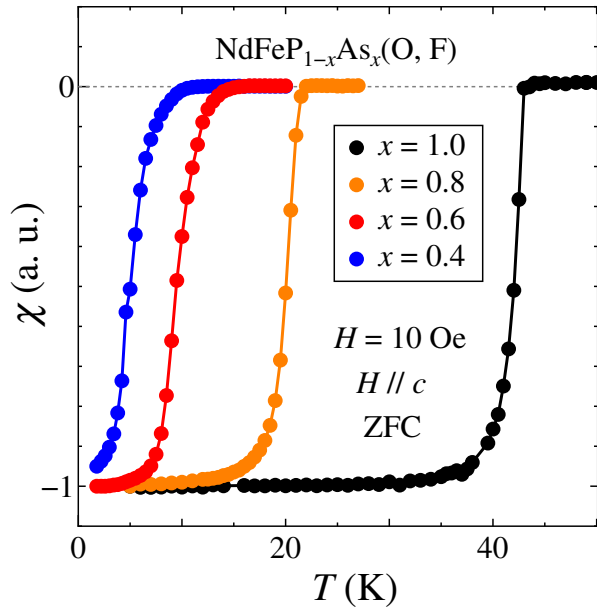
Figure 7.3:   Temperature dependence of magnetic susceptibility of single-crystalline $NdFeP_{1-x}As_x(O, F)$.

7.3   Electrical resistivity

Temperature dependence, double logarithmic plots and fitting curves of electrical resistivity of single-crystalline $NdFeP_{1-x}As_x(O, F)$ are presented in Figures 7.4, 7.5 and 7.6. T_c and the temperature dependence of electrical resistivity hardly changed in the same batch. The residual resistivity ratio (RRR) defined as ρ_{300K}/ρ_{0K} of $NdFeAs(O, F)$ was ~ 5, which is higher than that of the crystals without annealing of the AIST group. The x dependence of T_c, n, A and ρ_0 are discussed in Chapter 9.
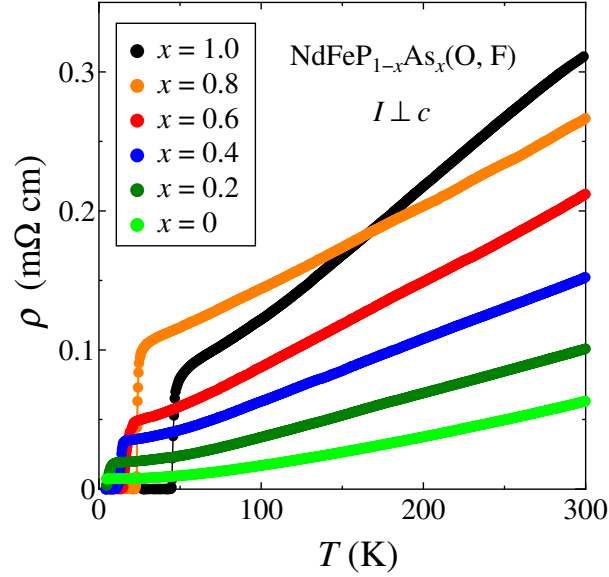
Figure 7.4:   Temperature   dependence   of   electrical   resistivity   of   single-crystalline NdFeP$_{1-x}$As$_x$(O, F).
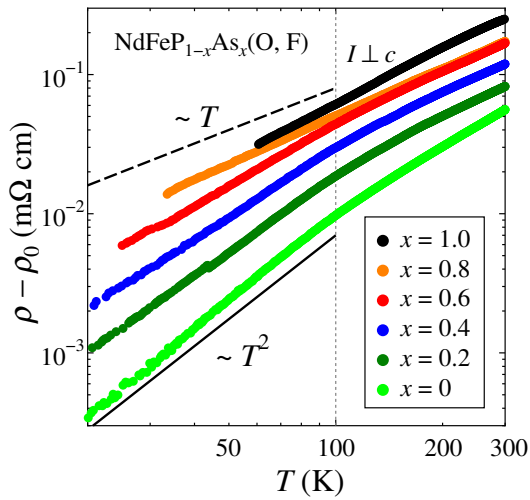
Figure 7.5:   Double   logarithmic   plot   of electrical   resistivity   of   single-crystalline NdFeP$_{1-x}$As$_x$(O, F).
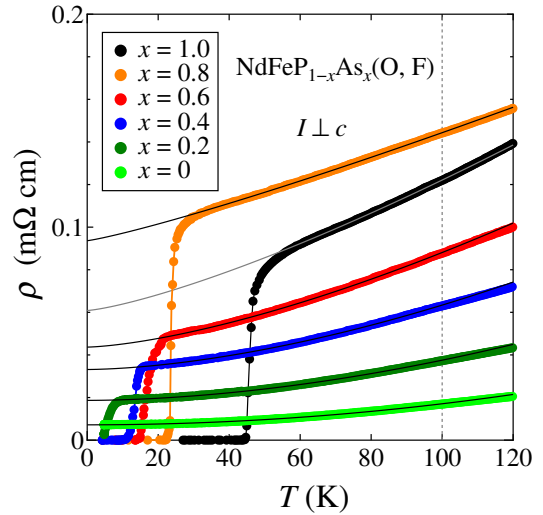
Figure 7.6: Fitting curves of electrical resistivity of single-crystalline NdFeP$_{1-x}$As$_x$(O, F).

7.4 Hall effect

7.4.1 Hall resistivity

Magnetic field dependences of Hall resistivity ρ_{xy} in single-crystalline NdFeP$_{1-x}$As$_x$(O, F) with various x at various temperature are plotted in Figures 7.7 - 7.12. ρ_{xy} is fitted with teh formula $\rho_0 = c_1 H + c_2 H^3$ and c_1 is defined as R_{H}.
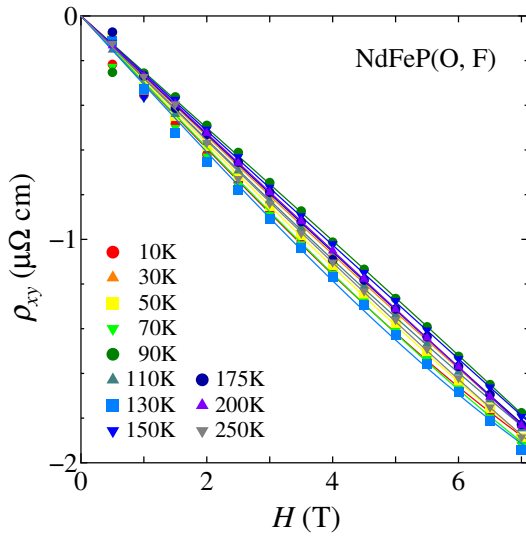
Figure 7.7: Magnetic field dependence of ρ_{xy} of single-crystalline NdFeP(O, F).
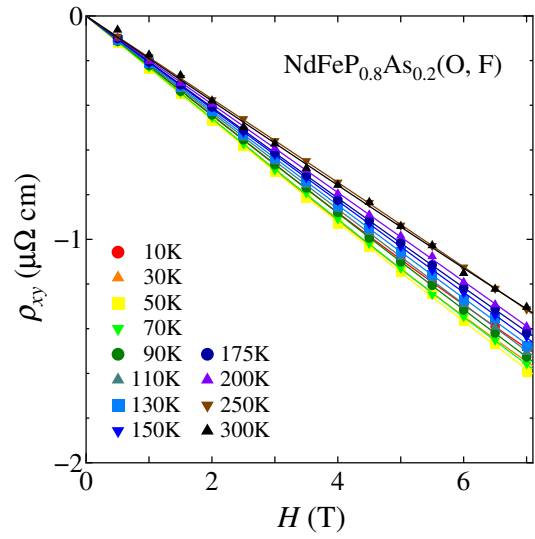
Figure 7.8: Magnetic field dependence of ρ_{xy} of single-crystalline NdFeP$_{0.8}$As$_{0.2}$(O, F).
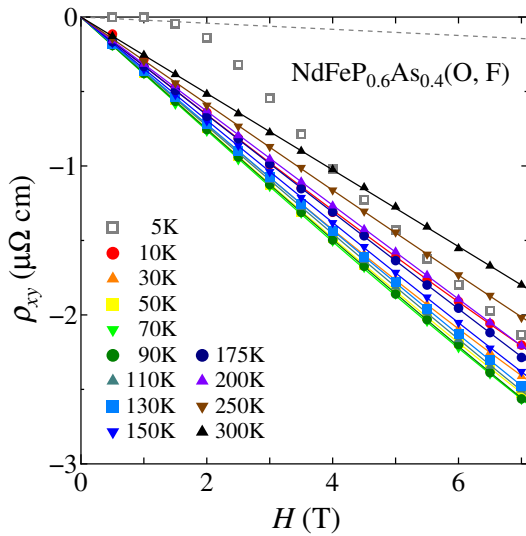
Figure 7.9: Magnetic field dependence of ρ_{xy} of single-crystalline NdFeP$_{0.6}$As$_{0.4}$(O, F).
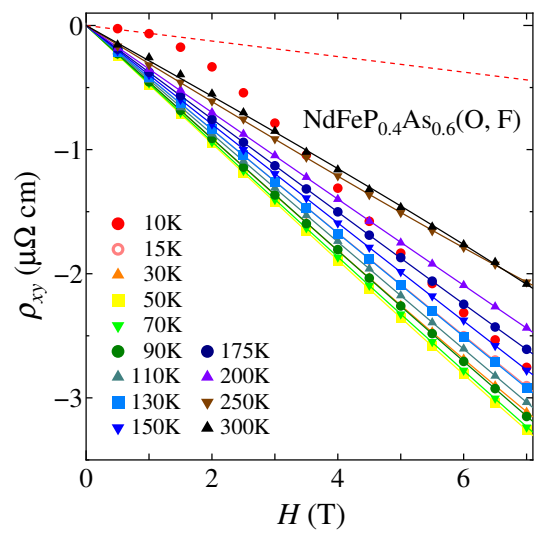
Figure 7.10: Magnetic field dependence of ρ_{xy} of single-crystalline NdFeP$_{0.4}$As$_{0.6}$(O, F).
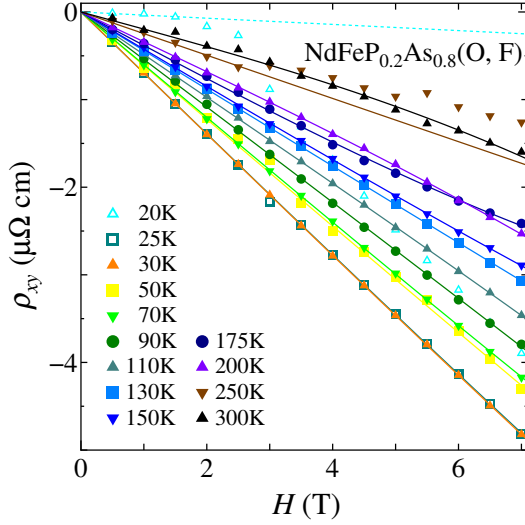
Figure 7.11: Magnetic field dependence of ρ_{xy} of single-crystalline NdFeP$_{0.2}$As$_{0.8}$(O, F).
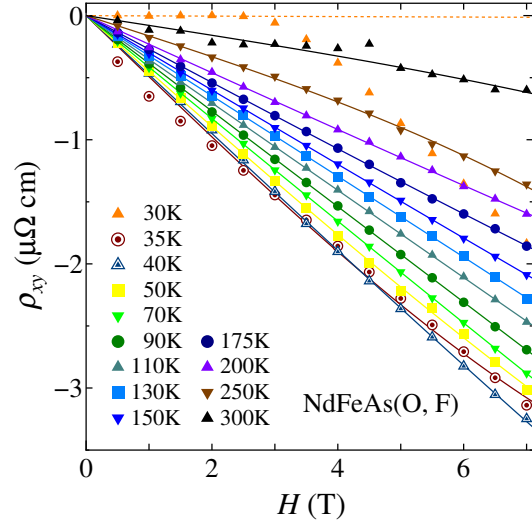
Figure 7.12: Magnetic field dependence of ρ_{xy} of single-crystalline NdFeAs(O, F).

7.4.2   Hall coefficient

Temperature dependence of Hall coefficient of single-crystalline NdFeP$_{1-x}$As$_x$(O, F) with various x shown in Figure 7.13. Temperature dependence of R_H of single-crystalline samples is similar to that of polycrystalline samples. R_H hardly change with temperature at $x = 0$ and 0.2. R_H gradually shows a temperature dependence with increasing x and the strong temperature dependence at $x = 0.8$ and 1.0. $|R_H(T = 300\text{K})|$ / $|R_H(50\text{K})| \sim 5$ at $x = 1.0$ is much smaller than that (~ 2) of the polycrystalline sample. This result is consistent with the previous report of single-crystalline NdFeAsO$_{0.82}$F$_{0.18}$ [65].

7.5   Magnetoresistance

Temperature dependences of magnetoresistance of NdFeAs(O, F) are shown in Figures 7.14 and 7.15. $\rho(T)$ is normalized at 55 K. With applying magnetic field, the resistive transition to superconducting state is broaden, and the suppression of T_c by magnetic field is more remarkable in the case of H // c than the case of $H \perp c$.

Upper critical magnetic field H_{c2} of NdFeAs(O, F) is presented in Figure 7.16. H_{c2} is defined as the magnetic field where $\rho(T)$ drops to 90 %, 70% and 50 % of ρ (55 K), and anisotropic parameter Γ is estimated as 7.7, 4.4, and 4.0, respectively. The Γ values are consistent with those of the previous studies [56].
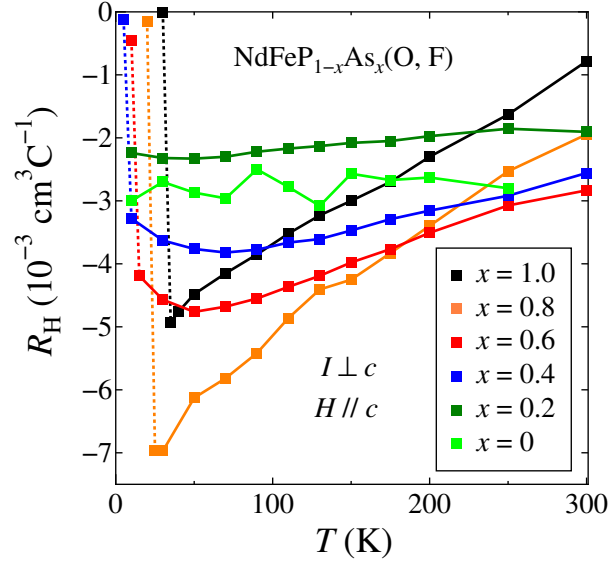
Figure 7.13:   Temperature dependence of Hall coefficient R_{H} of single-crystalline NdFeP$_{1-x}$As$_x$(O, F).
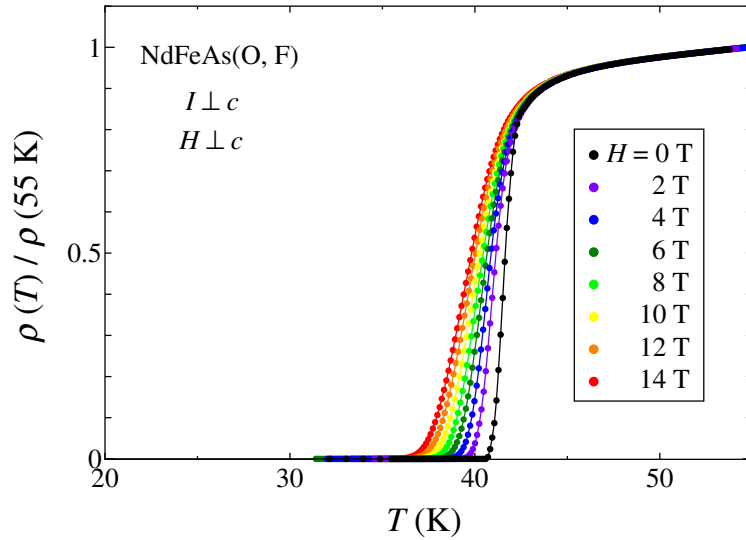
Figure 7.14: Temperature dependences of magnetoresistance of NdFeAs(O, F). The magnetic field was applied in the direction perpendicular to the c-axis.
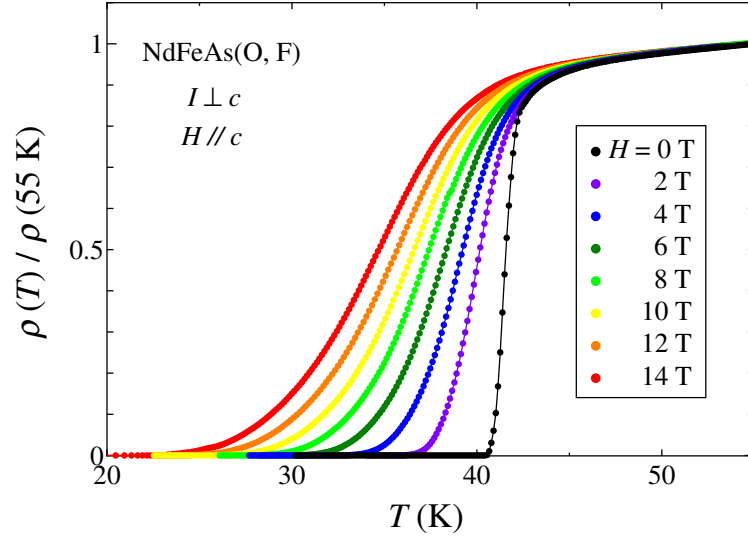
Figure 7.15: Temperature dependences of magnetoresistance of NdFeAs(O, F). The magnetic field was applied in the direction parallel to the c-axis.
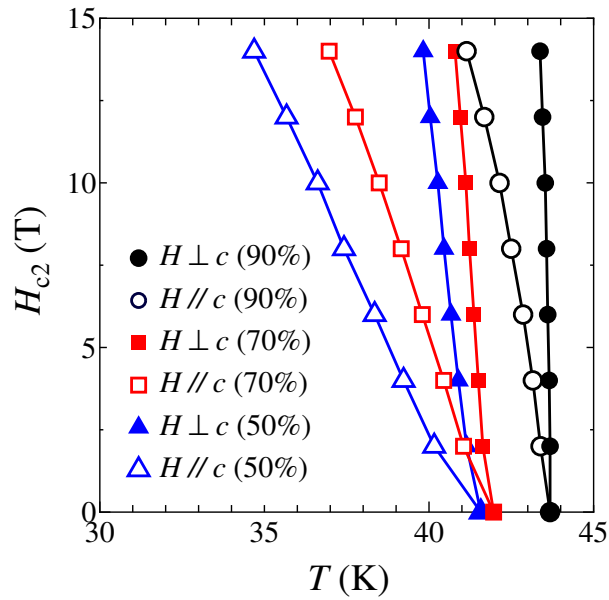
Figure 7.16: Upper critical magnetic field H_{c2} of NdFeAs(O, F).

7.6   ARPES

7.6.1 k_z dependence of FS mapping

The energies of incident light corresponding to Γ and Z points in reciprocal lattice have to be determined by the measurement of the energy dependence of FS mapping. First, the band dispersion along Γ - M direction was measured by using the incident light with the energies of $h\nu = 12$ - 40 eV. Next, the intensity of the MDCs at E_F were measured by using incident light with various energies. The energy dependence of the intensity of MDCs was changed to its k_z dependence by the analysis. FS mapping on k_x - k_z plane in P polarization of NdFeP$_{0.2}$As$_{0.8}$(O, F) is shown in Figure 7.17. There is a cylindrical hole FS around $k_x \sim \pm 0.4$, indicated by
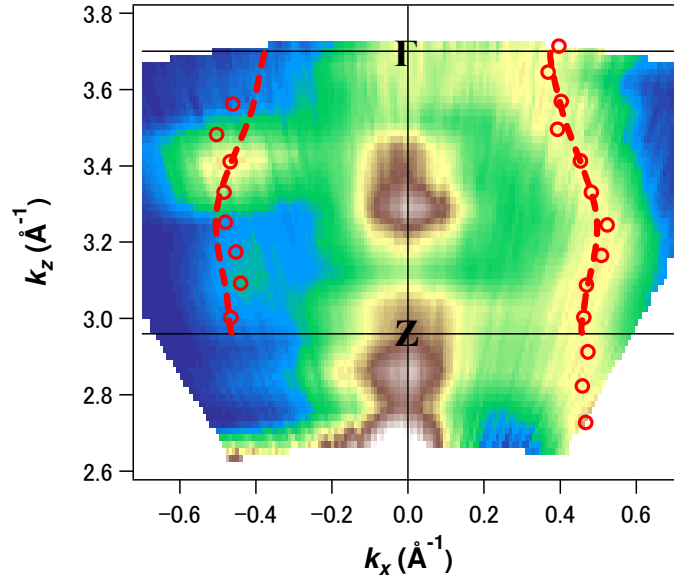
Figure 7.17: FS mapping on k_x - k_z plane in P polarization of NdFeP$_{0.2}$As$_{0.8}$(O, F).

red broken lines in Figure 7.17 (This FS has d_{z^2} orbital character. The detail of assignment of orbital character is described later.). This FS are slightly 3-dimensional and bent. The FS with d_{z^2} orbital character is expected to have a large shrinkage around Γ point. Then I determined that Γ point is located at $k_z = 3.7$, corresponding to the incident energy of 36 eV of incident light. The shape of this FS is similar to that of $x = 0.4$. Lattice constant c of $x = 0.4$ and 1.0 is only 1.1 % smaller and 0.4 % larger than that of $x = 0.8$, and their Brillouin zone sizes along k_z are almost same. Therefore, 36 eV is determined as the energy to detect Γ point in all the samples of the present system.

7.6.2   Band dispersion

Band dispersion along Γ - M direction of NdFeP$_{0.6}$As$_{0.4}$(O, F), NdFeP$_{0.2}$As$_{0.8}$(O, F) and NdFeAs(O, F) are presented in Figures 7.18 - 7.23.
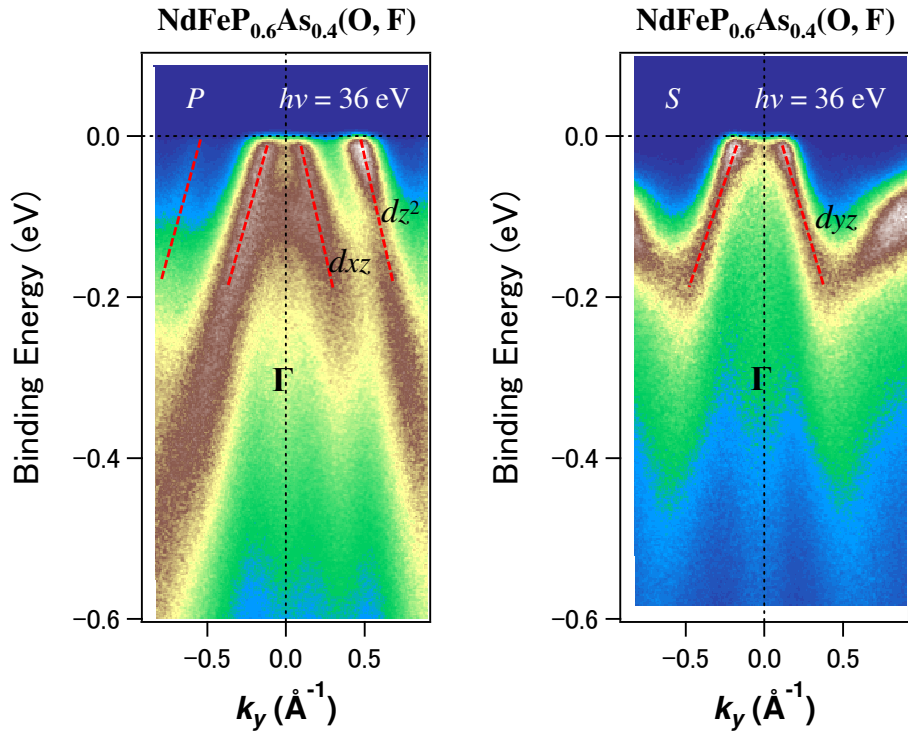
Figure 7.18: *P*- (Left) and *S*- (Right) polarized band dispersion around Γ point of NdFeP$_{0.6}$As$_{0.4}$(O, F).
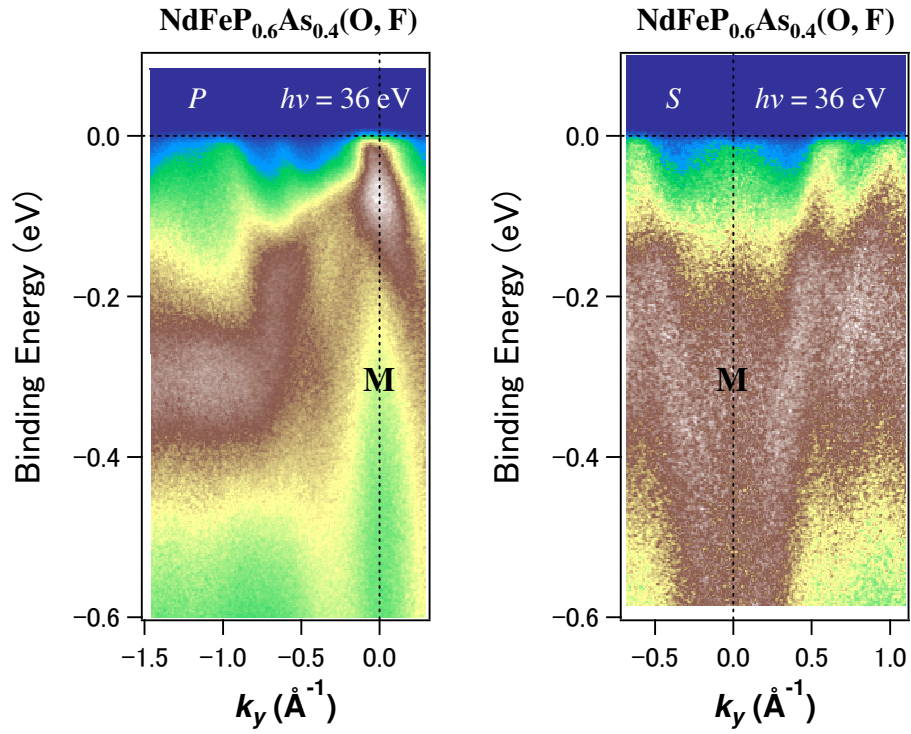
Figure 7.19: *P*- (Left) and *S*- (Right) polarized band dispersion around M point of NdFeP$_{0.6}$As$_{0.4}$(O, F).
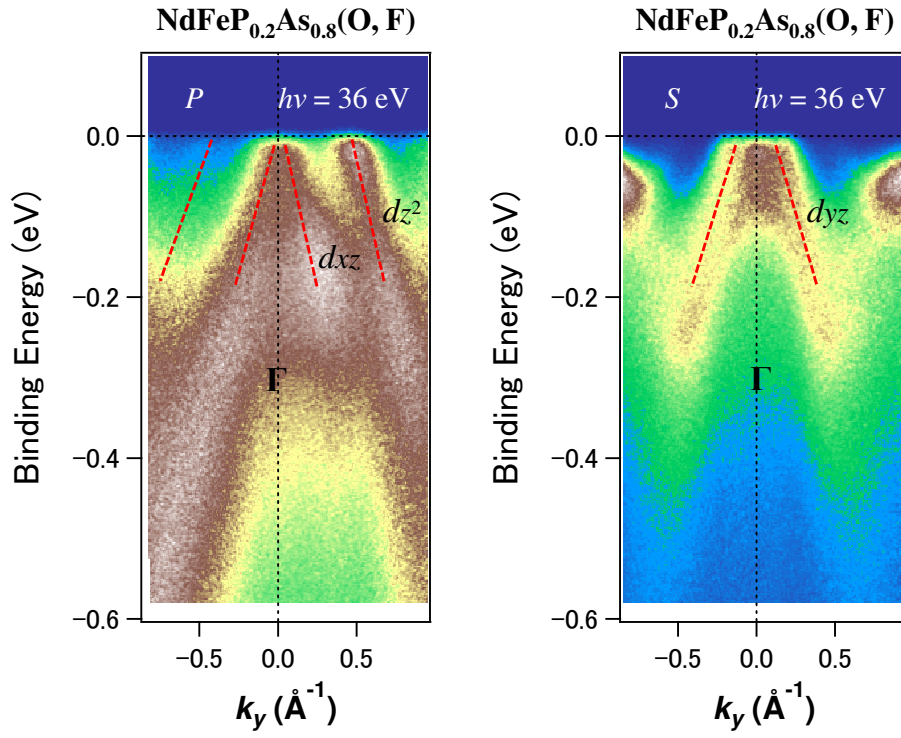
Figure 7.20: *P*- (Left) and *S*- (Right) polarized band dispersion around Γ point of NdFeP$_{0.2}$As$_{0.8}$(O, F).
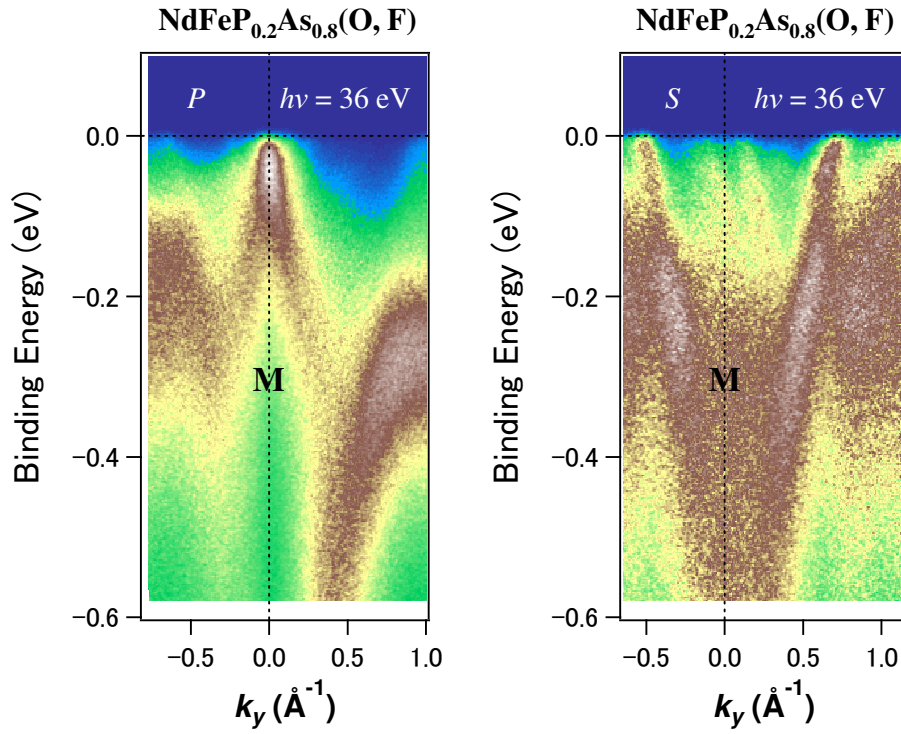
Figure 7.21: *P*- (Left) and *S*- (Right) polarized band dispersion around M point of NdFeP$_{0.2}$As$_{0.8}$(O, F).
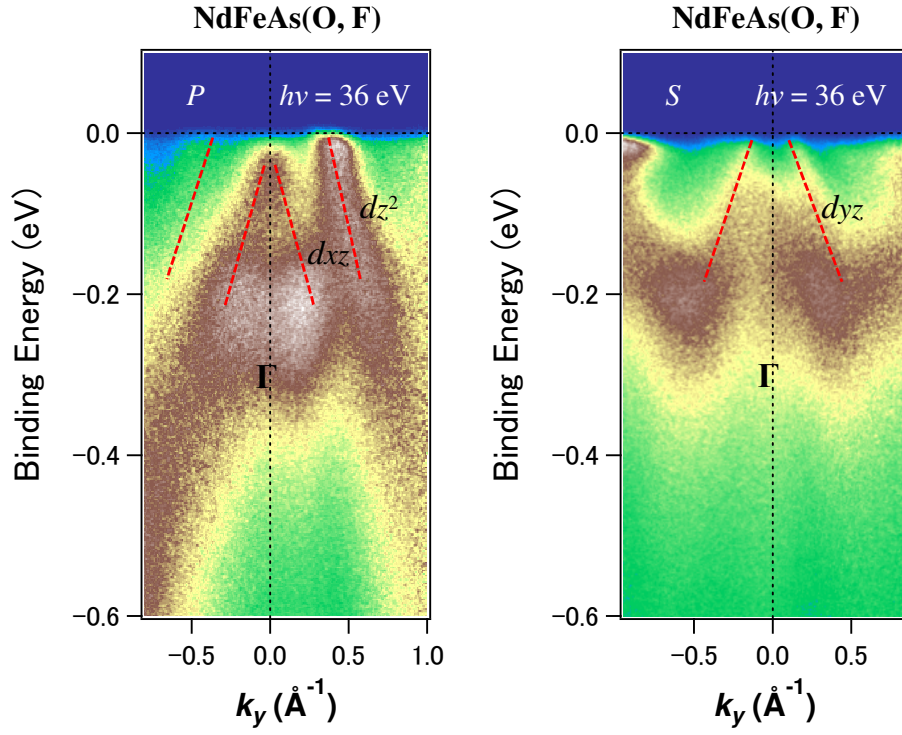
Figure 7.22: *P*- (Left) and *S*- (Right) polarized band dispersion around Γ point of NdFeAs(O, F).
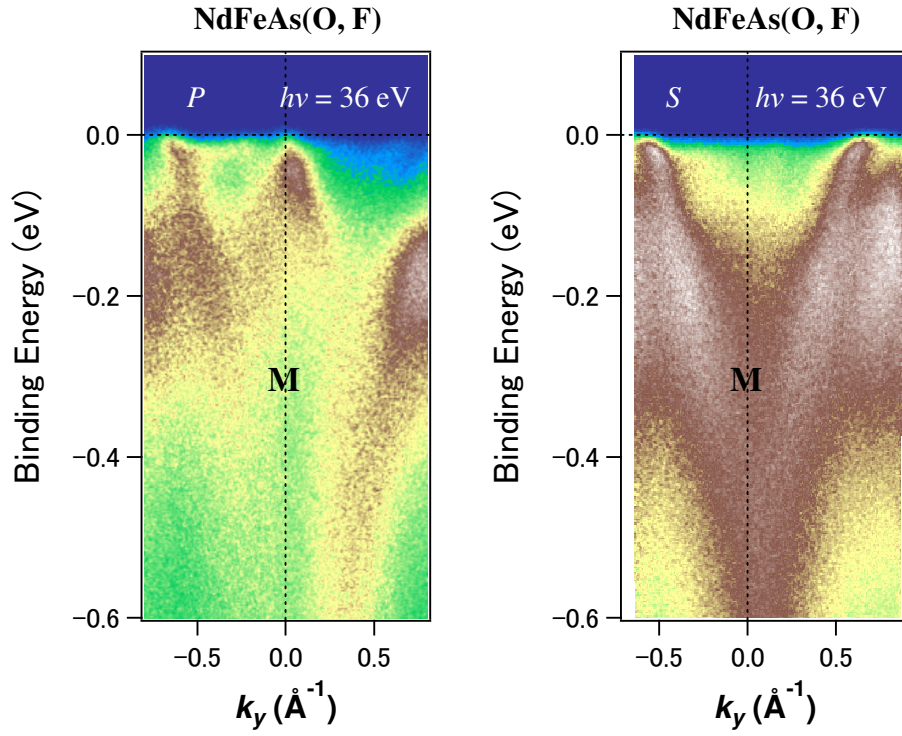
Figure 7.23: *P*- (Left) and *S*- (Right) polarized band dispersion around M point of NdFeAs(O, F).

As shown in the right panels of Figures 7.18, 7.20 and 7.22, one hole band is observed around Γ point in S polarization configuration. Along Γ - M direction in the S polarization, the bands with d_{yz} and d_{xy} orbital characters can be detected around Γ point. This band has a bottom around $k_y = \pm 0.4$ and upturns near M point. This dispersion is consistent with the d_{yz} band in the theoretical study [26]. Resultantly, the present results indicate that the band observed around Γ point in S polarization has d_{yz} orbital character.

As shown in the left panels of Figures 7.18, 7.20 and 7.22, several bands are observed around Γ point in P polarization configuration. In this polarization, the bands with d_{xz} and d_{z^2} characters can be observed. The $d_{x^2-y^2}$ band can be also observed in this polarization, but the theoretical studies have predicted that the bands with the d_{xz} and d_{z^2} orbital characters exist and the $d_{x^2-y^2}$ band does not appear. The band calculation also has demonstrated that the d_{xz} and d_{yz} bands almost degenerated around Γ point. Therefore, the band most near Γ point in the P polarization is assigned to one with d_{xz} orbital character. This d_{xz} band sinks with increasing As content x. Other broad band around Γ point have been observed in all the samples. This band may have d_{z^2} orbital character, but the existence of this broad band is not consistent with the theoretical studies. In LaFePO, the previous ARPES study has clarified the appearance of the same broad band around Γ point. The surface effect may be related with the appearance of this band. The band dispersion and related large FS with d_{z^2} character, described later, suggest that the sample surface is hole-doped and the top layer on the smple surface may be FePn layer.

Figures 7.19, 7.21 and 7.23 show the band dispersion around M point in the P and S polarization configuration in the $x = 0.4$, 0.8 and 1.0 samples. The band calculation indicates the existence of two electron-like bands around M point. Around M point, the present ARPES intensity has finite values, suggesting the existence of density of states at E_F. The finite intensity of ARPES is due to the electron-like bands with d_{xz} and d_{yz} characters predicted by the theoretical study.

7.6.3   Hole and electron FSs around Γ and M Points

In NdFeP$_{1-x}$As$_x$(O, F) with $x = 0.4$, 0.8 and 1.0, I measured the MDCs at E_F along many cutting lines on Brillouin zone, and mapped FSs on k_x - k_y plane at $k_z = 0$, which include Γ and M points. Figures 7.24, 7.25 and 7.26 show the maps of FSs on k_x - k_y plane at $k_z = 0$ by using P and S polarization configurations in the $x = 0.4$, 0.8 and 1.0 samples, respectively. The MDCs have several peaks, revealing the finite value of density of state at E_{F}, i.e. the existence

of FS. I fitted these peaks of MDCs by using Lorentz model, and the open circles indicate the positions of peak center of MDCs in Figures 7.24, 7.25 and 7.26. I connected these circles by the broken lines with circle shapes. In other words, the broken lines show the FSs. In principle, the FSs should be almost isotropic. However, the intensity of EDCs and FSs are anisotropic. This is due to measurement setting. In the EDC measurements, I fixed the direction of incident light and the position of the detector, while the samples was rotated and tilted. These rotations and tilting of the sample cause the anisotropic intensity of EDCs and FSs.

I briefly explain the relation between the band dispersion shown in Figures 7.18 - 7.23 and the map of FSs in Figures 7.24 - 7.26. In Figures 7.18 - 7.23, I show the band dispersions along k_y (Γ - M direction). This k_y direction corresponds to the vertical Γ - M one in Figures 7.24 - 7.26.

First, please see the lower panels in Figures 7.24 - 7.26. There are small and large FSs around Γ point. The analysis of band dispersion, described in previous section, indicates the existence of one hole FS with d_{yz} orbital character. The small FS around Γ point in the map for S polarization configuration corresponds to hole FS with d_{yz} character. As shown in the lower panel of Figure 7.24, other small FS is drawn by broken line around Γ point. This is the small hole FS with d_{xz} orbital character, observed in the P polarization and shown in the upper panel in Figure 7.24. For comparison, I show this d_{xz} FS in the lower panel in Figure 7.24. I also represent the larger FS with d_{z^2} character around Γ point observed in the P polarization configuration in the lower panels in Figures 7.24 - 7.26.

In the lower panels of Figures 7.24 - 7.26, there are larger FSs. The origin of these FSs is not clear. These FSs' area is similar to that of the d_{z^2} FS. In the S polarization, however, the d_{z^2} FS cannot be observed. The surface effect may affect not only the d_{z^2} but also d_{xy} bands. The larger FS may have the d_{xy} orbital character and be caused by the surface effect.

Around M point in the lower panels in Figures 7.24 - 7.26, there is one FS. The theoretical study indicates the existence of electron-like FSs with d_{xz} and d_{yz} characters. This FS around M point observed in the S polarization can be assigned to the electron FS with d_{yz} character. In the lower panels in Figures 7.24 - 7.26, I also show the small FSs around M point, which are observed in the P polarization configuration and represented in the upper panels of these figures.

Next, please see the upper panels in Figures 7.24 - 7.26. The FSs observed in the S polarization are also shown in these panels for comparison. As shown in the upper panel of Figure

7.24, there are small and large hole FSs around Γ point. From the analysis of band dispersion in the previous section, the small and large FSs in the $x = 0.4$ sample have d_{xz} and d_{z^2} orbital characters, respectively. As shown in the upper panels of Figures 7.25 and 7.26, the small FS with d_{xz} character disappears and the area of large FS shrinks with increasing As concentration x. The detail of these FSs' behaviors is discussed later. Around M point, there is one FS. Perhaps, this FS is electron on with d_{xz} character.
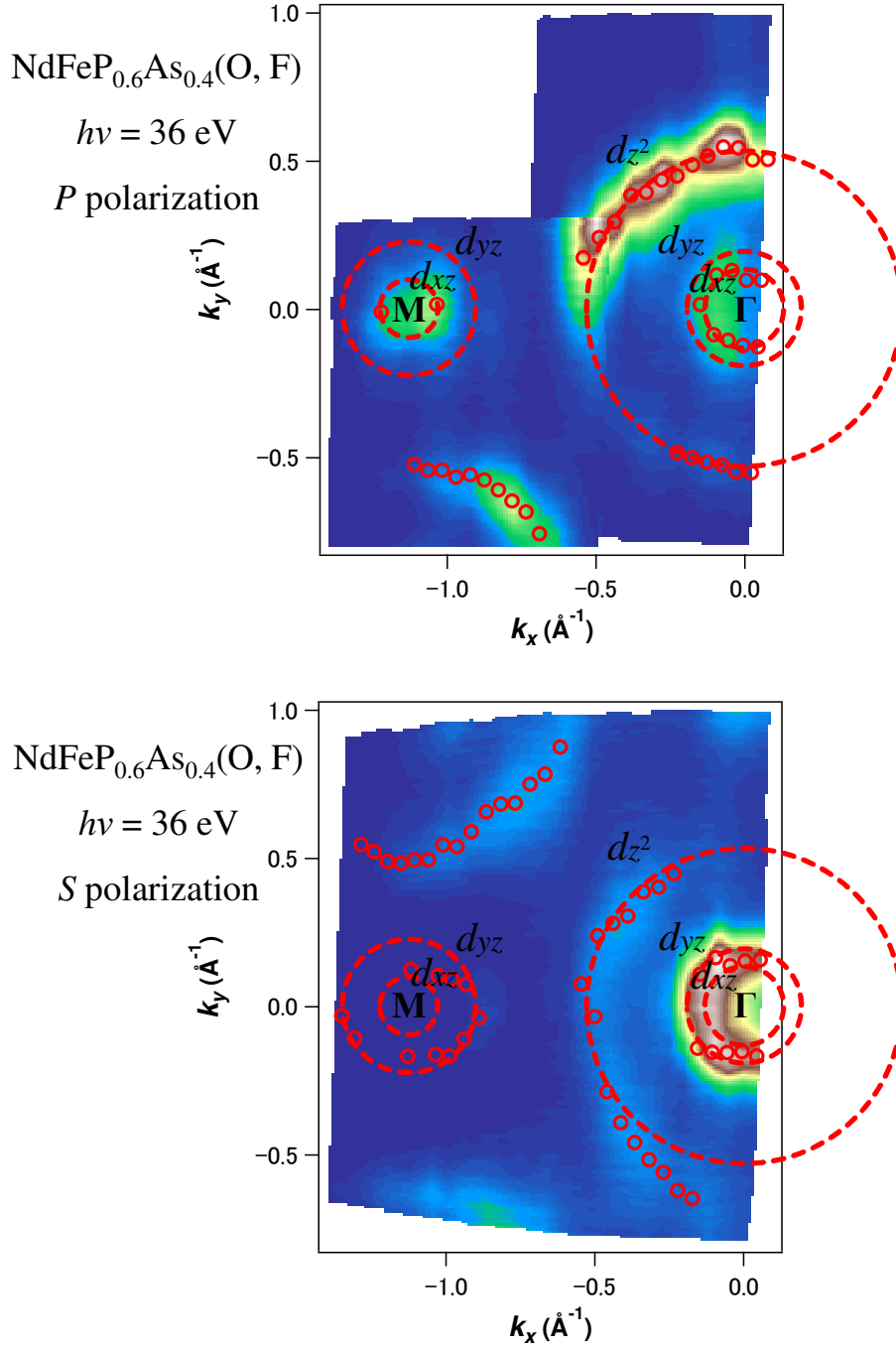
Figure 7.24: Maps of intensity of MDCs on k_x - k_y plane at $k_z = 0$ and at E_F in NdFeP$_{0.6}$As$_{0.4}$(O, F). Upper and lower panels show the results in P and S polarization configurations, respectively. The energy of incident light is 36 eV. The bright and dark colors indicate the higher and lower intensities of MDCs.
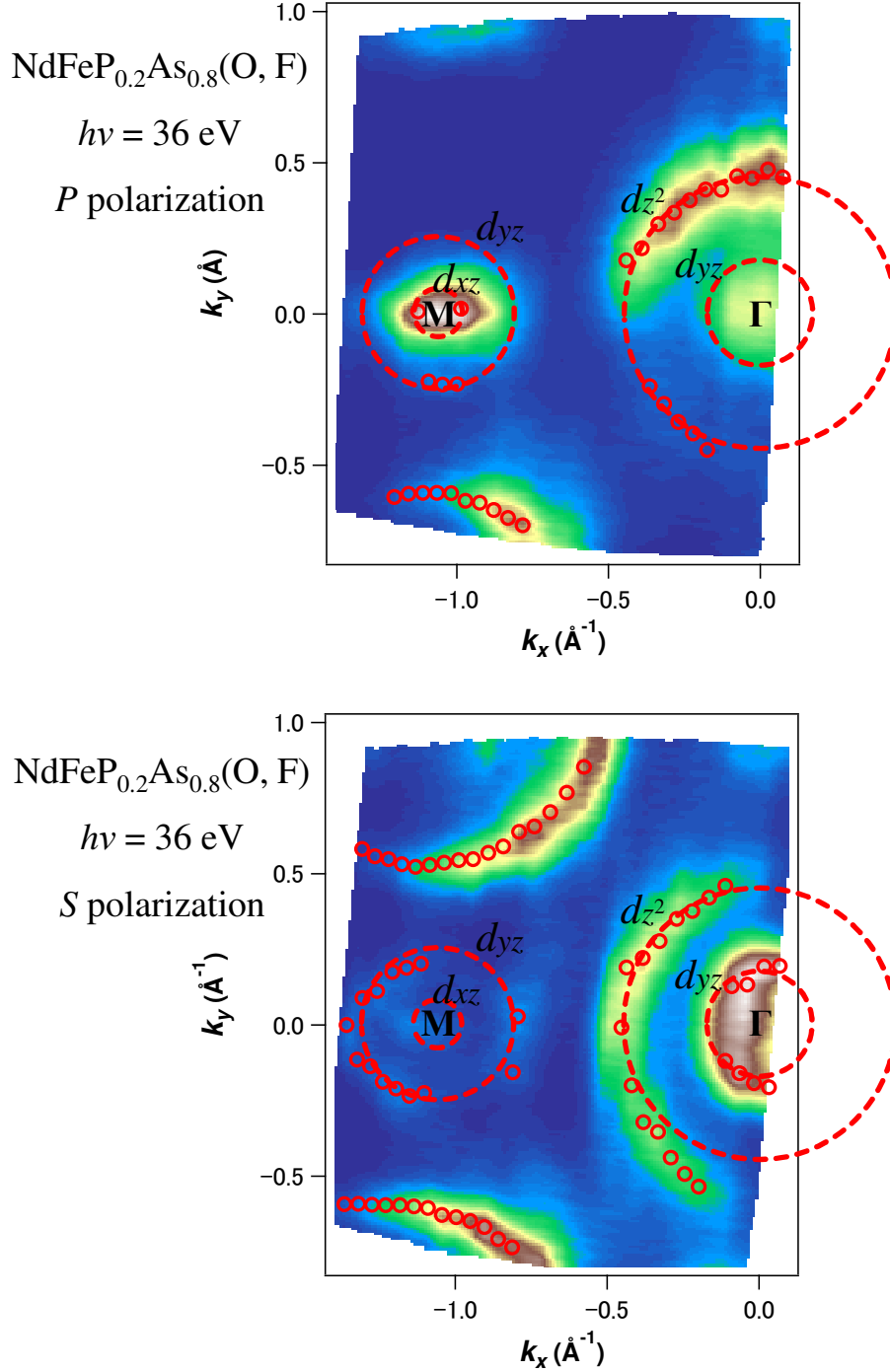
Figure 7.25: Maps of intensity of MDCs on k_x - k_y plane at $k_z = 0$ and at E_F in NdFeP$_{0.2}$As$_{0.8}$(O, F). Upper and lower panels show the results in P and S polarization configurations, respectively. The energy of incident light is 36 eV. The bright and dark colors indicate the higher and lower intensities of MDCs.
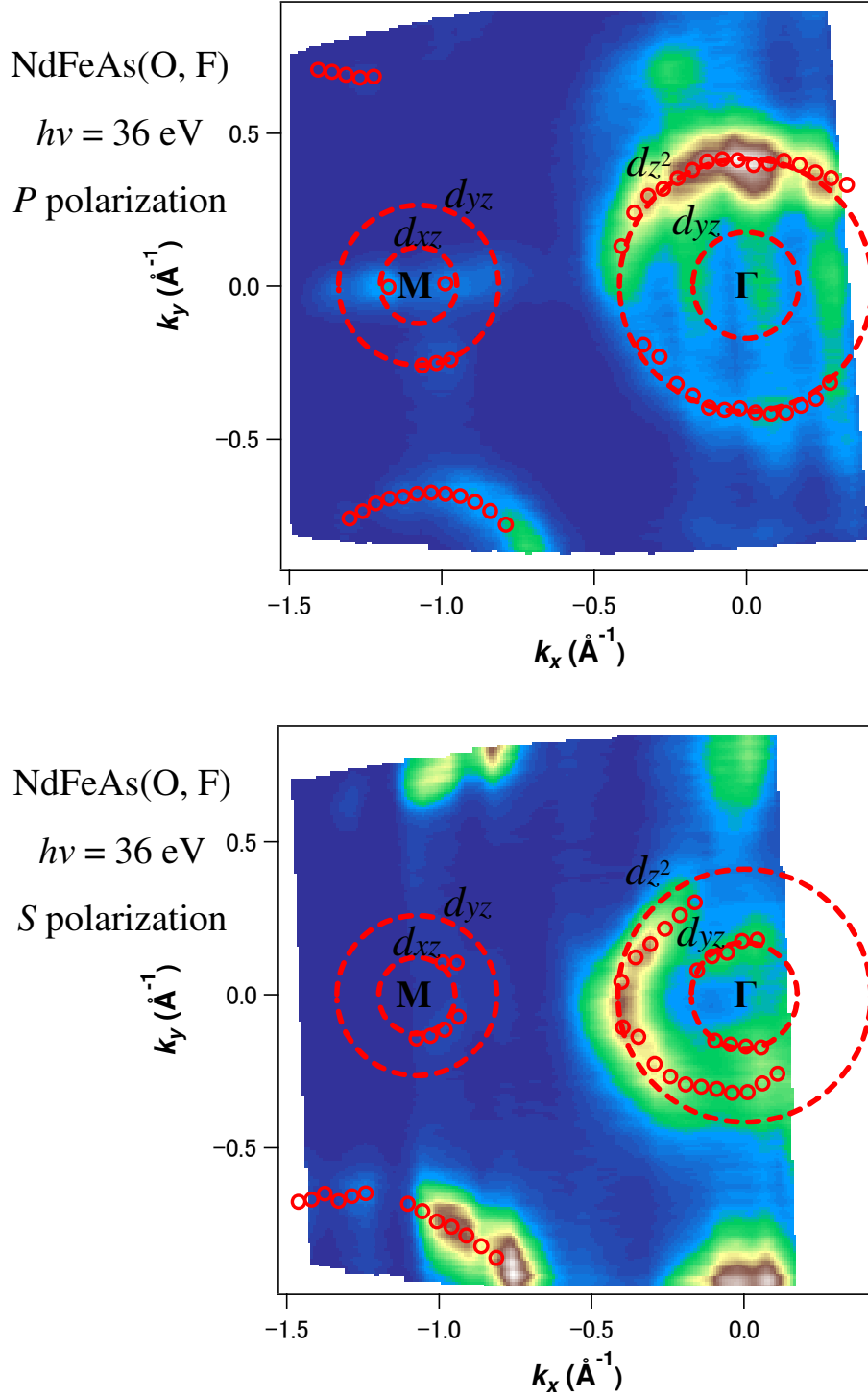
Figure 7.26: Maps of intensity of MDCs on k_x - k_y plane at $k_z = 0$ and at E_F in NdFeAs(O, F). Upper and lower panels show the results in P and S polarization configurations, respectively. The energy of incident light is 36 eV. The bright and dark colors indicate the higher and lower intensities of MDCs.

Chapter 8

Discussion

8.1 Transport properties

8.1.1 x dependences of T_c and n

T_c and the power n are determined in the same way as the case of polycrystalline samples. T_c and n are plotted as a function of As content x in Figure 8.1. T_c of single-crystalline $NdFeP_{1-x}As_x(O, F)$ (red) is lower than that of polycrystalline $NdFeP_{1-x}As_xO_{0.9}F_{0.1}$ (gray) for all x. This is caused by the lower F concentration of single-crystalline samples than that of polycrystalline ones. The nonmonotonous x dependence of n is also observed in single-crystalline samples. Therefore, x dependence of n in polycrystalline samples is caused by not the grain boundary effect but an essential physical property. The x dependence of T_c and n for single crystals indicates a correlation between T_c and n in the region of x $x = 0$ - 0.8 but no correlation above $x > 0.8$. T_c increases from ~ 0 K to 23.6 K and n decreases from 2.0 to 1.16 in the region of $x = 0$ - 0.8. This suggests that T_c is enhanced by the AFM fluctuation in this region. On the other hand, no relationship is observed in the region of $x = 0.8$ - 1.0. The boundary x composition changes from $x = 0.6$ in polycrystalline samples to $x = 0.8$ in single crystals. This may be caused by the difference of their carrier concentration. In fact, the electronic phase diagrams and the boundary composition are different in $LaFeP_{1-x}As_xO_{0.9}F_{0.1}$ and $LaFeP_{1-x}As_xO_{0.95}F_{0.05}$.

8.1.2 x dependence of ρ_0 and A

The x dependences of ρ_0 and A in $NdFeP_{1-x}As_x(O, F)$ are shown in Figure 8.2. ρ_0 and A cannot be discussed rigorously in the cases of polycrystalline samples because of the grain
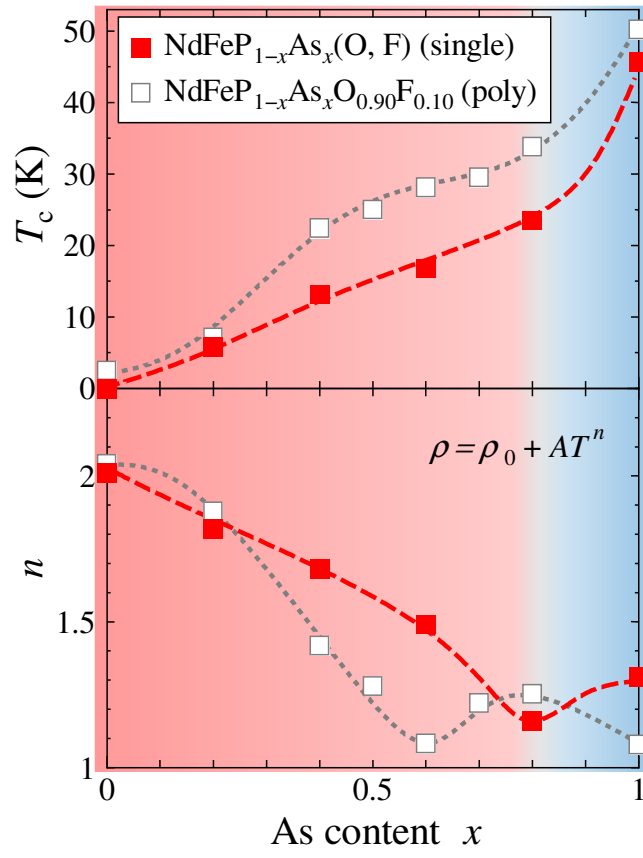
Figure 8.1: x dependences of T_c and n in NdFeP$_{1-x}$As$_x$(O, F).
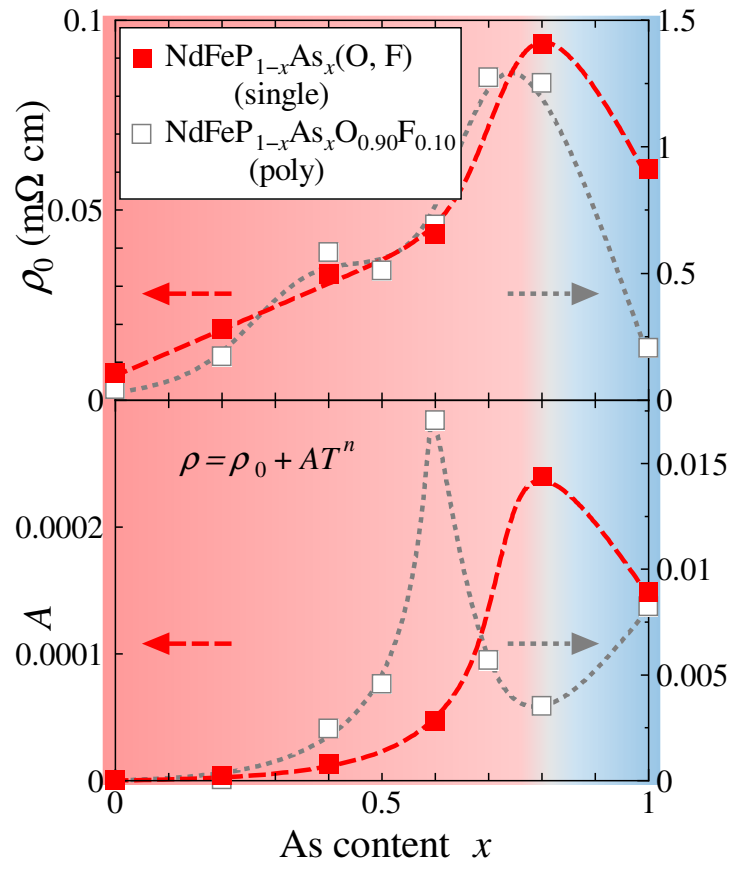
Figure 8.2: x dependence of ρ_0 and A in $\mathrm{NdFeP}_{1-x}\mathrm{As}_x(\mathrm{O, F})$.

boundary effect. However, in the cases of single-crystalline samples, there is no grain boundary effect, and ρ_0 and A can be discussed. Both of ρ_0 and A change systematically and they are enhanced at $x = 0.8$, where n approaches ~ 1. ρ_0 and A increase with x in the region of x = 0 - 0.8 and decrease with x in the region of x = 0.8 - 1.0. The x dependences of ρ_0 and A of single crystals are similar to that of polycrystals. Therefore, the results of polycrystals are also valid for discussion. As well as T_c and n, the enhancements of ρ_0, A and $|R_H|$ around x = 0.6 $\sim$ 0.8 may be also connected with non-Fermi liquid behavior in the present system. I point out that similar enhancements of R_H, ρ_0, A, and T_c together with T-linear resistivity were observed in CeCu$_2$(Si, Ge)$_2$ [66, 67, 68]. Apart from a magnetic quantum critical point in the pressure-T phase diagram, this heavy fermion compound shows another critical behavior at a higher pressure where the T_c reaches the highest value. The observed anomalies were interpreted as a result of the rapid change of the Ce valence. Watanabe *et al.* successfully explained these anomalies by the microscopic theory for valence fluctuation based on an extended Anderson model [69]. In the case of the present iron based superconductor, the P/As substitution is an isovalent substitution in a chemical sense. However, it is likely that the exchange of band energy with x (the band with some d orbital character is lifted up above E_F or other band shifts down below E_F.) causes valence (charge) fluctuation near the critical composition x = 0.6 - 0.8. Below x = 0.6 - 0.8, not only the AFM fluctuation but also this charge fluctuation gradually may increase with x and cause the enhancement of T_c. Actually, the ARPES results indicate that the FS with d_{xz} orbital character disappears around $x \sim 0.8$. This change of FS may be related with the anomalous transport properties around $x \sim 0.8$.

8.1.3 x dependence of R_H at $T = 50$ K

As reported in the previous paper, the absolute values of R_H in single crystals are lower than those in polycrystalline samples. However, the single crystals and polycrystalline samples show similar x dependence of R_H, i.e. $|R_H|$ is enhanced at x = 0.6 - 08, where n approaches to ~ 1. x dependences of R_H at $T = 50$ K and n in NdFeP$_{1-x}$As$_x$(O, F) are plotted in Figure 8.3. $|R_H|$ is enhanced at $x = 0.8$, where n approaches ~ 1. Therefore, the band crossing of d_{Z^2} and $d_{X^2-Y^2}$ are suggested like polycrystalline RFeP$_{1-x}$As$_x$O$_{0.9}$F$_{0.1}$. x dependence of R_H of single-crystalline samples is more gradual than that of polycrystalline ones. This may be related to the anisotropy of the crystals.
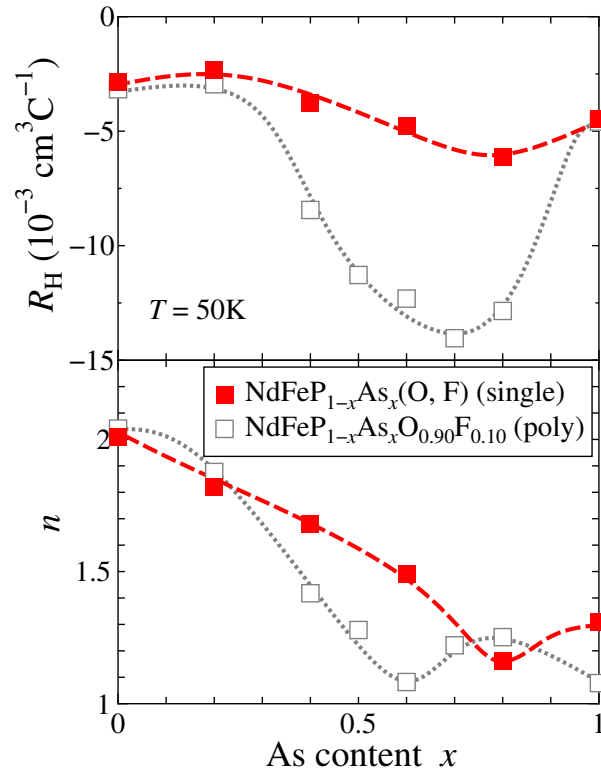
Figure 8.3: x dependence of R_{H} at $T = 50$ K and n in NdFeP$_{1-x}$As$_x$(O, F)

8.1.4   Correlation between T_c and n

Correlation between T_c and n in $NdFeP_{1-x}As_x(O, F)$ is presented in Figure 8.4. The data point for $x = 0$ - 0.8 of $NdFeP_{1-x}As_x(O, F)$ are on the same scaling line for $x = 0$ - 0.6 of polycrystalline samples. The present results indicate that the AFM and/or other fluctuations enhance T_c in lower x region, and the end point for T_c - n correlation in lower x region is located at $x \sim 0.8$. All the results of transport measurements are qualitatively the same in poly- and single crystals. This guarantees my discussions systematic.
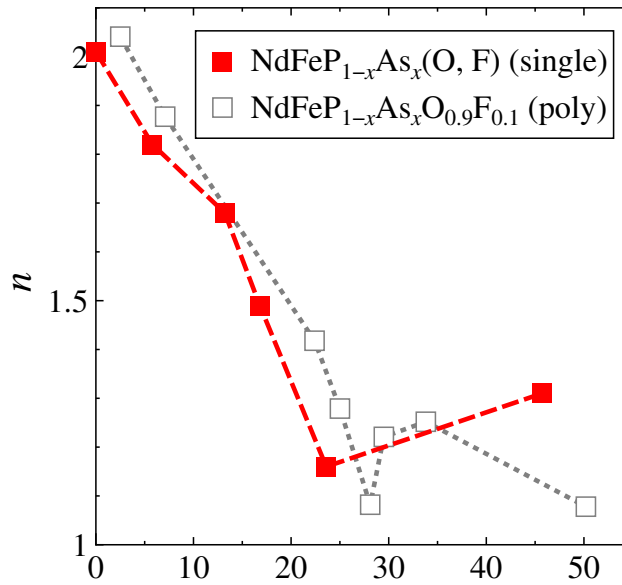
Figure 8.4: Correlation between T_c and n in $NdFeP_{1-x}As_x(O, F)$

8.2   ARPES measurement

8.2.1   Comparison with band calculation

Three or two hole FSs around Γ and two electron FSs around M are observed in all samples. Especially, two small hole FSs and two electron FSs observed in $x = 0.4$ are consistent with the band calculation result of 1111 system. However, the largest hole FS constructed of the d_{z^2} band (and perhaps with the d_{xy} one) is not predicted by band calculation. It is not also detected by dHvA measurements of LaFePO. On the other hand, the large hole FS is observed in all ARPES measurements of 1111 system, where R is La, Pr, Nd or Sm and Pn is P or As. The nodeless

superconducting gap of $\Delta = 15$ meV is also reported on this FS in NdFeAs(O, F). However, if the extremely large hole FS exists in truth, the system should be heavily hole-doped one. It is quite unlikely, then the other explanation is needed.

One possible explanation of the large hole FS is the surface effect. If a single-crystalline RFePnO is cleaved, RO or FePn layer seems to appear on the surface. Both of RO and FePn layers do not obtain electronic neutrality, therefore a new electronic state seems to emerge on the surface. Even if the observed FS mapping at $k_z = 0$ is hole doped state on the surface, the shapes of all hole and electron FSs hardly change. As a result, differences from the original states seem to be nearly the same for all samples. Therefore, the discussion of substitution effect in NdFeP$_{1-x}$As$_x$(O, F) is meaningful.

On the other hand, the hole FS constructed of the band with d_{xy} orbital character is predicted by band calculation for NdFeAs(O, F). It is considered as the trigger of high T_c nodeless superconductivity in spin fluctuation theory. However, it is not observed in all x. Recently, it is suggested that the d_{xy} band shows the strong dependence of photon energy of the incident light in K$_{0.8}$Fe$_{1.6}$Se$_2$ in the ARPES measurements. In the present system, the d_{xy} band in the bulk electronic state may also be strongly dependent on the energy of the incident light, and the selected photon energy may be too inadequate to observe the d_{xy} band or FS.

8.2.2 x dependence of FSs

Following two characteristic features of x dependence are observed in the results of ARPES measurements.

(i) The largest hole FS gradually shrinks with increasing x.

(ii) The smallest hole FS disappears at $x \sim 0.8$.

As for (i), the size of the largest hole FS is 1.06 Å^{-1} at $x = 0.4$, 0.90 Å^{-1} at $x = 0.8$ and 0.82 Å^{-1} at $x = 1.0$, which corresponds to about 47 %, 40 % and 37 % for first Brillouin zone, respectively. According to the band calculation, d_{z^2} band makes a hole FS at Z in RFePO and the band sinks below E_F with increasing As content x. Therefore, the shrinkage of the hole FS with x is consistent with the band calculation (though the hole FS exists in all x). This is the first experimental report of the systematic x dependence of the d_{z^2} band.

As for (ii), EDCs for P polarization of $x = 0.4$ and 0.8 are shown in Figure 8.5. The smallest hole FS constructed of d_{xz} band disappears at $x \sim 0.8$. To compare the feature (ii) in my
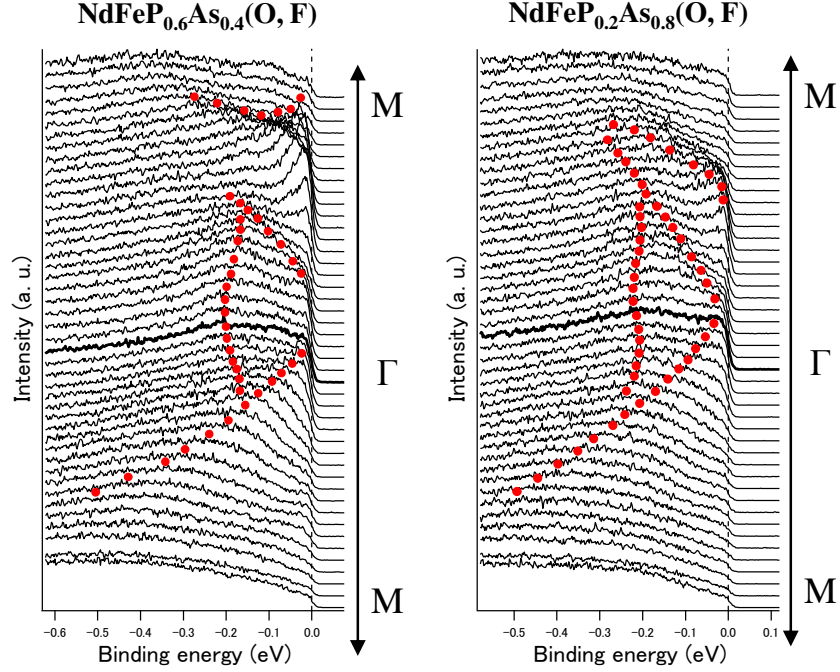
Figure 8.5: EDCs for P polarization of $x = 0.4$ and 0.8.

experimental result with the previous studies, the band dispersions and FS mappings at $k_z = 0$ of LaFePO, LaFeAsO and NdFeAsO$_{0.85}$F$_{0.15}$ [43, 44, 46, 70] are shown in Figure 8.6. In the case of LaFePO, a large hole FS (Γ_2 in the left panel of Figure 8.6) and double degenerated hole FSs (Γ_1) are observed. In LaFeAsO, a large hole FS (Γ_2) and a small non-degenerated hole FS are observed. In PrFeAsO$_{0.7}$ (shown in chapter 1), a large hole FS and a small FS are also reported, though the assignment of the orbital character is different from mine [46]. In NdFeAsO, only a large hole FS is observed and a hole-like-band exists below E_F around Γ point.

If the above previous studies are explained from the suggestion (ii) in NdFeP$_{1-x}$As$_x$(O, F), the degenerated hole FSs (Γ_1) in LaFePO seems to be resolved and they are separated to the small hole FS and a pseud-hole FS in LaFeAsO. In widely, the small hole band seems to gradually sinks below E_F with decreasing bond angle α (or the increasing h_{Pn}) in LaFePO, LaFeAsO and NdFeAsO$_{0.85}$F$_{0.15}$ (and perhaps PrFeAsO$_{0.7}$).

The band calculation where the bond angle α is virtually changed has been performed [71]. The band calculation result for the bond angle α variations of 120 °, 110 ° and 100 ° in LaFeAsO is shown in Figure 8.7. The two hole bands around Γ are nearly degenerated at $\alpha = 120$ °, which is similar to the experimental result of LaFePO. The degeneracy is resolved following decreasing α and it is similar situation to $x = 0.4$. The degeneracy is completely resolved at $\alpha = 110$
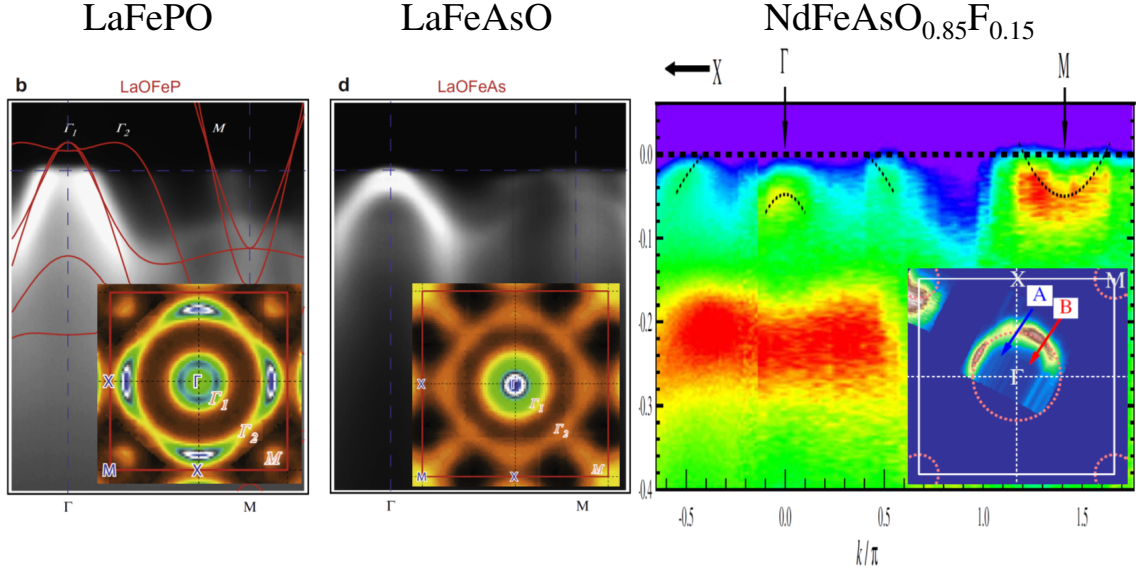
Figure 8.6: Band dispersions and FS mappings at $k_z = 0$ of LaFePO (Left), LaFeAsO (Center) and NdFeAsO$_{0.85}$F$_{0.15}$ (Right) [43, 44, 46, 70].

$^\circ$. One hole FS gradually decreases with decreasing α and completely disappears $\alpha = 100$ $^\circ$. As a result, the tendency to disappear the hole FS constructed of d_{xz} band is similar to band calculation, however, the difference of α is ~ 10 $^\circ$.

In the present system, the d_{xz} band sinks down with increasing x, and the top of this band touches E_{F} around Γ point at $x \sim 0.8$. Below $x \sim 0.8$, the hole FS with d_{xz} is observed around Γ point, while it disappears above $x \sim 0.8$. The x dependence of T_{c} and n, their relationship and other transport properties are distinctly changed around $x = 0.6 \sim 0.8$. As described before, I think that these nonmonotonic changes of T_{c} and transport properties are caused by the transformation of FS from the FeP type to the FeAs one, i.e., the 3-dimensional hole FS with d_{z^2} orbital character disappears and the cylindrical d_{xy} FS appears. Unfortunately, I could not observe the above-mentioned FS changes perhaps because of the surface effect and other problems. However, I found the clear change of d_{xz} band around $x \sim 0.8$, and think that the change of this FS induces the nonmonotonic changes of T_{c} and transport properties.
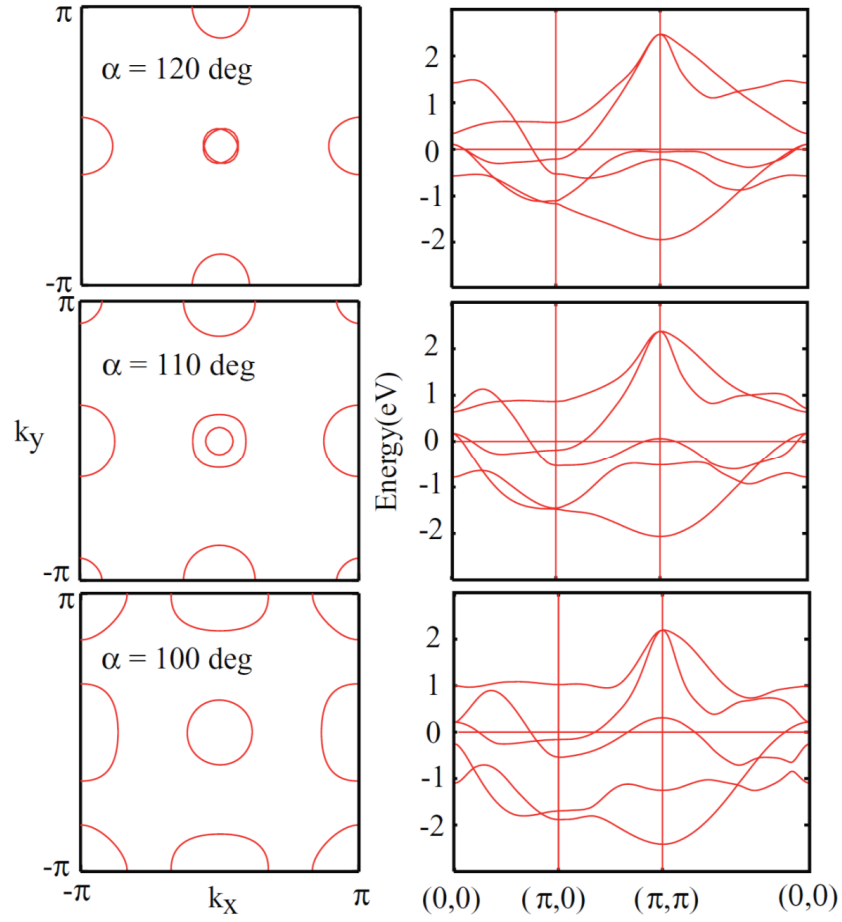
Figure 8.7: The band calculation result for bond angle α variations of 120 °, 110 ° and 100 ° in LaFeAsO [71].

Part IV

Conclusion

Chapter 9

Conclusion

In this work, I have investigated the transport properties and ARPES in $R\mathrm{FeP}_{1-x}\mathrm{As}_x\mathrm{O}_{1-y}\mathrm{F}_y$ in order to find a key parameter determining T_c in iron pnictides. From my work, the following experimental results and conclusions are obtained.

(i) I have studied the transport properties of the polycrystalline samples of $R\mathrm{FeP}_{1-x}\mathrm{As}_x\mathrm{O}_{0.9}\mathrm{F}_{0.1}$ ($R = $ La, Pr and Nd), and clarified the relation between T_c and the transport properties by changing the P/As ratio in this system. The present results have revealed that there are two distinct regions of x. In the low x region ($x < 0.6$ - 0.8), T_c linearly increases from ~ 3 to ~ 30 K with decreasing the power n in $\rho = \rho_0 + AT^n$ from ~ 2 at $x = 0$ to ~ 1 around $x = 0.6$ - 0.8. This strongly suggests that some bosonic fluctuation such as AFM one is a primary factor to enhance T_c. The universal T_c - n relation holds for all the R systems with $x < 0.6$ - 0.8 in the present study as well as $Ae\mathrm{Fe}_2(\mathrm{As}, \mathrm{P})_2$ ($Ae = $ Ba and Sr). In addition to the T-linear resistivity, R_H, ρ_0, and A are strongly enhanced near $x = 0.6$ - 0.8, suggesting some critical change of the electronic state. In the high x region ($x > 0.6$ - 0.8), on the other hand, T_c becomes strongly R-dependent and further increases with x, but shows no clear correlation with n. The compounds with $x > 0.6$ - 0.8 seem to approach another universal T_c - n relation which holds for $R\mathrm{FeAsO}_{1-y}$ and $(\mathrm{Ba}, \mathrm{K})\mathrm{Fe}_2\mathrm{As}_2$. The presence of two distinct T_c - n relations could be the evidence that there are two T_c-rising mechanisms and related two different FS states in the iron pnictides.

(ii) I have synthesized the single crystals of $\mathrm{NdFeP}_{1-x}\mathrm{As}_x\mathrm{O}_{0.9}\mathrm{F}_{0.1}$ and investigated the transport properties and ARPES of them. I have succeeded in the single crystal grown of this system by high pressure technique. The transport properties of these single crystals without the grain

boundary effect are consistent with those of polycrystalline samples. The present results of single crystals strongly indicate the existence of two T_c-rising mechanism and two different FS states.

(ⅲ) I have performed the ARPES measurement using single crystals of $NdFeP_{1-x}As_xO_{0.9}F_{0.1}$ with $x = 0.4$, 0.8 and 1.0 in order to clarify x-dependent changes of band structures and FSs. The ARPES results indicate the existence of three hole and two electron FSs in $x = 0.4$, and two hole and two electron FSs in $x = 0.8$ and 1.0 samples. The orbital characters of these FSs have been assigned by the measurements of polarization dependence of incident light. The d_{xz} hole FS exists around Γ point at $x = 0.4$. The d_{xz} band sinks down with increasing x, and the top of this band touches E_F around Γ point in the $x = 0.8$ sample. With further increasing x, the hole FS with d_{xz} character disappears at $x = 1.0$. The T_c, n and other transport properties distinctly change around $x = 0.6$ - 0.8. The clear difference of FSs below and above $x = 0.6$ - 0.8 may be related with the change of transport properties, and support the scenario of two T_c-rising mechanisms and two different FS states in this system.

Future works

In this work, I succeeded in the observation of several FSs and the systematic doping dependence of band structure by ARPES study. As described in the main content, I think that the nonmonotonic changes of T_c and transport properties are caused by the transformation of FS from FeP type to FeAs one, i.e., the 3-dimensional hole FS with d_{z^2} orbital character disappears and the cylindrical d_{xy} FS appears. Unfortunately, I could not observe such FS changes perhaps because of the surface effect and other problems. Particularly, the d_{xy} FS perhaps plays an important role for the appearance of high T_c superconductivity but it is missing in my spectra. This d_{xy} FS must be searched and its behavior must be clarified by ARPES measurements using the incident lights with various photon energy. In addition, I could not observe the superconducting gap of each FS by ARPES because of the time limitation. They also must be observed in future works to clarify the superconducting feature in this system.

Bibliography

[1] Y. Kamihara, H. Hiramatsu, M, Hirano, R, Kawamura, H, Yanagi, T, Kamiya, and H. Hosono, J. Am. Chem. Soc. **128**, 10012 (2006).

[2] Y. Kamihara, T. Watanabe, M. Hirano, and H. Hosono, J. Am. Chem. Soc. **130**, 3296 (2008).

[3] Z. Ren, W. Lu, J. Yang, W. Yi, X. Shen, Z. Li, G. Che, X. Dong, L. Sun, F. Zhou, and Z. Zhao, Chin. Phys. Lett. **25**, 2215 (2008).

[4] C. Wang, L. Li, S. Chi, Z. Zhu, Z. Ren, Y. Li, Y. Wang, X. Lin, Y. Luo, S. Jiang, X. Xu, G. Cao, and Z. Xu, Euro. Phys. Lett. **83**, 67006 (2008).

[5] H. Luetkens, H.-H. Klauss, M. Kraken, F. J. Litterst, T. Dellmann, R. Klingeler, C. Hess, R. Khasanov, A. Amato, C. Baines, M. Kosmala, O. J. Schumann, M. Braden, J. Hamann-Borrero, N. Leps, A. Kondrat, G. Behr, J.Werner, and B. Buchner, Nature Mater. **8**, 305 (2009).

[6] J. Zhao, Q. Huang, C. de la Cruz, S. Li, J. W. Lynn, Y. Chen, M. A. Green, G. F. Chen, G. Li, Z. Li, J. L. Luo, N. L. Wang, and P. Dai, Nature Mater. **7**, 953 (2008).

[7] N. Fujiwara, S. Tsutsumi, S. Iimura, S. Matsuishi, H. Hosono, Y. Yamakawa and H. Kontani, Phys. Rev. Lett. **111**, 097002 (2013).

[8] K. Miyazawa, K. Kihou, P. M. Shirage, C. H. Lee, H. Kito, H. Eisaki, and A. Iyo, J. Phys. Soc. Jpn. **78**, 034712 (2009).

[9] S. Matsuishi, Y. Inoue, T. Nomura, Y. Kamihara, M. Hirano, and H. Hosono, New J. Phys. **11**, 025012 (2008).

[10] E. M. Brüning, C. Krellner, M. Baenitz, A. Jesche, F. Steglich, and C. Geibel, Phys. Rev. B **101**, 117206 (2008).

[11] J.-Q. Yan, A. Kreyssig, S. Nandi, N. Ni, S. L. Bud'ko, A. Kracher, R. J. McQueeney, R. W. McCallum, T. A. Lograsso, A. I. Goldman, and P. C. Canfield, Phys. Rev. B **78**, 024516 (2008).

[12] X. F. Wang, T. Wu, G. Wu, H. Chen, Y. L. Xie, J. J. Ying, Y. J. Yan, R. H. Liu, and X. H. Chen, Phys. Rev. Lett. **102**, 117005 (2009).

[13] H. Chen, Y. Ren, Y. Qiu, Wei Bao, R. H. Liu, G. Wu, T. Wu, Y. L. Xie, X. F. Wang, Q. Huang, and X. H. Chen, Euro. Phys. Lett. **85**, 17006 (2009).

[14] S. R. Saha, N. P. Butch, T. Drye, J. Magill, S. Ziemak, K. Kirshenbaum, P. Y. Zavalij, J. W. Lynn, and J. Paglione, Phys. Rev. B **85**, 024525 (2012).

[15] C. Lester, J. Chu, J. G. Analytis, S. C. Capelli, A. S. Erickson, C. L. Condron, M. F. Toney, I. R. Fisher, and S. M. Hayden, Phys. Rev. B **79**, 144523 (2009).

[16] S. Kasahara, T. Shibauchi, K. Hashimoto, K. Ikada, S. Tonegawa, R. Okazaki, H. Shishido, H. Ikeda, H. Takeya, K. Hirata, T. Terashima, and Y. Matsuda, Phys. Rev. B **81**, 184519 (2010).

[17] S. A. J. Kimber, A. Kreyssig, Y. Zhang, H. O. Jeschke, R. Valenti, F. Yokaichiya, E. Colombier, J. Yan, T. C. Hansen, T. Chatterji, R. J. McQueeney, P. C. Canfield, A. I. Goldman, and D. N. Argyriou, Nature Mater. **8**, 471 (2009).

[18] J. H. Tapp, Z. Tang, B. Lv, K. Sasmal, B. Lorenz, P. C. W. Chu, and A. M. Guloy, Phys. Rev. B **78**, 060505(R) (2008).

[19] O. Heyer, T. Lorenz, V. B. Zabolotnyy, D. V. Evtushinsky, S. V. Borisenko, I. Morozov, L. Harnagea, S. Wurmehl, C. Hess, and B. Büchner, Phys. Rev. B **84**, 064512 (2011).

[20] K. Mydeen, E. Lengyel, Z. Deng, X. C. Wang, C. Q. Jin, and M. Nicklas, Phys. Rev. B **82**, 014514 (2010).

[21] S. Kasahara, K. Hashimoto, H. Ikeda, T. Terashima, Y. Matsuda, and T. Shibauchi, Phys. Rev. B **85**, 060503 (2012).

[22] X. Zhu, F. Han, G. Mu, P. Cheng, B. Shen, B. Zeng, and H. Wen, Phys. Rev. B **79**, 220512(R) (2009).

[23] H. Ogino, Y. Matsumura, Y. Katsura, K. Ushiyama, S. Horii, K. Kishio, and J. Shimoyama, Supercond. Sci. Technol. **22**, 075008 (2009).

[24] P. M. Shirage, K. Kihou, C. H. Lee, H. Kito, H. Eisaki, and A. Iyo, Physica C **484**, 12 (2012).

[25] H. Kinouchi, H. Mukuda, Y. Kitaoka, P. M. Shirage, H. Fujihisa, Y. Gotoh, H. Eisaki, and A. Iyo, Phys. Rev. B **87**, 121101(R) (2013).

[26] V. Vildosola, Leonid Pourovskii, Ryotaro Arita, Silke Biermann, and Antoine Georges, Phys. Rev. B **78**, 064518 (2008).

[27] K. Kuroki, H. Usui, S. Onari, R. Arita, and Hideo Aoki, Phys. Rev. B **79**, 224511 (2009).

[28] C. H. Lee, A. Iyo, H. Eisaki, H. Kito, M. T. Fernandez-Diaz, T. Ito, K. Kihou, H. Matsuhata, M. Braden, and K. Yamada, J. Phys. Sci. Jpn. **77**, 083704 (2008).

[29] Y. Mizuguchi, Y. Hara, K. Deguchi, S. Tsuda, T. Yamaguchi, K. Takeda, H. Kotegawa, H. Tou, and Y. Takano, Supercond. Sci. Technol. **23** 054013 (2010).

[30] J. D. Fletcher, A. Serafin, L. Malone, J. G. Analytis, J.-H. Chu, A. S. Erickson, I. R. Fisher, and A. Carrington, **102**, 147001 (2009).

[31] L. Malone, J. D. Fletcher, A. Serafin, and A. Carrington, Phys. Rev. B **79**, 145501(R) (2009).

[32] K. Hashimoto, M. Yamashita, S. Kasahara, Y. Senshu, N. Nakata, S. Tonegawa, K. Ikada, A. Serafin, A. Carrington, T. Terashima, H. Ikeda, T. Shibauchi, and Y. Matsuda, Phys. Rev. B **81**, 220501(R) (2010).

[33] K. Hashimoto, S. Kasahara, R. Katsumata, Y. Mizukami, M. Yamashita, H. Ikeda, T. Terashima, A. Carrington, Y. Matsuda, and T. Shibauchi, arXiv: 1107.4505v1 (2011).

[34] T. Kondo, A. F. Santander-Syro, O. Copie, C. Liu, M. E. Tillman, E. D. Mun, J. Schmalian, S. L. Bud'ko, M. A. Tanatar, P. C. Canfield, and A. Kaminski, Phys. Rev. Lett. **101**, 147003 (2008).

[35] H. Ding, P. Richard, K. Nakayama, K. Sugawara, T. Arakane, Y. Sekiba, A. Takayama, S. Souma, T. Sato, T. Takahashi, Z. Wang, X. Dai, Z. Fang, G. F. Chen, J. L. Luo, and N. L. Wang, Euro. Phys. Lett. **83**, 47001 (2008).

[36] Y. Zhang, Z. R. Ye, Q. Q. Ge, F. Chen, Juan Jiang, M. Xu, B. P. Xie, and D. L. Feng, Nature Phys. **4**, 2248 (2012).

[37] M. Yamashita, Y. Senshu, T. Shibauchi, S. Kasahara, K. Hashimoto, D. Watanabe, H. Ikeda, T. Terashima, I. Vekhter, A. B. Vorontsov, and Y. Matsuda, Phys. Rev. B **84**, 060507(R) (2011).

[38] K. A. Yates, T. M. Usman, K. Morrison, J. D. Moore, A. M. Gilbertson, A. D. Caplin, L. F. Cohen, H. Ogino and J. Shimoyama, Supercond. Sci. Technol. **23**, 022001 (2010).

[39] K. T. Lai, A. Takemori, S. Miyasaka,1, F. Engetsu, H. Mukuda, and S. Tajima, Phys. Rev. B **90**, 064504 (2014).

[40] Y. Luo, Y. Li, S. Jiang, J. Dai, G. Cao, and Z. Xu, Phys. Rev. B **81**, 134422 (2010).

[41] Y. Luo, H. Han, S. Jiang, X. Lin, Y. Li, J. Dai, G. Cao, and Z. Xu, Phys. Rev. B **83**, 054501 (2011).

[42] Y. Li, X. Lin, T. Zhou, J. Shen, Y. Luo, Q. Tao, G. Cao, Z. Xu, Physica C **470**, 493 (2009).

[43] D. H. Lu, M. Yi, S. -K. Mo, A. S. Erickson, J. Analytis, J.-H. Chu, D. J. Singh, Z. Hussain, T. H. Geballe, I. R. Fisher, and Z.-X. Shen, Nature **455**, 07263 (2008).

[44] D. H. Lu, M. Yi, S. -K. Mo, J. G. Analytis, J. -H. Chu, A. S. Erickson, D. J. Singh, Z. Hussain, T. H. Geballe, I. R. Fisher, and Z. -X. Shen, Physica C **469**, 452 (2009).

[45] A. I. Coldea, J. D. Fletcher, A. Carrington, J. G. Analytis, A. F. Bangura, J.-H. Chu, A. S. Erickson, I. R. Fisher, N. E. Hussey, and R. D. McDonald, Phys. Rev. Lett. **101**, 216402 (2008).

[46] I. Nishi, M. Ishikado, S. Ideta, W. Malaeb, T. Yoshida, A. Fujimori, Y. Kotani, M. Kubota, K. Ono, M. Yi, D. H. Lu, R. Moore, Z. -X. Shen, A. Iyo, K. Kihou, H. Kito, H. Eisaki, S. Shamoto, and R. Arita, Phys. Rev. B **84**, 014504 (2011).

[47] L. X. Yang, B. P. Xie, Bo Zhou, Yan Zhang, Q. Q. Ge, Fan Wu, X. F. Wang, X. H. Chen, and D. L. Feng, J. Phys. Chem. Solids **72**, 460 (2011).

[48] F. Izumi, and K. Momma, Solid. State. Phenom. **130**, 15 (2007).

Bibliography

[49] T.M. McQueen, M. Regulacio, A. J. Williams, Q. Huang, J. W. Lynn, Y.S. Hor, D. V. West, M.A. Green, and R. J. Cava, Phys. Rev. B **78**, 024521 (2008).

[50] A. S. Sefat, A. Huq, M. A. McGuire, R. Jin, B. C. Sales, D. Mandrus, L. M. D. Cranswick, P. W. Stephens, and K. H. Stone, Phys. Rev. B **78**, 104505 (2008).

[51] B.I. Zimmer, W. Jeitschko, J. H. Albering, R. Glaum, and M. Reehuis, J. Alloys Compds. **229**, 238 (1995).

[52] P. Quebe, L. Terbuchte, and W. Jeitschko, J. Alloys Compd. **302**, 70 (2000).

[53] Y. Xiao, Y. Su, R. Mittal, T. Chatterji, T. Hansen, S. Price, C. M. N. Kumar, J. Persson, S. Matsuishi, Y. Inoue, H. Hosono, and Th. Brueckel, Phys. Rev. B **81**, 094523 (2010).

[54] R. E. Baumbach, J. J. Hamlin, L. Shu, D. A. Zocco, N. M. Crisosto, and M. B. Maple, New J. of Phys. **11**, 025018 (2009).

[55] Z. Ren, J. Yang, W. Lu, W. Yi, X. Shen, Z. Li, G. Che, X. Dong, L. Sun, F. Zhou, and Z. Zhao, Euro. Phys. Lett. **82**, 57002 (2008).

[56] M. Ishikado, S. Shamoto, H. Kito, A. Iyo, H. Eisaki, T. Ito, and Y. Tomioka, Physica C **469**, 901 (2008).

[57] N. W. Ashcroft and N. D. Mermin, Solid State Physics, 240 (1976).

[58] T. Moriya, Spectroscopy of Mott Insulators and Correlated Metals, eds. A. Fujimori and Y. Tokura, p.66-79 (Springer, Berlin, 1995).

[59] H. Mukuda, F. Engetsu, K. Yamamoto, K. T. Lai, M. Yashima, Y. Kitaoka, A. Takemori, S. Miyasaka, and S. Tajima, Phys. Rev. B **89**, 064511 (2014).

[60] Y. Nakajima, H. Shishido, H. Nakai, T. Shibauchi, K. Behnia, K. Izawa, M. Hedo, Y. Uwatoko, T. Matsumoto, R. Settai, Y. Onuki, H. Kontani, and Y. Matsuda, J, Phys. Soc, Jpn. **76**, 024703 (2007).

[61] S. Ishida, M. Nakajima, Y. Tomioka, T. Ito, K. Miyazawa, H. Kito, C. H. Lee, M. Ishikado, S. Shamoto, A. Iyo, H. Eisaki, K. M. Kojima, and S. Uchida, Phys. Rev. B **81**, 094515 (2010).

[62] N. D. Zhigadlo, S. Weyeneth, S. Katrych, P. J. W. Moll, K. Rogacki, S. Bosma, R. Puzniak, J. Karpinski, and B. Batlogg, Phys. Rev. B **86**, 214509 (2012).

[63] A. Damascelli, Z. Hussain, and Z. X. Shen, Rev. Mod. Phys. **75**, 473 (2003).

[64] Z. R. Ye, Y. Zhang, B. P. Xie, and D. L. Feng, Chin. Phys. B **22**, 087407 (2013).

[65] P. Cheng, H. Yang, Y. Jia, L. Fang, X. Zhu, G. Mu, and H. Wen, Phys. Rev. B **78**, 134508 (2008).

[66] H. Q. Yuan, F. M. Grosche, M. Deppe, C. Geibel, G. Sparn, and F. Steglich, Science **302**, 2104 (2003).

[67] H. Q. Yuan, F. M. Grosche, M. Deppe, G. Sparn, C. Geibel, and F. Steglich, Phys. Rev. Lett. **96**, 047008 (2006).

[68] G. Seyfarth, A. -S. Ruetschi, K. Sengupta, A. Georges, and D. Jaccard, Phys. Rev. B **85**, 205105 (2012).

[69] S. Watanabe, M. Imada, and K. Miyake, J. Phys. Soc. Jpn. **75**, 043710 (2006).

[70] C. Liu, T. Kondo, A. D. Palczewski, G. D. Samolyuk, Y. Lee, M. E. Tillman, N. Ni, E. D. Muna, R. Gordon, A. F. Santander-Syro, S. L. Bud'ko a, J. L. McChesney, E. Rotenberg, A. V. Fedorov, T. Valla, O. Copie, M. A. Tanatar, C. Martin, B. N. Harmon, P. C. Canfield, R. Prozorov, J. Schmalian, and A. Kaminski, Physica C **469**, 461 (2009).

[71] H. Usui and K. Kuroki, Phys. Rev. B, **84**, 024505 (2011).

Acknowledgment

I would like to appreciate following people who supported me to accomplish this study. Without their help, this dissertation would not have materialized.

Tajima Laboratory

Prof. Setsuko Tajima, Prof. Shigeki Miyasaka, Prof. Masamichi Nakajima, Prof. Takahiko Masui, Mr. Shinnosuke Suzuki, Mr. Satoshi Saijo, Mr. Wataru Hirata, Mr. Ryuichiro Fukuta, Mr. Tyler Miyake, Dr. Kwing To Lai, Mr. Tatsuya Kobayashi, Mr. Kazuhiro Henmi, Mr. Tohru Adachi, Mr. Taichi Tokuhisa, Mr. Masahiro Uekubo, Mr. Takahiro Yamamoto and Ms. Yoshiko Ishimoto

Graduate school of science, Osaka University

Prof. Kazuhiko Kuroki, Prof. Hidetomo Usui, Prof. Katsuhiro Suzuki, Prof. Masayuki Hagiwara and Prof. Takanori Kida

Graduate school of engineering science, Osaka University

Prof. Yoshio Kitaoka, Prof. Hidekazu Mukuda, Prof. Masaaki Ashida, Prof. Masayoshi Ichimiya, Prof. Akira Sekiyama, Prof. Takayuki Kisu, Prof. Hidenori Hujiwara and Mr. Kohei Yamagami

UVSOR Facility, Institute for Molecular Science (IMS) and Nagoya University

Prof. Tetsuya Hajiri, Prof. Kiyohisa Tanaka and Prof. Masaharu Matsunami

International Superconductivity Technology Center (ISTEC) - Superconductivity Research Laboratory (SRL)

List of publications

1. A. Takemori, S. Saijo, S. Suzuki, S. Miyasaka, S. Tajima, A. Nakao, H. Nakao, R. Kumai, and Y. Murakami, "Correlation between T_c and Transport Properties in $PrFeP_{1-x}As_xO_{0.9}F_{0.1}$", J. Phys. Soc. Jpn. **81**, SB043 (2012).

2. A. Takemori, S. Miyasaka, S. Tajima, S. Lee, S. Adachi, N. Chikumoto, and K. Tanabe, "Single crystal growth of Nd-1111 iron pnictide superconductors by high pressure synthesis", JPS Conf. Proc. **1**, 012111 (2014).

3. S. Miyasaka, A. Takemori, S. Saijo, S. Suzuki, and S. Tajima, "Search for Key Parameter for Determining T_c in Fe-based Superconductors: Study of As/P Substitution in RFe(As, P)(O, F) [R = La and Nd]", J. Phys. Chem. Solid **72**, 414 (2011).

4. T. Okuda, W. Hirata, A. Takemori, S. Suzuki, S. Saijo, S. Miyasaka, and S. Tajima, "Thermoelectric Properties of $LaFePO_{1-x}F_x$ and $LaFeAsO_{1-x}F_x$ −Possibility of the Hidden Mass Enhancement of $LaFeAsO_{1-x}F_x$−", J. Phys. Soc. Jpn. **80**, 044704 (2011).

5. S. Adachi, T. Shimode, M. Miura, N. Chikumoto, A. Takemori, K. Nakao, Y. Oshikubo, and K. Tanabe, "Pulsed laser deposition of $BaFe_2(As, P)_2$ superconducting thin films with high critical current density", Supercond. Sci. Technol. **25**, 105015 (2012).

6. M. Miura, S. Adachi, T. Shimode, K. Wada, A. Takemori, N. Chikumoto, K. Nakao, and K. Tanabe, "Anisotropy and Superconducting Properties of $BaFe_2(As_{1-x}P_x)_2$ Films with Various Phosphorus Contents", Appl. Phys. Express. **6**, 093101 (2013).

7. S. Miyasaka, A. Takemori, T. Kobayashi, S. Suzuki, S. Saijo and S. Tajima, "Two Fermi Surface States and Two T_c-Rising Mechanisms Revealed by Transport Properties in RFeP$_{1-x}$As$_x$O$_{0.9}$F$_{0.1}$ (R = La, Pr, and Nd)", J. Phys. Soc. Jpn. **82**, 124706 (2013).

8. H. Mukuda, F. Engetsu, K. Yamamoto, K. T. Lai, M. Yashima, Y. Kitaoka, A. Takemori, S. Miyasaka and S. Tajima, "Enhancement of superconducting transition temperature due to antiferromagnetic spin fluctuations in iron-pnictides $LaFe(As_{1-x}P_x)(O_{1-y}F_y)$: ^{31}P-NMR Studies", Phys, Rev. B **89**, 064511 (2014).

9. K. T. Lai, A. Takemori, S. Miyasaka, F. Engetsu, H. Mukuda, and S. Tajima, "Evolution of the phase diagram of $LaFeP_{1-x}As_xO_{1-y}F_y$ ($y = 0$ - 0.1)", Phys, Rev. B **90**, 064504 (2014).

List of presentation at international conferences

1. "Search for Key Parameter for Determining T_c in Fe-based Superconductors: Study of As/P Substitution in RFe(As, P)(O, F) [R = La and Nd]", The 9th International Conference on Spectroscopies of Novel superconductors 2010, in Shanghai in 2010 (Poster).

2. "P/As Substitution Effect on 1111 Iron Pnictide Superconductors", International Workshop on Novel Superconductors and Super Materials 2011, in Tokyo in 2011 (Poster).

3. "Correlation between T_c and Transport Properties in RFeP$_{1-x}$As$_x$O$_{1-y}$F$_y$", TOKIMEKI 2011 -International workshop on heavy fermions-, in Osaka in 2011 (Poster).

4. "Two Different Superconducting Mechanisms in RFe(P, As)(O, F) [R = rare earth]", Materials and Mechanisms of Superconductivity 2012, in Washington, D.C. in 2012 (Poster).

5. "Single crystal growth of NdFeAs(O, F) by high pressure synthesis", IRON-SEA, in Osaka in 2013, (Poster).

6. "Single crystal growth of Nd-1111 iron pnictide superconductors by high pressure synthesis", Asia Pacific Physics Conference 12, in Chiba in 2013 (Poster).

7. "Band Structure Change with P/As Substitution in NdFe(P, As)(O, F)", The 1st International Symposium on Cadet Program, in Osaka in 2014 (Poster).

List of presentation at the Japan physical society meetings

1. "P/As substitution effect in 1111-type iron pnictide superconductors", The Japan physical society fall meeting, in Osaka in 2010 (Oral).

2. "P/As substitution effect in 1111-type iron pnictide superconductors II", The Japan physical society spring meeting, in Niigata in 2011 (Oral).

3. "Transport properties in $R\mathrm{FeP}_{1-x}\mathrm{As}_x\mathrm{O}_{0.9}\mathrm{F}_{0.1}$ (R = La, Pr, Nd)", The Japan physical society fall meeting, in Toyama in 2011 (Oral).

4. "Single crystal groth and physical properties measurement of 1111 iron pnictide superconductor NdFe(P,As)(O,F)", The Japan physical society fall meeting, in Aichi in 2014 (Oral).

5. "Composition-dependent ARPES on $\mathrm{NdFeP}_{1-x}\mathrm{As}_x$(O, F), The Japan physical society spring meeting, in Tokyo in 2015 (Oral).